Abbs, Charlotte (2014) Quantum dynamics of non-linear optomechanical systems. PhD thesis, University of Nottingham.

Access from the University of Nottingham repository:
http://eprints.nottingham.ac.uk/27692/1/C%20Abbs%20PhD%20Thesis.pdf

QUANTUM DYNAMICS OF NON-LINEAR OPTOMECHANICAL SYSTEMS

by

CHARLOTTE ABBS, MPHYS

Thesis submitted to The University of Nottingham
for the degree of Doctor of Philosophy

March 2014

ABSTRACT

This thesis explores the dynamics of optomechanical systems, which use radiation pressure to couple together optical and mechanical modes. Such systems display dynamics ranging from the quantum to the classical, with a variety of applications including ground state cooling and precision measurements. In this thesis two different geometries are presented for such a system in the form of the 'reflective' and 'dispersive' systems. Different aspects of the dynamics are investigated numerically and analytically.

Firstly the reflective system is introduced, which consists of a cavity formed from a fixed and a moveable mirror. The optical frequency of the cavity couples linearly to the moveable mirror's position. This geometry is explored as the cavity is driven by a laser, revealing a range of dynamical states in the mirror as the drive frequency is varied.

An alternative geometry is presented in the form of the dispersive optomechanical system. Two fixed mirrors with a partially transmitting membrane at the centre provide a cavity supporting two optical modes, that couple approximately linearly or quadratically to the membrane position, depending on where the membrane is fixed.

The system is explored in both linear and quadratic coupling regimes. Quadratic coupling is explored for a single optical mode by selecting a high tunnelling rate through the membrane. The dynamics of the membrane are explored via a similar set of techniques to those applied to the reflective system.

Linear coupling for two optical modes is explored in the regimes of blue and red detuning. First resolved sideband cooling is explored, providing an alternative approach ground state cooling (which has been explored for the reflective case). Finally, strongly driving the system over a range of coupling strengths induces classical behaviour, extending from limit cycle oscillations to chaotic motion.

ACKNOWLEDGMENTS

CONTENTS

LIST OF FIGURES

LIST OF TABLES

1

INTRODUCTION

Studies of the interaction between light and matter form the basis of an understanding of how humans observe the world. The field of quantum optics applies quantum theory to these interactions by accounting for wave-particle duality[1]. That light behaves as discrete particles (photons) has been a momentous discovery of the 20th century[2, 3]. Optomechanical systems play a key role in quantum optics, by coupling optical and mechanical modes together. This coupling allows the behaviour of a nanoscale object to be observed via measurements of the light field. Furthermore, optomechanical systems offer insight into a variety of physical phenomena occurring at the boundary between quantum and classical physics.

1.1 RADIATION PRESSURE

A key feature of optomechanical systems is their use of radiation pressure, an effect documented as far back as the 17th century, when Johannes Kepler noticed that the tails of passing comets always pointed away from the sun. This led him to postulate the existence of a 'solar breeze', blowing the tails outwards from the sun[4]. This was accompanied by an appeal that "ships and sails proper for heavenly air should be fashioned" so that humans could travel the skies. Unwittingly, he had stumbled upon the concept of solar sails - a feat of engineering which has recently been achieved by the Japanese Aerospace Exploration Agency[5].

What Kepler had actually observed was the action of radiation pressure on the tails of comets. Solar photons strike the vapourized gas particles emitted from the comet, and scatter off them. The change in their momentum results in a force on the gas, in the photon's original direction of travel. The effect occurs when photons strike any surface, but is more pronounced for a reflecting body, where the change in momentum is twice the original momentum. The force F exerted on a completely reflecting surface by a light beam of power P is $F = 2P/c$, where c is the speed of light.

Long after Kepler, the existence of radiation pressure was verified in laboratory conditions by Lebedev in 1901[6]. Owing to the small momentum carried by photons, the pressure force is typically too small to deflect a macroscopic object. However, the effect can be magnified by selecting lightweight, reflecting objects with large surface areas, and using high intensity light. This is the principle behind the design of solar sails[7, 8]; these large, reflecting sheets of metal are propelled through space using only the radiation emitted from the sun.

1.2   OPTOMECHANICAL SYSTEMS

In order to observe deflection of objects by light much closer to home, optomechanical systems have been developed. A cavity formed from two mirrors, driven by a laser, provides a practical system in which to observe the effects of radiation pressure, as the force is amplified by repeated reflections. The light field circulating the cavity is coupled to a mechanical mode, provided by a resonator of some description. The simplest example is a setup where one of the cavity mirrors is mounted on a cantilever, which is free to move along the cavity's axis. Figure 1.1a shows such a system. Light striking the mirror then causes a deflection, altering the length of the cavity, and changing the frequency of the circulating radiation. This is the reflective setup, and provides a scenario where the optical frequency is coupled linearly to the position of the cantilever. An example of a mechanical mirror is given in Figure 1.2a.

The interplay of forces within the system results in a variety of dynamical effects, depending on how it is driven. As radiation circulates the cavity, a radiation pressure force is exerted on the mechanical element. The optical frequency changes as the mirror moves in response to the force, altering the intensity of radiation. However, radiation takes a finite time to leak out of the cavity. As a result the cavity responds to the mirror's motion with a time lag, and an effect known as back action arises, whereby the radiation force acts back on the resonator as it moves[9]. This effect can be used to either put energy into the resonator or extract it.

Varying the coupling strength allows one to observe a range of states in the resonator, from the classical to the quantum[10, 11, 12]. Driving the cavity below resonance extracts energy from the resonator, allowing it to be cooled to its quantum ground state[13, 14]. When the cavity is driven above resonance, one
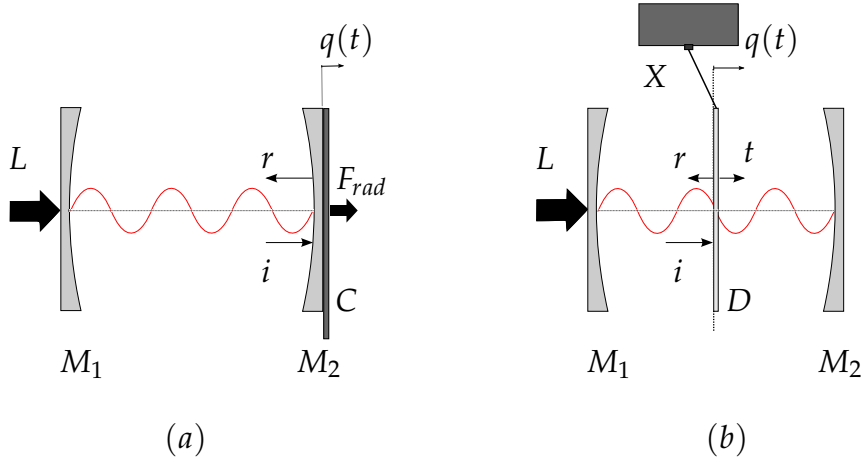
Figure 1.1: Schematic diagrams of different examples of optomechanical geometries: (a) the reflective system, consisting of a cavity formed by a fixed mirror M_1 and a movable mirror M_2, mounted on a cantilever, C, and free to move along the cavity's axis. (b) The dispersive system, where the cavity is formed from two fixed mirrors, M_1 and M_2. The mechanical mode is provided by a membrane, D, which is clamped at X, free to move along the cavity's axis. Both are driven by laser radiation, L, with mechanical displacement measured by $q(t)$.

can observe a situation where energy is absorbed by the resonator, creating phonons. The motion of the resonator can be characterised by two quantities; the damping due to back action and the phase diffusion in the resonator's state. Another useful quantity to define is the Fano factor - this measures the spread in the distribution of phonons present in the resonator, which depends on both the damping and diffusion. One of the first signifiers of quantum behaviour is when the Fano factor drops below unity, indicating number squeezing in the mechanical mode[10, 12, 15].

In recent years alternative ways of combining optical and mechanical modes have been explored. In this thesis, one such alternative geometry is explored in detail. This is often referred to as 'dispersive optomechanics'[16], an example is shown in Figure 1.1b. For this geometry, both cavity mirrors are fixed, and the mechanical element takes the form of a partially transmitting membrane mounted on a cantilever at the centre of the cavity. Figure 1.2b shows an example of a membrane made from silicon nitride. This has the advantage of offering either

linear or quadratic coupling between the mechanical and optical modes, depending on the positioning of the resonator[17].

Additional advantages are apparent when considering the engineering of such systems experimentally. The reflective setup requires the fabrication of mechanical elements with both a high quality factor and a highly reflecting surface[18]. Practically speaking this has proven difficult. By choosing a system with two fixed reflecting surfaces and a separate membrane with the high quality factor, one does not require these two properties to be combined in a single structure. For experiments in dispersive optomechanics, membranes are generally fabricated from high-stress stoichiometric silicon nitride[18]; this provides a material with low intrinsic losses[19] and minimal optical absorption[20] - providing high mechanical quality factors and optical finesses simultaneously. An example of such a membrane is give in Figure 1.2b. Here the 50 nm thick Silicon Nitride is mounted on a Silicon microchip.
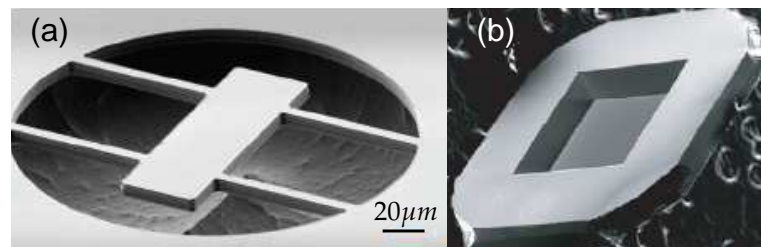
Figure 1.2: Experimental realisations of resonators for (a) the reflective system and (b) the dispersive system. The example in (a) is adapted from [21], and shows a suspended microscale mirror. In (b) a silicon nitride membrane, of dimensions $1mm \times 1mm \times 50nm$, is mounted on a silicon chip, and is adapted from [22].

1.3 APPLICATIONS OF OPTOMECHANICAL SYSTEMS

The applications of optomechanical systems are manifold. Optomechanical systems allow one to probe physical effects which lie along the boundary between quantum and classical physics. Whilst the scale of a mechanical resonator can be as large as centimetres, theoretical work suggests that strong coupling to the light field may allow quantum effects to be observed on a relatively large scale. These include superposition[11], decoherence [23], squeezing[10] and entanglement[24]. Depending on

the type of coupling, one may also be able to make quantum non-demolition (QND) measurements of the light field[7], as well as precision measurements on the resonator state. In the case of linear coupling, one can measure the position of the resonator by monitoring the light field leaking out of the cavity. In the case of quadratic coupling, the energy of the mechanical component can, in principle, be measured, thus providing a possible way of observing quantization of energy[25].

Optomechanics has been at the centre of the development of gravitational wave detectors. For a number of years, experiments aimed at the detection of gravitational waves have made use of interferometers with mechanically suspended mirrors[7, 8]. For these large scale optomechanical systems, the effects of back action were undesirable. Since the initial experiments of the 1970s and 1980s, however, the effects of back action have generated much interest, with experiments emerging to study it on a smaller scale.

There exist many variations on the optical cavity system - all with the central feature of a resonance which is tuned by mechanical motion, and experiences a delayed response. The resonance can be provided by an optical mode or an electromagnetic resonance. Examples include the optical cavity discussed, whispering gallery modes[26], single electron transistors (SETs)[15] and superconducting LC-circuits[14]. The mechanical element can be provided by anything from a cantilever [27] - in the case of a cavity mirror - to a movable capacitor plate[15] - in the case of the SET and can range in scale from nanometres [28] (in the setup discussed) to centimetres[29] (in the case of gravitational wave detectors).

1.4 THE STRUCTURE OF THIS THESIS

This thesis is organised as follows. Chapters 2 introduces the reflective optomechanical system, providing a description of a linearly coupled optomechanical system. The central features of the system are presented, and some analytic techniques introduced, which will be utilised in further chapters. A Wigner transformation is presented, which allows one to model certain aspects of the system analytically, under certain circumstances. In addition, several features are explored numerically by solving the master equation. This allows a contrast to be drawn between the classical and quantum regimes as the optomechanical coupling is swept. In addition, the limits of the Wigner

transformation are tested by calculating the switching rate for a bistable state.

Chapter 3 introduces the dispersive optomechanical system. This kind of system offers an alternative method of exploring optomechanical coupling, without the fabrication problems presented by the reflective system. Parameters in this chapter are selected to produce quadratic coupling between a single optical and mechanical mode. A similar analysis to Chapter 2 is then applied to describe the system analytically. Comparing this with a similar numerical calculation, the applicability of the Wigner transformation can be compared for the reflective and dispersive different systems. Additional numerical analysis explores quantum features of the dispersive system in the strong coupling regime.

Chapter 4 examines the dispersive optomechanical system, in the regime where two optical modes are important. Here the regime of red detuning is explored, with the aim of investigating the extent to which the system can be used to cool the resonator to its quantum ground state. Such a feat has been achieved using the reflective system[13, 14], but further advances would be needed to achieve this using the more easily fabricated dispersive system.

Chapter 5 explores the dispersive system further, in the regime of blue detuning. Here strong coupling drives the resonator into a state of self-oscillation, where dynamical multistability is possible. In this regime, fluctuations are neglected and a semi-classical approach can be taken to investigate the dynamics. The dynamics are mapped out numerically, over a range of couplings, before an analytic approximation is applied to predict the amplitudes of limit cycle oscillations.

The results of Chapter 2, Sections 2.3 and 2.4 comprise prior work on the truncated Wigner approach to optomechanical systems, by Denzil Rodrigues and Andrew Armour. These results have been published in [15, 30, 31]. The results of Chapter 2, Section 2.5 and Chapters 3 to 5 contain original research undertaken in collaboration with Andrew Armour.

EXPLORING THE REFLECTIVE OPTOMECHANICAL SYSTEM

2.1 INTRODUCTION

This chapter presents an in depth analysis of the reflective optomechanical system. This couples the optical resonance of a cavity to the mechanical motion of a suspended mirror, providing an example of linear coupling between position and frequency. The cavity mode is driven by radiation from a laser source. The circulation of radiation within the cavity results in an energy exchange between the optical and mechanical modes. The driving frequency determines the type of exchange; driving above resonance (blue detuning) causes energy to be transferred to the resonator whilst driving below resonance (red detuning) results in energy being extracted from the resonator.

Since the optical frequency couples linearly to the mechanical displacement, an accurate measurement of the resonator's position is possible via measurement of the cavity frequency. This opens up the possibility of precision measurements of such objects to within their ground state uncertainty[32]. For such measurements, the effects of 'back action' can be undesirable due to photon shot noise[33] which causes fluctuations in the mechanical position. Increasingly, research into optomechanical systems has utilised the effects of back action for the purposes of ground state cooling of resonators[34, 35, 36, 13]. This has led to the achievement of quantum ground state cooling in the reflective optomechanical system[14].

Recently, however, research has also begun to explore the regime of blue detuning[37, 38, 39]. In this regime the mechanical mode can be driven into a regime of self-oscillations where losses are balanced by radiation forces[9, 40]. Effects such as dynamical multistability[41] and chaos[42] result from strong driving. More recently, the regime of strong coupling has been explored in both theory[10, 43] and experiment[44], with the aim of generating non-classical states in the resonator, including squeezed states[45] and entangled states[24].

This chapter explores linear coupling in both the blue and red detuned regimes, by introducing the reflective optomechanical

system in Section 2.2. The optical mode is assumed to be driven at a range of frequencies and the response of the resonator investigated both analytically and numerically. In Section 2.3 the dynamics are explored analytically via a semi-classical approximation, which applies in the weak coupling regime. In Section 2.4 a numerical approach is taken, by solving the master equation. The resonator dynamics are investigated by tuning the drive frequency. The average phonon number and Fano factor are plotted, revealing transitions between stable states, observed in the Wigner function. Numerical results are then compared to plots generated using the analytic approximation of Section 2.3. Finally, a bistable regime is explored in Section 2.5 and a semi-classical calculation of the switching rate is compared to a fully quantum one.

2.2 THE SYSTEM
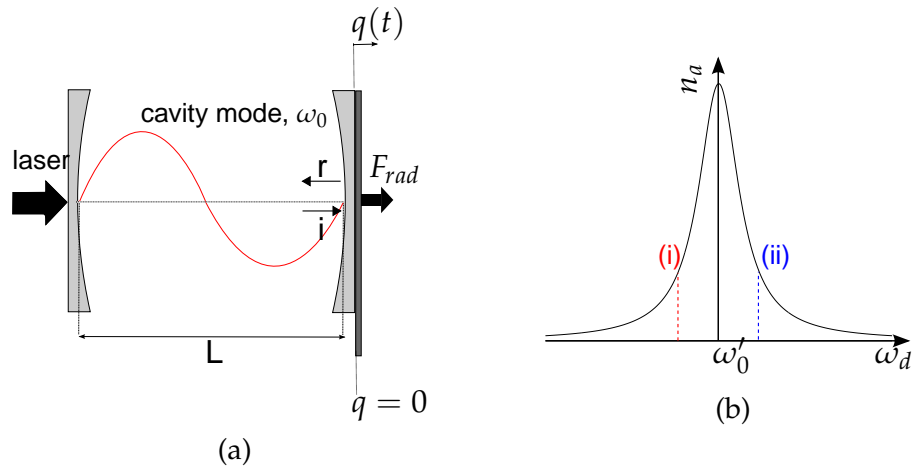
Figure 2.1: Reflective setup for an optomechanical system (a) schematic diagram showing a cavity formed from two mirrors spaced by distance L, one of which is mounted on a mechanical cantilever at position $q = 0$. As the cavity mode, ω_0, is driven by a laser, radiation circulates in the cavity and produces a pressure force F_{rad} on the cantilever as an incident wave (i) which is reflected (r). This results in a displacement $q(t)$, which alters the optical cavity frequency, from ω_0 to ω_0'. The number of photons, n_a, responds to the driving frequency, ω_d, as shown in (b). Points [i] and [ii] indicate regions where the drive frequency results in damping and driving, respectively.

Consider the system shown in Figure 2.1a. A cavity is formed from two mirrors. One mirror is mounted on a mechanical resonator (eg a cantilever), allowing it to move along the axis shown by the dotted line. The position of the resonator is given by $q(t)$. With $q = 0$ the cavity supports optical modes, of frequency ω_0, determined by the cavity length, L:

$$\omega_0 = \frac{2k\pi c}{L}, \tag{2.1}$$

where c is the speed of light and k is an integer denoting which order of resonance is being probed. A laser drives the cavity near its resonant frequency, radiation circulates within the cavity, exerting a radiation pressure on the movable mirror[46, 6]. This causes a deflection in the mirror, altering the cavity length and thus the frequency as

$$\omega_0'(t) = \frac{2k\pi c}{L + q(t)} \tag{2.2}$$

$$\approx \omega_0 - \frac{\omega_0}{L}q(t). \tag{2.3}$$

In this way the optical frequency couples linearly to the position of the mechanical mode[30, 17]. The coupling strength is denoted λ_0,

$$\lambda_0 = -\frac{\omega_0}{L}. \tag{2.4}$$

This is known as the 'reflective' setup, as the radiation is reflected by the mechanical element.

2.2.1 *Dynamical back-action*

The mechanical element is displaced via a radiation pressure force, caused by photons striking it. The total force is thus directly proportional to the number of photons in the cavity at a given time, $n_a(t)$. A classical equation of motion can be written for a resonator of mass m and natural frequency ω_m:

$$m\ddot{q} + \gamma\dot{q} + m\omega_m^2 q = F_0 n_a(t), \tag{2.5}$$

where γ is the intrinsic damping of the resonator and F_0 is the force exerted by each photon. The displacement of the mirror alters the frequency of the optical mode, whilst the drive frequency remains constant. As a result the number of photons in the cavity changes,

$$n_a(t) \approx n_0(t) + \frac{\mathrm{d}n_a}{\mathrm{d}q}q(t), \tag{2.6}$$

where $n_0(t)$ is the number of photons circulating when $q(t) = 0$. The damping constant for the cavity is given by κ, and this determines the timescale over which photons leak out. As a result there is a finite 'ring down' time[9], resulting in a delayed response to the mechanical motion, causing a time lag between the resonator being displaced and the photon intensity changing. This means that $n_a(t)$ actually depends on $q(t - \tau)$, where $\tau = \kappa^{-1}$.

$$n_a(t) \;\approx\; n_0(t) + \frac{\mathrm{d}n_a}{\mathrm{d}q}q(t - \tau) \tag{2.7}$$

$$\approx\; n_0(t) + \frac{\mathrm{d}n_a}{\mathrm{d}q}\left(q(t) - \tau\dot{q}\right) \tag{2.8}$$

Since the photon intensity affects the radiation pressure, the force on the mechanical mode also responds with a time lag, and Equation 2.5 becomes

$$m\ddot{q} + \left(\gamma + F_0\tau\frac{\mathrm{d}n_a}{\mathrm{d}q}\right)\dot{q} + m\left(\omega_m^2 - \frac{F_0}{m}\frac{\mathrm{d}n_a}{\mathrm{d}q}\right)q = F_0 n_0(t). \tag{2.9}$$

From Equation 2.9, the effect of the optomechanical coupling to n_a has three identifiable results, a static shift in the equilibrium position of q, determined by n_0, a modification to the damping and a frequency shift, both proportional to $\mathrm{d}n_a/\mathrm{d}q$. Since the position modulates the optical frequency, this can be written

$$\frac{\mathrm{d}n_a}{\mathrm{d}q} \;=\; \frac{\mathrm{d}\omega_0'}{\mathrm{d}q}\frac{\mathrm{d}n_a}{\mathrm{d}\omega_0'}. \tag{2.10}$$

Figure 2.1b illustrates the cavity response to the drive frequency, in terms of the photon number. The graph takes the form of a Lorentzian curve[9], peaked around ω_0' (which changes with q).

The quantity $\mathrm{d}\omega_0'/\mathrm{d}q$ is determined by the geometry of the system. For the system shown in Figure 2.1a, $\mathrm{d}\omega_0'/\mathrm{d}q < 0$. Figure 2.1b illustrates the cavity's response to the optical drive provided by the laser source. As ω_d approaches ω_0, the number of photons circulating in the cavity increases rapidly, so that a resonance occurs at $\omega_d = \omega_0$. Two different scenarios of detuning are labelled (i) and (ii) in Figure 2.1b:

[i]When the system is driven below resonance (red detuning), a decrease in ω_0' brings the system closer to resonance, such that $\mathrm{d}n_a/\mathrm{d}\omega_0' < 0$. As a result, $\mathrm{d}n_a/\mathrm{d}q > 0$, so that the system is more heavily damped. In addition, the effective mechanical frequency is reduced.

[ii]When the system is driven above resonance (blue detuning), an increase in ω_0' brings the system closer to resonance, such that $dn_a/d\omega_0' > 0$. As a result, $dn_a/dq < 0$, so that the total damping in the system is reduced and the mechanical frequency increased.

The resulting forces on the resonator in response to its motion are referred to as dynamical 'back action'. This effect can be used to cool or drive a resonator[36, 31]. This thesis will address both of these cases, in various optomechanical systems. The present chapter focuses largely on the case of blue detuning, with the case of red detuning briefly addressed in Section 2.3.6.

2.2.2 *The Hamiltonian*

The system of Figure 2.1a is now analysed in detail. Consider an optical mode with frequency ω_0, driven by a laser with frequency ω_d, which is coupled by radiation pressure to a mechanical mode of frequency ω_m. Provided $\omega_0 \gg \omega_m$, the Hamiltonian of the system can be written in the form[35]

$$
\begin{aligned}
H &= \omega_0 a^\dagger a + \omega_m b^\dagger b + \lambda \left(b + b^\dagger \right) a^\dagger a \\
&\quad + \Omega \left(a e^{-i\omega_d t} + a^\dagger e^{i\omega_d t} \right),
\end{aligned}
\tag{2.11}
$$

where a and b are annihilation operators for the optical and mechanical modes, respectively and Ω is the strength of the laser drive. The mechanical mode has natural frequency ω_m and is coupled with strength λ to the optical mode, which relates to λ_0 by

$$
\lambda = \frac{\lambda_0}{\sqrt{2m\omega}}.
\tag{2.12}
$$

The units are chosen so that $\hbar = 1$, this will be the case for the entire thesis. The term in λ is the coupling between the two harmonic oscillators, and is the source of the non-linear behaviour in the system.

To remove the explicit time dependence in the Hamiltonian, one can transform into a frame rotating at the drive frequency. A unitary transformation, $U = e^{iH_0 t}$ is performed on H, giving $\tilde{H} = UHU^\dagger$ with $H_0 = \omega_d a^\dagger a$. This results in a transformed Hamiltonian of the form

$$
\tilde{H} = \omega_0 a^\dagger a + \omega_m b^\dagger b + \lambda \left(b + b^\dagger \right) a^\dagger a + \Omega \left(a + a^\dagger \right).
\tag{2.13}
$$

To obtain the effective Hamiltonian, which acts on the transformed wavefunction, $|\psi'\rangle = U|\psi\rangle$, consider the Schrödinger equation acting on the wavefunction, $|\psi\rangle$:

$$i\frac{\partial|\psi\rangle}{\partial t} = H|\psi\rangle. \tag{2.14}$$

The transformed wavefunction, $|\psi'\rangle$ must obey the same equation, with $H = H_{eff}$. This leads to an effective Hamiltonian $H_{eff} = \tilde{H} - H_0$, thus

$$H_{eff} = \Delta a^\dagger a + \omega_m b^\dagger b + \lambda \left(b + b^\dagger\right) a^\dagger a + \Omega \left(a + a^\dagger\right), \tag{2.15}$$

where $\Delta = \omega_0 - \omega_d$ is the detuning of the laser drive.

2.2.3 *Master equation*

The Hamiltonian of Equation 2.15 captures the dynamics of an isolated optomechanical system, however this is not a realistic scenario. In practice any systems fabricated experience dissipation, reducing the cavity finesse, $\mathcal{F}$, and mechanical quality factor, Q. The master equation includes losses in the system which lead to damping and decoherence in the cavity and resonator modes, by modelling the effects of coupling the system to its environment.

One can model the losses in the cavity by coupling the optical mode to a spectrum of modes outside of the cavity, which describe its environment. The origin of losses in the resonator is less well understood. Prior investigations propose dissipation due to clamping losses via the cantilever supports[47] as well as defects in the resonator's structure[48]. For the following analysis, a simple model for the dissipation in the optical and mechanical modes will be used. This is often applied in the field of optomechanics[49]. Both modes are coupled to heat baths describing their environments, which consist of a series of harmonic oscillators - optical modes for the cavity and phonon modes for the resonator, which describe the bulk material the cantilever is clamped to.

With these assumptions an effective master equation can be written down[1], describing the evolution of the reduced density matrix for the system:

$$\dot{\rho} = -i\left[H, \rho\right] + \hat{\mathcal{L}}_a \rho + \hat{\mathcal{L}}_b \rho, \tag{2.16}$$

where $\hat{\mathcal{L}}_a$ and $\hat{\mathcal{L}}_b$ are operators describing the dissipation from the cavity and resonator, respectively, they are given by

$$\hat{\mathcal{L}}_a\rho = -\frac{\kappa}{2}(\overline{n}_a + 1)\left(a^\dagger a\rho + \rho a^\dagger a - 2a^\dagger \rho a\right)$$
$$-\frac{\kappa}{2}\overline{n}_a\left(aa^\dagger\rho + \rho aa^\dagger - 2a\rho a^\dagger\right), \tag{2.17}$$

$$\hat{\mathcal{L}}_b\rho = -\frac{\gamma}{2}(\overline{n} + 1)\left(b^\dagger b\rho + \rho b^\dagger b - 2b^\dagger \rho b\right)$$
$$-\frac{\gamma}{2}\overline{n}\left(bb^\dagger\rho + \rho bb^\dagger - 2b\rho b^\dagger\right), \tag{2.18}$$

where $\overline{n}_a$ and $\overline{n}$ describe the thermal occupation of the cavity and resonator, respectively and are determined by their temperature T:

$$\overline{n}_a = \left[e^{\omega_0/k_BT} - 1\right]^{-1}, \tag{2.19}$$

$$\overline{n} = \left[e^{\omega_m/k_BT} - 1\right]^{-1}, \tag{2.20}$$

where k_B is Boltzmann's constant. The dissipation terms of Equations 2.17 and 2.18 do not account for the coupling between the mechanical and optical modes, but this is a higher order effect[49], and is ignored when considering the weak coupling modelled in this system.

The transformation detailed in Equations 2.13 to 2.15 does not affect the dissipation terms. As a result Equation 2.16 can be transformed to describe the density matrix in the frame rotating at the drive frequency. This matrix is denoted $\tilde{\rho}$ and obeys a master equation of the form

$$\dot{\tilde{\rho}} = -i\left[H_{eff}, \tilde{\rho}\right] + \hat{\mathcal{L}}_a\tilde{\rho} + \hat{\mathcal{L}}_b\tilde{\rho}. \tag{2.21}$$

The cavity is assumed to have $\overline{n}_a = 0$. Because of the high optical frequency, its thermal occupation remains negligible up to $T_a \sim 300\text{K}$.

At this point two approaches can be taken. The aim is to investigate the mechanical mode, and determine the behaviour of the resonator within the coupled system. It is possible to do this both analytically and numerically. A numerical approach entails solving the master equation directly to get ρ, the density matrix (as described in Section 2.4). This encodes the properties of the resonator, which allows one to calculate its average properties, given

$$\langle\hat{O}\rangle = \text{Tr}\left[\tilde{\rho}\hat{O}\right], \tag{2.22}$$

for any observable operator, $\hat{O}$. An alternative route (described in Section 2.3) involves a semi-classical approximation, which describes the approximate behaviour of the system within a certain range of parameters.

2.3   SEMI-CLASSICAL APPROXIMATION

An analytic approach describes the dynamics of the system in the weak coupling regime, using a semi-classical approximation [30, 1]. The calculation proceeds via a Wigner transformation, whereby complex numbers α and β are introduced to describe the phase space of the cavity and resonator, respectively[1].

The Wigner function is a quasi probability distribution used in quantum mechanics[1, 50]. For a given wave function, it is a generating function for all spatial auto-correlation functions, encoding all the quantum expectation values for a given density matrix[51]. For the cavity-resonator system it is written as the Fourier transform of the characteristic function of the density operator,

$$W(\alpha, \beta) = \frac{1}{\pi^2} \int d^2\eta_a \int d^2\eta_b \, e^{\eta_a^*\alpha - \eta_a\alpha^*} e^{\eta_b^*\beta - \eta_b\beta^*} \chi(\eta_1, \eta_2), \quad (2.23)$$

where the characteristic function, $\chi(\eta_1, \eta_2)$ uniquely defines the density operator, and is given by[1]

$$\chi(\eta_1, \eta_2) = \text{Tr}\left[\rho e^{\eta_a a^\dagger - \eta_a^* a} e^{\eta_b b^\dagger - \eta_b^* b}\right]. \quad (2.24)$$

The phase space variables α and β replace the quantum operators, a and b. The two sets of variables are related by their averages, thus for example

$$\langle \alpha^*\alpha \rangle \Longleftrightarrow \frac{1}{2}\langle a^\dagger a + aa^\dagger \rangle \quad (2.25)$$

$$\langle \beta^*\beta \rangle \Longleftrightarrow \frac{1}{2}\langle b^\dagger b + bb^\dagger \rangle, \quad (2.26)$$

where averages are taken over the distribution of states in the system.

In quantum mechanics the Wigner function plays an analogous role to the classical probability distribution. However, it also accounts for the uncertainty principle and includes quantum features, thereby failing to satisfy certain criteria which apply to probability distributions[52]. For instance, it may take on negative values[10, 12].

A Wigner transformation on the master equation (Equation 2.21) gives

$$
\begin{aligned}
\frac{\partial W}{\partial t} \;=\; & \frac{\partial}{\partial \beta^*}\left(-i\omega_m\beta^* - i\lambda\left(\alpha^*\alpha - \frac{1}{2}\right) + \frac{\gamma}{2}\beta^*\right)W \\
& + \frac{\partial}{\partial \beta}\left(i\omega_m\beta + i\lambda\left(\alpha^*\alpha - \frac{1}{2}\right) + \frac{\gamma}{2}\beta\right)W \\
& + \frac{\partial}{\partial \alpha^*}\left(-i\Delta\alpha^* - i\lambda(\beta + \beta^*)\left(\alpha^*\alpha - \frac{1}{2}\right) + \frac{\kappa}{2}\alpha^*\right)W \\
& + \frac{\partial}{\partial \alpha}\left(i\Delta\alpha + i\lambda(\beta + \beta^*)\left(\alpha^*\alpha - \frac{1}{2}\right) + \frac{\kappa}{2}\alpha\right)W \\
& + \frac{\kappa}{2}\frac{\partial^2 W}{\partial\alpha\partial\alpha^*} + \frac{\gamma}{2}(\overline{n}+1)\frac{\partial^2 W}{\partial\beta\partial\beta^*} \\
& + i\frac{\lambda}{8}\left(\frac{\partial^3 W}{\partial\beta\partial\alpha\partial\alpha^*} - \frac{\partial^3 W}{\partial\beta^*\partial\alpha\partial\alpha^*}\right),
\end{aligned}
\tag{2.27}
$$

where the shorthand $W = W(\alpha, \beta)$ is used for the Wigner function. Details for the calculation are supplied in Appendix A. This transformation is exact and describes the full quantum behaviour of the system.

The third order derivatives present a problem, however. If it weren't for their presence the equation would be in the form of a Fokker-Planck equation. This would allow equations of motion to be written as a set of coupled Langevin equations[1, 50]. There are two possible solutions to this conundrum. Firstly, a different transformation is possible using the Positive-P distribution [1, 53]. This does not involve third order terms and so a Fokker-Planck type equation is obtained. Unfortunately the transformation is much more complicated, and the phase space required is twice as large[1]. In this instance, the *truncated Wigner approximation* (TWA) is applied. This involves simply dropping the third order derivatives in Equation 2.27. The equation then accounts for the zero point noise in the system, but does not treat the non-linearity exactly[54]. This approximation is known to work in the case of systems close to a steady state, with linear fluctuations[1]. This requires λ to be kept small so that interactions between the cavity and resonator are relatively weak. Quantitatively, it is required that $\lambda \ll 2\omega_m$[31].

The approximated Fokker-Planck equation takes the form

$$
\begin{aligned}
\frac{dW(\alpha,\beta)}{dt} =\ & \frac{\partial}{\partial\alpha}\left[F_\alpha(\alpha,\beta)W(\alpha,\beta)\right] + \frac{\partial}{\partial\alpha^*}\left[F_{\alpha^*}(\alpha,\beta)W(\alpha,\beta)\right] \\
& + \frac{\partial}{\partial\beta}\left[F_\beta(\alpha,\beta)W(\alpha,\beta)\right] + \frac{\partial}{\partial\beta^*}\left[F_{\beta^*}(\alpha,\beta)W(\alpha,\beta)\right] \\
& + \frac{1}{2}\frac{\partial^2}{\partial\beta\partial\beta^*}\left[D_\beta(\alpha,\beta)W(\alpha,\beta)\right] \\
& + \frac{1}{2}\frac{\partial^2}{\partial\alpha\partial\alpha^*}\left[D_\alpha(\alpha,\beta)W(\alpha,\beta)\right],
\end{aligned}
\tag{2.28}
$$

where the following functions are defined:

$$
F_\alpha = i\Delta\alpha + i\lambda(\beta+\beta^*)\left(\alpha^*\alpha - \frac{1}{2}\right) + \frac{\kappa}{2}\alpha + i\Omega \tag{2.29}
$$

$$
F_{\alpha^*} = (F_\alpha)^* \tag{2.30}
$$

$$
F_\beta = i\omega_m\beta + i\lambda\left(\alpha^*\alpha - \frac{1}{2}\right) + \frac{\gamma}{2}\beta \tag{2.31}
$$

$$
F_{\beta^*} = (F_\beta)^* \tag{2.32}
$$

$$
D_\alpha = \kappa \tag{2.33}
$$

$$
D_\beta = \gamma(\overline{n}+1), \tag{2.34}
$$

where $F_{\alpha,\beta}$ describe the forces acting on the system, and $D_{\alpha,\beta}$ describe the diffusion in the system. This can be written in the equivalent form of a set of Langevin equations for variables α, α^*, β and β^*[1],

$$
\dot{\alpha} = -i\left(\Delta + \frac{\lambda}{2}(\beta+\beta^*)\right)\alpha - \frac{\kappa}{2}\alpha - i\Omega + \eta_\alpha \tag{2.35}
$$

$$
\dot{\alpha^*} = i\left(\Delta + \frac{\lambda}{2}(\beta+\beta^*)\right)\alpha^* - \frac{\kappa}{2}\alpha^* + i\Omega + \eta_{\alpha^*} \tag{2.36}
$$

$$
\dot{\beta} = -\frac{i\lambda}{2}\left(\alpha^*\alpha - \frac{1}{2}\right) - i\omega_m\beta - \frac{\gamma}{2}\beta + \eta_\beta, \tag{2.37}
$$

$$
\dot{\beta^*} = \frac{i\lambda}{2}\left(\alpha^*\alpha - \frac{1}{2}\right) + i\omega_m\beta - \frac{\gamma}{2}\beta + \eta_{\beta^*}, \tag{2.38}
$$

where fluctuations in the cavity and resonator are described by Gaussian white noise variables η_α and η_β, respectively. These noise terms are governed by the following correlators:

$$
\langle\eta_\alpha(t)\eta_{\alpha^*}(t')\rangle = \frac{\kappa}{2}\delta(t-t'), \tag{2.39}
$$

$$
\langle\eta_\beta(t)\eta_{\beta^*}(t')\rangle = \frac{\gamma}{2}(2\overline{n}+1)\delta(t-t'). \tag{2.40}
$$

All other correlators are zero. Equations 2.35 to 2.38 are coupled, non-linear equations, which cannot be solved exactly. In

the following, solutions are derived via a series of approxima-
tions, consistent with a weakly coupled system, where $\lambda \ll 2\omega_m$.

2.3.1 *Analysis of Langevin equations*

Analysis of the resonator dynamics requires a decoupled equa-
tion for β. In order to proceed, additional approximations are
required. Equations 2.35 to 2.38 are analysed by exploiting the
separation of time-scales in the cavity and resonator dynam-
ics. The damping in the cavity determines the time-scale over
which oscillations in the optical mode relax, and is significantly
higher than both the mechanical damping and the coupling be-
tween the modes: $\kappa \gg \gamma, \lambda$. The cavity therefore loses energy
via dissipation on a much faster timescale than energy is trans-
ferred to or lost from the resonator, and over the timescale of
cavity relaxation, any variations in the mechanical amplitude
are small. One can therefore describe the cavity dynamics with
respect to a mechanical mode which oscillates at a fixed fre-
quency with a constant amplitude[41]. This amounts to the
ansatz $\beta = \beta_c + Be^{-i\phi}e^{-i\omega_m t}$, where ϕ and B are treated as con-
stants, and β_c is a constant shift in the origin of the resonator,
which is yet to be evaluated. Equation 2.35 then reads

$$\dot{\alpha} = -i\left(\Delta' + \lambda B \cos\left(\phi + \omega_m t\right)\right)\alpha - i\Omega - \frac{\kappa}{2}\alpha + \eta_\alpha, \quad (2.41)$$

where $\Delta' = \Delta + \lambda \Re[\beta_c]$ is the detuning including a frequency
shift brought about by the fixed point displacement of the res-
onator, β_c. By making a further substitution, $\tilde{\alpha} = \alpha e^{iz\sin(\phi+\omega_m t)}$,
where $z = \frac{\lambda B}{\omega_m}$, one can isolate the oscillating terms in the rotat-
ing frame of $\tilde{\alpha}$,

$$\frac{d\tilde{\alpha}}{dt} = -i\Delta'\tilde{\alpha} - i\Omega e^{iz\sin(\phi+\omega_m t)} - \frac{\kappa}{2}\tilde{\alpha} + \tilde{\eta}_\alpha, \quad (2.42)$$

where $\tilde{\eta}_\alpha = \eta_\alpha e^{iz\sin(\phi+\omega_m t)}$.

After a Fourier Transform and some rearranging, a solution
for $\tilde{\alpha}(\omega)$ takes the form

$$\tilde{\alpha}(\omega) = \frac{-i\Omega}{i(\omega + \Delta') + \frac{\kappa}{2}} \int_{-\infty}^{\infty} dt' e^{-i(\omega t' - z\sin(\omega_m t') - \omega\phi/\omega_m)}$$
$$+ \frac{\tilde{\eta}_\alpha(\omega)}{i(\omega + \Delta') + \frac{\kappa}{2}}. \quad (2.43)$$

By applying the Jacobi-Anger expansion[55], the integral is evaluated,

$$\tilde{\alpha}(\omega) = \frac{-i\Omega \sum_n J_n(z) e^{i\phi n}}{\frac{\kappa}{2} + i(\omega + \Delta')} \delta(\omega + \omega_m n) + \frac{\tilde{\eta}_\alpha(\omega)}{\frac{\kappa}{2} + i(\omega + \Delta')}, \quad (2.44)$$

where $\sum_n J_n(z)$ denotes a sum over bessel functions of the first kind, $J_n(z)$, over the limits $n = -\infty$ to $n = \infty$. The first term in Equation 2.44 can be identified as an average, $\langle \tilde{\alpha} \rangle$, and the second as the fluctuating part, $\delta\tilde{\alpha}$. A similar expression is derived for $\tilde{\alpha}^*$, where $\tilde{\alpha}^*(\omega) = \alpha^*(\omega) e^{-iz\sin(\phi + \omega_m t)}$:

$$\tilde{\alpha}^*(\omega) = \frac{i\Omega \sum_n J_n(z) e^{-i\phi n}}{\frac{\kappa}{2} + i(\omega - \Delta')} \delta(\omega + \omega_m n) + \frac{\tilde{\eta}_\alpha^*(\omega)}{\frac{\kappa}{2} + i(\omega - \Delta')}. \quad (2.45)$$

Note that, after a Fourier transform, $\tilde{\alpha}^*(\omega)$ and $\tilde{\alpha}(\omega)$ are no longer complex conjugates of one another.

2.3.2 *Damping due to back action*

Turning now to Equation 2.37, analysis of the mechanical mode requires one to evaluate the term $\alpha^*\alpha - 1/2$. In order to so, recall the assumptions made when applying the TWA. In dropping the third order differentials, an accurate picture of the zero-point noise in the system is acquired, at the cost of describing the non-linearity exactly. This works well when fluctuations are weak, and so one can write $\alpha = \langle \alpha \rangle + \delta\alpha$, and approximate $\delta\alpha\delta\alpha^*$ by its average, $\langle \delta\alpha\delta\alpha^* \rangle = \frac{1}{2}$. Doing this (as described in Appendix B), one finds

$$\alpha^*\alpha - \frac{1}{2} = \langle \alpha^* \rangle \langle \alpha \rangle + \langle \alpha \rangle \delta\alpha^* + \langle \alpha^* \rangle \delta\alpha, \quad (2.46)$$

This term describes the resonator dynamics arising from the coupling to the cavity mode. It is composed of an average and fluctuating dynamics, which can be treated separately. Turning attention to the average dynamics, the resonator amplitude evolves according to

$$\langle \dot{\beta} \rangle = -\left(i\omega_m + \frac{\gamma}{2} \right) \langle \beta \rangle - i\frac{\lambda}{2} \langle \alpha^* \rangle \langle \alpha \rangle. \quad (2.47)$$

The last term in Equation 2.47 can be evaluated via a Fourier transform,

$$\langle \alpha^* \rangle \langle \alpha \rangle (\omega) = \Omega^2 \sum_{n,n'} \frac{J_n(z) J_{n'}(z) \delta\left(f_{n,n'}(\omega) \right) e^{-i\phi(n-n')}}{h_n^*(h_n + i\omega)}, \quad (2.48)$$

where it has been noted that $\langle \alpha^* \rangle \langle \alpha \rangle (\omega) = \langle \tilde{\alpha}^* \rangle \langle \tilde{\alpha} \rangle (\omega)$, and the quantities h_n and $f(\omega)$ have been defined:

$$h_n = \frac{\kappa}{2} + i(\omega_m n + \Delta') \tag{2.49}$$

$$f_{n,n'}(\omega) = \omega + \omega_m(n - n'). \tag{2.50}$$

Analysis of the centre of the limit cycle, β_c is immediately possible, by isolating the non rotating terms in Equation 2.47,

$$\beta_c = -i\frac{\lambda}{2}\frac{\langle \alpha^* \rangle \langle \alpha \rangle (\omega = 0)}{i\omega_m + \frac{\gamma}{2}}, \tag{2.51}$$

where $\langle \alpha^* \rangle \langle \alpha \rangle (\omega = 0)$ denotes the non rotating term in the sum of Equation 2.48. When $\omega = 0$ the delta function isolates the term $n' = n$ in the sum over n' to give

$$\beta_c = -\frac{\lambda\Omega^2}{2\omega_m - i\gamma}\sum_n \frac{J_n^2(z)}{\frac{\kappa^2}{4} + (\omega_m n + \Delta')^2}. \tag{2.52}$$

Switching attention, now, to the oscillating parts of Equation 2.47, a rotating wave approximation[56] (RWA) is applied. This isolates terms in the sum of Equation 2.48 that oscillate near the mechanical frequency, since higher frequency oscillations at $n\omega_m$ (where $n > 1$) will produce negligible contributions when the average is taken over a long enough timescale. These terms are therefore discarded so that Equation 2.53 can then be written

$$\langle \dot{\beta} \rangle = -i(\omega_m + \delta\omega)\langle \beta \rangle - \frac{1}{2}(\gamma + \gamma_{BA})\langle \beta \rangle, \tag{2.53}$$

where the damping due to the cavity back action, γ_{BA}, and frequency shift, $\delta\omega$, are identified as the real and imaginary parts of the truncated sum in Equation 2.48. The discarding of higher order oscillations in ω_m amounts to picking out terms in the sum where $n' - n = 1$, giving

$$\frac{\gamma_{BA}}{2} + i\delta\omega = -\frac{i\lambda\Omega^2}{2B}\frac{\sum_n J_n(z)J_{n+1}(z)}{h_n^* h_{n+1}}. \tag{2.54}$$

Taking the real and imaginary parts, the damping and frequency shift are then expressed in terms of z,

$$\gamma_{BA}(z) = -\sum_n \frac{\lambda^2\Omega^2\kappa}{2z}\frac{J_n(z)J_{n+1}(z)}{|h_n|^2|h_{n+1}|^2} \tag{2.55}$$

$$\delta\omega(z) = \sum_n \frac{\lambda^2\Omega^2}{2\omega_m z}\frac{J_n(z)J_{n+1}(z)}{|h_n|^2|h_{n+1}|^2}. \tag{2.56}$$

These two expressions are thus amplitude dependent, a property which will be investigated in later sections. It should be noted that the approximation in making the ansatz $\beta = \beta_c + Be^{-i(\omega_m t + \phi)}$ neglects variations in frequency, which are then calculated in the form of $\delta\omega(z)$. The calculation is not done self consistently as $\delta\omega(z)$ is found to be several orders of magnitude smaller than ω_m for the parameters of interest. This results in relative errors of around 10^{-5} when calculating $\gamma_{BA}(z)$, and so the correction is ignored.

2.3.3   *Classical dynamics of limit cycles*

Equation 2.53 describes the average dynamics of the resonator, leading to a classical equation of motion for the amplitude B:

$$\langle \dot{B} \rangle = -\frac{\gamma_T(B)}{2} \langle B \rangle, \tag{2.57}$$

where the total damping is written $\gamma_T(B) = \gamma + \gamma_{BA}(B)$. Two types of steady state solution, B_0, are possible to satisfy Equation 2.57:

(i) $B_0 = 0$: a 'fixed point' state, where the resonator fluctuates around a central point, β_c.

(ii) $B_0 \neq 0$: a 'limit cycle' state, where the resonator oscillates with a constant amplitude about β_c.

Both of these obey the condition

$$(\gamma + \gamma_{BA}(B_0)) B_0 = 0. \tag{2.58}$$

Note that $B_0 = 0$, the state corresponding to a fixed point, is always a solution (though not necessarily a stable one). One can obtain solutions for limit cycles, $B_0 \neq 0$, for a given set of parameters by finding the intersections between curves of γ and $\gamma_{BA}(B)$. Figure 2.2 shows such an intersection. The stability of a solution is determined by analysing the effect of small deviations from B_0. For example, consider a solution to Equation 2.58, where $B = B_0$. Taking a point $B = B_0 + \delta B$, arbitrarily close to B_0, the rate of change is given by expanding Equation 2.57 about B_0, for small changes δB:

$$\dot{B} = -\frac{1}{2}(\gamma + \gamma_{BA}(B_0 + \delta B))(B_0 + \delta B) \tag{2.59}$$

$$\dot{\delta B} = -\frac{1}{2}(\gamma + \gamma_{BA}(B_0))\delta B - \frac{d\gamma_{BA}}{dB}\bigg|_{B_0} B_0 \delta B, \tag{2.60}$$

where the first term on the left hand side determines the fixed point stability and the final term determines the limit cycle stability. In order for a small change to bring the system back to the solution at B_0, it is required that $\delta \dot{B}$ have opposite sign to δB. This provides the following stability conditions:

[i]For a fixed point, require $\gamma + \gamma_{BA}(0) > 0$.

[ii]For a limit cycle, require $d\gamma_{BA}/dB > 0$.

For the case shown in Figure 2.2, there is a stable solution at $B = 7.4$. For this set of parameters it is the only stable solution for the amplitude.
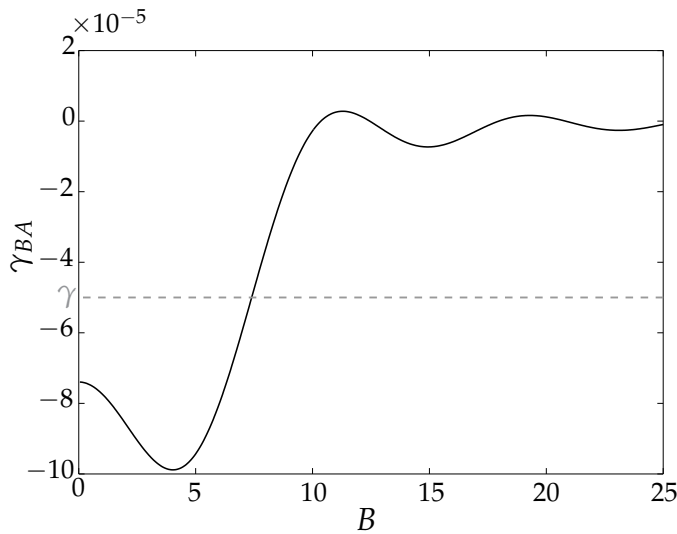
Figure 2.2: Estimation of limit cycles by plotting $\gamma_{BA}(B)$ (solid line) and finding intersects with $-\gamma$ (dotted line), for $\Delta/\omega_m = -1$. Since the intersection occurs where $d\gamma_{BA}/dB > 0$, the limit cycle is stable. In this case the value of $\gamma_{BA}(0)$ is negative, hence the fixed point state is not stable. Parameters are $\omega_m = 1$, $\lambda = 0.4$, $\Omega = 0.05$, $\kappa = 1$ and $\gamma = 5 \times 10^{-5}$, and are discussed in Section 2.4.

2.3.4 *Diffusion*

Analysis so far has concentrated largely on the average dynamics of the system, which describe the effect of the forces on the resonator. Whilst this offers insight into stabilities in the resonator dynamics, it is not the full picture. Fluctuations in the system arise from the finite temperature of the the resonator, as well as fluctuations in the cavity. These become important when

calculating statistical averages. Given that $|\beta|^2 = B^2$, Equation 2.37 can be expressed in terms of the energy, $E = B^2$:

$$\dot{E} = -\gamma_T E + 2\sqrt{E}\eta_T, \qquad (2.61)$$

where the fluctuations are expressed as a single term, η_T, given by

$$\eta_T = \left(\eta_\beta e^{i(\omega_m t + \phi)} + \eta_{\beta^*} e^{-i(\omega_m t + \phi)}\right) + \eta_{BA}(t), \quad (2.62)$$

and

$$\eta_{BA}(t) = \left(\eta_{eff} + \eta_{eff}^*\right)\sin\left(\omega_m t + \phi\right), \qquad (2.63)$$

where η_{eff} are the fluctuations arising from coupling to the cavity, given by

$$\eta_{eff} = \frac{\lambda}{2}\langle\alpha^*\rangle\delta\alpha, \qquad (2.64)$$

which is a function of the cavity noise, η_α. Using Equation 2.44 and 2.45, expressions for the $\eta_{eff}(\omega)$ and $\eta_{eff}^*(\omega)$ are found using the convolution theorem:

$$\langle\alpha^*\rangle\delta\alpha(\omega) = i\Omega\sum_n \frac{J_n(z)e^{-i\phi n}\tilde{\eta}_{\alpha^*}(\omega + \omega_m n)}{h_n^*(h_n + i\omega)}, \qquad (2.65)$$

$$\langle\alpha\rangle\delta\alpha^*(\omega) = -i\Omega\sum_n \frac{J_n(z)e^{i\phi n}\tilde{\eta}_{\alpha^*}(\omega - \omega_m n)}{h_n(h_n^* + i\omega)}. \qquad (2.66)$$

The diffusion coefficient, $D_T = D_{th} + D_{BA}$ contains a contribution from thermal fluctuations and cavity fluctuations, respectively. An effective diffusion constant, valid on time-scales much longer than ω_m and κ, is obtained from the zero frequency component of the noise correlation function, averaged over a mechanical period. It can be expressed as

$$D_T = \lim_{\omega\to 0}\frac{\omega_m}{2\pi}\int_0^{\frac{2\pi}{\omega_m}}\mathrm{dt}\int_{-\infty}^{\infty}\mathrm{d}\omega' e^{i(\omega+\omega')t}\langle\eta_T(\omega)\eta_T(\omega')\rangle. \quad (2.67)$$

The separate terms D_{th} and D_{BA} arise because η_{eff} and η_{eff}^* do not correlate with η_β and η_{β^*}. The correlator can therefore be split into the two separate terms. The result is

$$D_{th} = \frac{\gamma}{2}\left(\bar{n} + \frac{1}{2}\right), \qquad (2.68)$$

$$D_{BA} = \lim_{\omega\to 0}\frac{\omega_m}{\pi}\int_0^{\frac{\omega_m}{\pi}}\mathrm{dt}\int_{-\infty}^{\infty}\mathrm{d}\omega'\langle\eta_{BA}(\omega)\eta_{BA}(\omega')\rangle e^{i(\omega+\omega')t}. \quad (2.69)$$

Evaluation of the right hand side of Equation 2.69 leads to the final result,

$$D_{BA}(z) = \frac{\Omega^2 \lambda^2 \gamma}{8} \sum_n \frac{1}{|h_n|^2} \left| \frac{J_{n+1}(z)}{h_{n+1}} - \frac{J_{n-1}(z)}{h_{n-1}} \right|^2, \quad (2.70)$$

where $z = \lambda \sqrt{E}/\omega_m$.

2.3.5 *Probability distribution of resonator energy*

A comparison to numerical calculations can be provided by calculating the probability distribution for the resonator energies. Equation 2.61 takes the form of a Langevin equation allowing an equivalent Fokker-Planck equation to be deduced in terms of the probability $P(E, t)$ of the resonator being found in a state with energy E.

$$\frac{\partial}{\partial t} P(E, t) = -\frac{\partial}{\partial E} \left(\frac{1}{2} \gamma_T(E) E P(E, t) \right)$$

$$+ \frac{1}{2} \frac{\partial^2}{\partial E^2} \left(E D_T(E) P(E, t) \right). \quad (2.71)$$

The steady state probability distribution can be found by setting the time differential to zero. The solution takes the form

$$P(E) \propto e^{-U(E)}, \quad (2.72)$$

where the potential $U(E)$ is defined[1]

$$U(E) = \int_0^E dE' \frac{\gamma_T(E')}{D_T(E')} \quad (2.73)$$

Equations 2.72 and 2.73 give some insight into the form of the probability distribution. One expects to observe peaks in $P(E)$ at $E_0 = B_0^2$, if B_0 satisfies the energy balance condition, Equation 2.58. These solutions correspond to minima in the potential, $U(E)$. In the following, $\langle E \rangle$ is investigated, which relates to the average phonon number, $\langle n \rangle = \langle b^\dagger b \rangle$, by Equation 2.26,

$$\langle E \rangle = \langle n \rangle + \frac{1}{2}. \quad (2.74)$$

---

1 Note that a small correction to the numerator arising from noise terms is neglected here[31].

2.3.6 *Cooling regime*

The probability distribution of Equation 2.72 is complicated and contains an integral which is not easily evaluated. However, under certain circumstances, one can make further approximations which allow Equation 2.72 to be explored analytically, before a numerical approach is necessary. The regime of cooling has been investigated extensively in recent years[57, 34, 45]. When the cavity is driven below its resonant frequency, it is possible to enter a regime where energy is extracted from the resonator. This is of interest when one wishes to cool a resonator to its quantum mechanical ground state, a feat achieved in recent years[13, 14]. In this regime the damping is positive and the resonator is known to remain in a state where it fluctuates about the fixed point. This allows the assumption that $z \ll 1$, which leads to the approximate expansion of the Bessel functions[58]:

$$J_n(z) \approx \frac{1}{n!} \left(\frac{z}{2} \right)^n.$$ (2.75)

From this, approximate expressions for the damping and diffusion can be deduced, by taking $\gamma_{BA} \approx \gamma_{BA}(0)$, $D_{BA} \approx D_{BA}(0)$ and isolating terms in the sum which give the highest contribution:

$$\gamma_{BA}(0) \approx \frac{\lambda^2 \Omega^2 \omega_m \Delta' \kappa}{\left[\frac{\kappa^2}{4} + \Delta'^2 \right] \left[\frac{\kappa^2}{4} + (\omega_m + \Delta')^2 \right] \left[\frac{\kappa^2}{4} + (\omega_m - \Delta')^2 \right]}$$ (2.76)

$$D_{BA}(0) \approx \frac{4\lambda^2 \Omega^2 \kappa \left[\frac{\kappa^2}{4} + \omega_m^2 + \Delta'^2 \right]}{\left[\frac{\kappa^2}{4} + \Delta'^2 \right] \left[\frac{\kappa^2}{4} + (\omega_m + \Delta')^2 \right] \left[\frac{\kappa^2}{4} + (\omega_m - \Delta')^2 \right]}.$$ (2.77)

The thermal diffusion is written in terms of the intrinsic damping and thermal phonon number, $D_{th} = \gamma(\bar{n} + \frac{1}{2})$. The back action contribution to the diffusion can be written in a similar way:

$$D_{BA}(0) = \gamma_{BA}(0) \left(n_{BA} + \frac{1}{2} \right),$$ (2.78)

where n_{BA} is the back action contribution to the phonon number in the resonator. In the case of cooling, this takes the form

$$n_{BA} = \frac{\frac{\kappa^2}{4} + (\omega_m - \Delta')^2}{4\omega_m \Delta'}.$$ (2.79)

The probability distribution is then

$$P(E) \propto e^{-\frac{(\gamma+\gamma_{BA}(0))E}{\gamma_{BA}(0)\left(n_{BA}+\frac{1}{2}\right)+\gamma\left(\overline{n}+\frac{1}{2}\right)}}, \qquad (2.80)$$

which decays exponentially in E. Equation 2.80 takes the form of a Wigner distribution for a harmonic oscillator in a thermal state (after integrating out the phase)[31, 1], with thermal occupation number

$$n_{eff} = \frac{\gamma_{BA}(0)n_{BA} + \gamma\overline{n}}{\gamma_{BA}(0) + \gamma}. \qquad (2.81)$$

Figure 2.3 compares the probability distributions obtained via the full analytic calculation (Equation 2.72) and the small z approximation (Equation 2.80). Parameters chosen are $\omega_m = 10$, $\Delta = 20$, $\lambda = 1$, $\Omega = 0.05$, $\gamma = 5 \times 10^{-5}$, $\overline{n} = 0.001$, $\kappa = 1$ so that the resonator is well into the regime of cooling and $z \ll 1$ over the range of the peak. The approximation works very well, with minor discrepancies highlighted via the logarithmic plot in the inset.
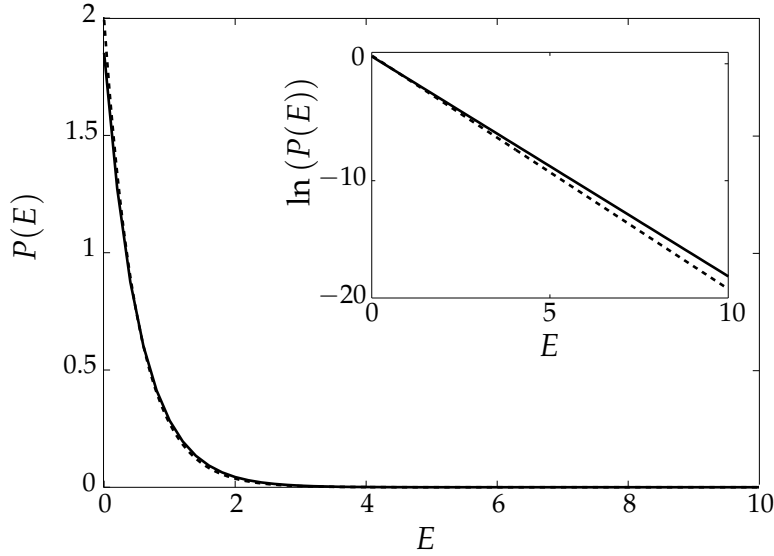
Figure 2.3: Small z approximation for $P(E)$, relevant in the regime of cooling (dashed). This is compared with Equation 2.72 (solid), for parameters $\omega_m = 10$, $\Delta = 20$, $\lambda = 1$, $\Omega = 0.05$, $\gamma = 5 \times 10^{-5}$, $\overline{n} = 0.001$, $\kappa = 1$. Inset shows the same comparison on a logarithmic scale.

Note that, in the case of sideband cooling, $\Delta = \omega_m$, one can deduce a limit on the minimum effective phonon number:

$$n_{eff} = \left(\frac{\kappa}{4\omega_m}\right)^2, \qquad (2.82)$$

where one requires heavy damping such that $\gamma_{BA} \gg \gamma$, so that $n_{eff} \approx n_{BA}$. This will be discussed in more detail in Chapter 4.

2.3.7 *Gaussian approximation in the limit cycle regime*

In addition to the regime of low energies, the semi-classical analytic approach can be used to model the dynamics well within the limit cycle regime, where fixed amplitude oscillations dominate the resonator motion, and fluctuations are small. In this regime, the probability distribution forms a peak, with a very small spread around the point E_0, which satisfies Equation 2.58. With this in mind, the potential $U(E)$ can be approximated by an expansion, up to second order, about that energy:

$$U(E) \; \simeq \; U(E_0) + \frac{1}{2}(E - E_0)^2 \frac{\frac{\mathrm{d}\gamma_{BA}}{\mathrm{d}E}\big|_{E_0}}{D_{BA}(E_0) + D_{th}}. \quad (2.83)$$

This gives a Gaussian probability distribution of the form

$$P(E) \;\; = \;\; \frac{e^{-(E-E_0)^2/2\sigma^2}}{2\sigma^2\sqrt{2\pi}}, \quad (2.84)$$

where

$$\sigma^2 = \frac{D_{BA}(E_0) + D_{th}}{\frac{\mathrm{d}\gamma_{BA}}{\mathrm{d}E}\big|_{E_0}}. \quad (2.85)$$

2.4 NUMERICAL ANALYSIS

In this section Equation 2.21 is solved directly, for a fixed number of cavity and resonator states. Details of how the numerical calculations are performed are given in Appendix C. Analysis to follow will characterise the resonator dynamics by calculating four different quantities: the probability distribution, $P(n) = \langle n|\hat{\rho}|n\rangle$, for the number of phonons in the resonator; the average phonon number $\langle n\rangle$; the Fano factor, F, defined by $F = (\langle n^2\rangle - \langle n\rangle^2)/\langle n\rangle$, which measures the spread in the probability distribution; the Wigner function, $W(\beta)$. Each of these follows from the numerically calculated steady state density matrix, ρ.

The behaviour of these quantities will be described as the laser detuning, Δ, and optomechanical coupling, λ, are varied. These two parameters control the energy exchange between the cavity and resonator. When $\Delta = 0$, the laser is in resonance with

the cavity mode and photons build up the cavity[13]. Here no significant exchange of energy occurs with the resonator. As the detuning is increased above(below) resonance, it is expected that phonons would be created(extracted) as the resonator is driven (damped). As the detuning is swept, transitions are expected between different dynamical states of the resonator. The optomechanical coupling determines the strength of this interaction.

Numerics are produced for the following sets of parameters:

[i]$\omega_m = 1, \lambda = 0.4, \gamma = 5 \times 10^{-5}$,

[ii]$\omega_m = 5, \lambda = 1.5, \gamma = 3 \times 10^{-5}$,

[iii]$\omega_m = 5, \lambda = 2, \gamma = 3 \times 10^{-5}$,

and units are adopted such that $\kappa = 1$ is set throughout the calculation. The first two sets of parameters involve the good $(\omega_m/\kappa \gg 1)$ and bad $(\omega_m/\kappa \approx 1)$ cavity regimes. In the good cavity regime the resonances which occur for $\Delta = l\omega_m$, with l an integer, lead to separate peaks which can be distinguished from one another and the main cavity resonance at $\Delta = 0$. In the bad cavity regime the resonances overlap and energy transfer occurs over a broad range of Δ values. The third set of parameters explores the regime of stronger optomechanical coupling.

The parameters are selected to give a distribution of states where higher energy modes are unoccupied, so that a small, finite number of cavity and resonator modes are modelled. For this reason, a weak driving strength and low temperature are required. For each set of parameters $\Omega = 0.05$ and $\overline{n} = 0$ are used.

2.4.1 *Results in 'Bad cavity' limit*

Figure 2.4 shows the average phonon number and Fano factor as the detuning is swept for the bad cavity case, [i]. A single resonance peak occurs, where the $l = 0, -1, -2$ peaks merge due to the broadening. The broadening has the effect of adding uncertainty to the energy transfer condition, $\Delta = l\omega_m$, so that a wider spread of Δ values satisfy the condition, and $\langle n \rangle$ is finite over a broader range. The merging of the peaks allows multiple photons to be absorbed in certain regions of the curve, creating a skewed peak, with a sudden decrease in $\langle n \rangle$ near $\Delta \approx -2\omega_m$. The shape of the curve is understood by examining the Wigner function at various points along the curve. There

are three distinct dynamical states seen in the resonator, given in Figure 2.5. Sweeping through Δ and λ reveals transitions between these states.
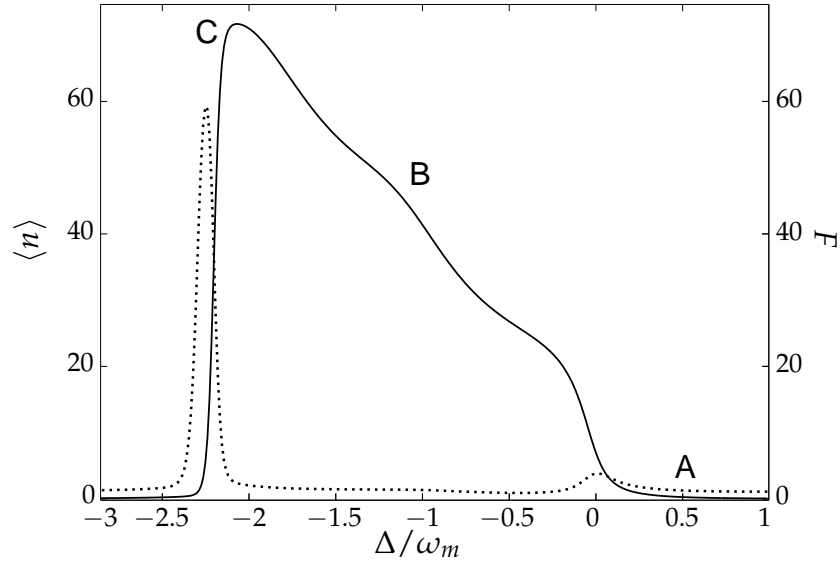
Figure 2.4: Average phonon number (solid) and Fano factor (dotted) with respect to detuning for the parameters of case [i]. Labels *A*, *B* and *C* refer to the three distinct states in the resonator, shown by Wigner functions in Figure 2.5.

Figure 2.5a shows the Wigner function at point A in Figure 2.4, where the resonator is in a fixed point state. This is characterised by a probability distribution concentrated on a central point. The slight spread indicates small fluctuations, which grow as the detuning is made more negative, causing the probability density to spread out, thinning at the centre, to eventually form a limit cycle. At point B, The Wigner function takes the form of a ring of probability density, illustrated in Figure 2.5b. The limit cycle state involves stable oscillations at a fixed amplitude about a central point[15, 31]. The transition from fixed point to limit cycle is smooth, so that the amplitude increases continuously from zero. This results in a small peak in *F*. Here the fluctuations cause a slight broadening in the distribution, without any discontinuities as $\langle n \rangle$ increases smoothly.

The transition at C is clearly marked by a large peak in the Fano factor and a sharp fall in $\langle n \rangle$. This indicates a sudden increase in the spread of the distribution. Here the resonator has a finite probability of being in either a fixed point or limit cycle state, with the Wigner function shown in Figure 2.5c. Fluctuations cause the resonator to switch between the two states with
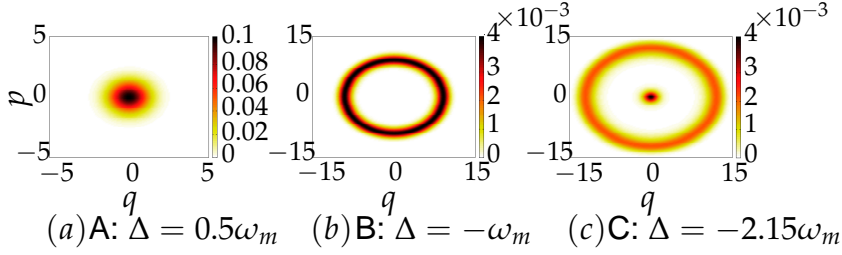
Figure 2.5: Wigner functions for the resonator, in terms of variables $q = (\beta + \beta^*)/\sqrt{2}$ and $p = (\beta - \beta^*)/\sqrt{2}i$, for (a) point A, (b) point B and (c) point C, as labelled in Figure 2.4. Three distinct states are observed in the resonator's motion.

widely separated energies, giving a large peak in F and a sharp drop in $\langle n \rangle$, as two very different amplitudes are averaged over. In classical terms, one can think of this type of state as bistable, with both a low and a high energy state accessible to it.

A similar set of transitions are observed in the resonator when the coupling is swept. Figure 2.6 shows $\langle n \rangle$ and F with respect to λ for $\Delta = -\omega_m$, with the remaining variables identical to those in case [i]. The resonator makes a smooth transition between a fixed point at X and limit cycle state at Y, marked by a sharp peak in F. The phonon number peaks before gradually decreasing as the limit cycle gradually collapses. This happens over a much broader range in λ compared to the collapse of the limit cycle in Figure 2.4, where the fixed point emerges. In Figure 2.6 the increase in λ past point Y induces the emergence of an additional limit cycle, resulting in an increase in F around $\lambda = 0.7$.

2.4.2 Results for resolved sideband ('good cavity') limit

When the mechanical frequency is increased, one finds a situation where $\omega_m > \kappa$, and the system approaches the resolved sideband limit, where resonances in the mechanical energy spectrum are resolved and a strong transfer of energy between the resonator and cavity occurs in regions focused on the resonances, $|\Delta| = l\omega_m$. Figure 2.7 shows the average phonon number and Fano factor as the detuning is swept for the parameters of case [ii]. In contrast to Figure 2.4, the main resonance peak is sharp, and separated from the secondary peak at $l = 0$ by a region where $\langle n \rangle \approx 0$.

The $l = 0$ peak is accompanied by a peak in F, though no bistability occurs in this region of the graph. The large fluctuations are due to noise in the cavity. In this region the cavity
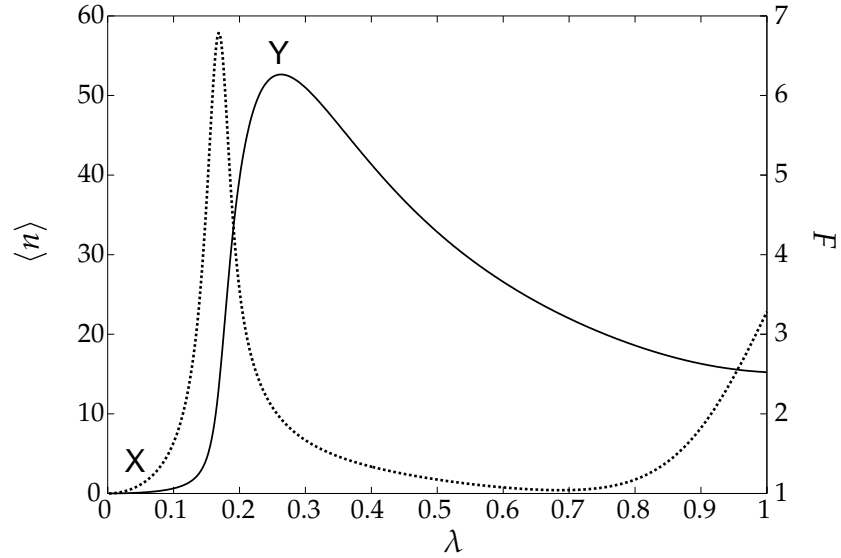
Figure 2.6: Average phonon number (solid) and Fano factor (dotted) with respect to coupling, λ, for parameters in set [i] with $\Delta = -1$. Points X and Y mark the fixed point and limit cycle states, respectively.
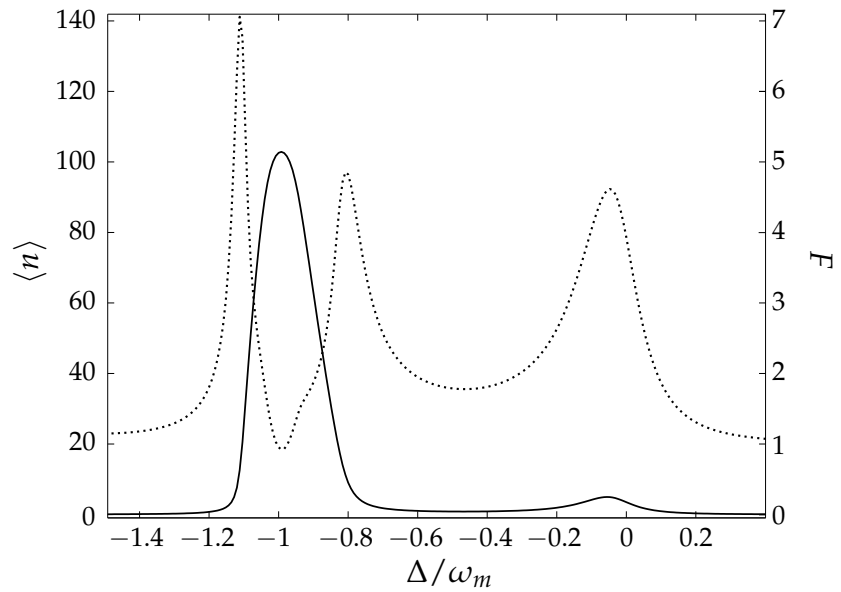
Figure 2.7: Average phonon number (solid) and Fano factor (dotted) with respect to detuning, Δ, approaching the resolved sideband limit, $\omega_m = 5$.

mode is strongly driven, and the occupation is large. Since the diffusion in the resonator is proportional to $\langle \alpha \rangle$ (via Equation 2.70) this causes a peak in F.

A notable difference between the parameters of set [ii], compared to set [i], is the absence of a bistability. The Fano factor peaks at $\Delta = -0.8\omega_m$ and $\Delta = -1.1\omega_m$, where the large fluctuations mark the transition between a limit cycle and fixed point. The transition is smooth, however. At $\Delta \approx 0.8$ the limit cycle emerges, with increasing energy as Δ increases, up to where $\langle n \rangle$ peaks, before gradually decreasing in energy until the fixed point state is recovered. This results in the symmetric resonance peak in Figure 2.7.

Figure 2.8 shows the result of an increased coupling strength (case [iii]). With increased coupling a further resonance at $l = 2$ is observable, and produces the strongest peak in $\langle n \rangle$. Within the region of this resonance, the transitions between fixed point and limit cycle states occur with bistabilities. This is evident from the order of magnitude increase in the Fano factor peaks, compared with the transitions near $l = 0$ and $l = 1$.
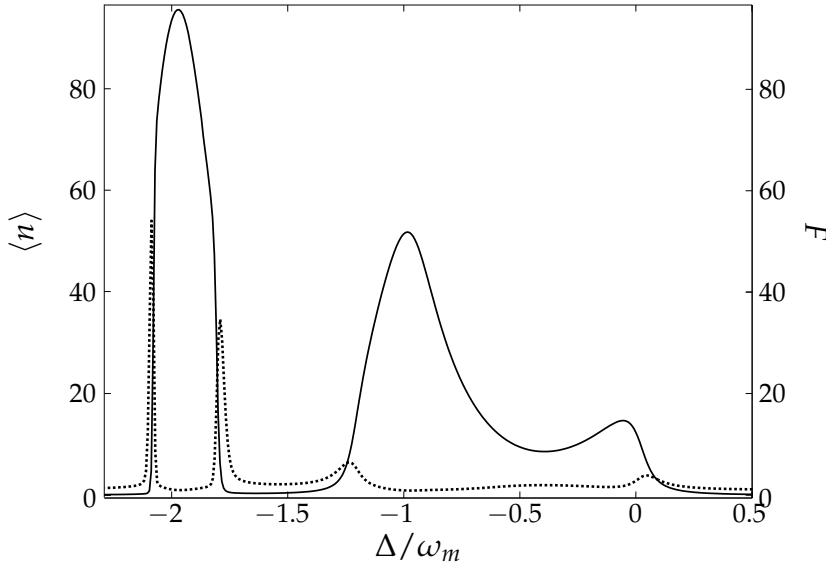
Figure 2.8: Average phonon number (solid) and Fano factor (dotted) with respect to detuning, Δ for $\omega_m = 5$ and $\lambda = 2$.

2.4.3 *Results for strong coupling regime*

As the coupling is increased, non-linear effects become stronger and non classical behaviour emerges[10, 12, 43, 59]. A good indicator of this is seen in the Fano factor, which drops below unity[10, 30, 31]. Figure 2.9 shows the Fano factor as λ is swept for $\omega_m = 3.33$, $\Delta = 0$, $\lambda = 2.8$, $\Omega = 0.333$, $\gamma = 3.33 \times 10^{-4}$,

$\kappa = 1, \bar{n} = 0$. Near point A the resonator falls into a limit cycle and Fano factor drops to a minimum (see Figure 2.10a). The limit cycle state is marked by small amplitude fluctuations. Values of $F \leq 1$ indicate sub-Poissonian states (number squeezing)[12].
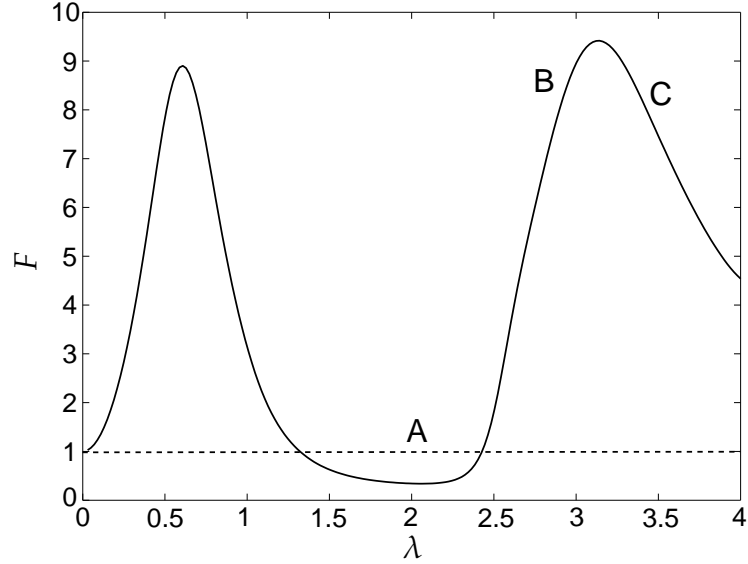
Figure 2.9: The Fano factor in the strong coupling regime, with points of interest labelled A, B and C. Parameters used are $\omega_m = 3.33$, $\Delta = 0$, $\Omega = 0.333$, $\gamma = 3.33 \times 10^{-4}$, $\kappa = 1, \bar{n} = 0$.

As the coupling is increased, two competing effects occur, shown in plots of $P(n)$ (Figure 2.10). Whilst the limit cycle becomes narrower, the emergence of an additional limit cycle at higher n, causes F to increase (point B). As this merges with the original limit cycle, the Fano factor drops (point C). Though F appears to increase due to the additional peaks, number squeezing still occurs in the original peak, which can manifest itself as negative Wigner densities[12]. Figure 2.11a shows the point labelled

(a)A: $\lambda = 2.05$ (b)B: $\lambda = 2.8$ (c)C: $\lambda = 3.5$
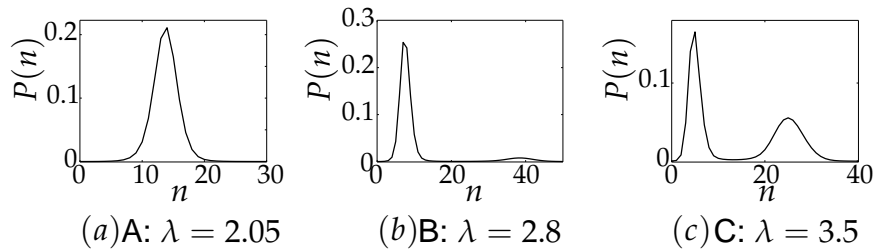
Figure 2.10: Strong coupling regime explored via $P(n)$ distributions in at points A, B and C of Figure 2.9.

B in Figure 2.9, where bright circles just below the limit cycle amplitude mark negative Wigner densities.

(a)   (b)
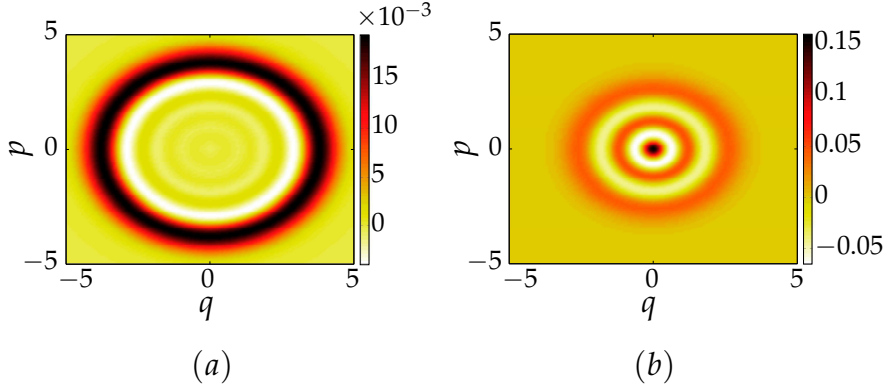
Figure 2.11: Wigner functions, showing non-classicality: (a) For the resonator, with $\omega_m = 3.33$, $\Delta = 0$, $\lambda = 2.8$, $\Omega = 0.333$, $\gamma = 3.33 \times 10^{-4}$, $\kappa = 1$, $\bar{n} = 0$, where bright rings at amplitudes below the limit cycle indicate negativity. (b) $n = 4$ Fock state, for comparison.

The presence of negative regions and a low Fano factor is reminiscent of the Fock state, or number state. An example of the Wigner function of such a state is illustrated in Figure 2.11b. This shows a resonator number state in the $n = 4$ Fock state. The negative regions lie in rings, between rings of positive peaks.

2.4.4 *Comparison between numerical and analytic calculations*

Attention is now turned to investigating how well the truncated Wigner approach described in Section 2.3.5 works by comparing the results from the probability distribution $P(E)$ to those obtained by solving the master equation numerically. Figure 2.12 shows the average phonon number and Fano factor, as calculated analytically (in blue) alongside numerical results (in black). There is very good agreement between the two curves, apart from a small shift in Δ. This shift is corrected, by manually adding in a frequency shift $\tilde{\Delta} = \Delta - \lambda^2/(4\omega_m)$. The shifted result is shown by the dashed line, resulting in two very closely matched curves. This correction does not follow from the analytic model and suggests a limitation due to the inexact treatment of the non-linearity[31].

The probability distribution from Equation 2.72 can be compared to the numerical calculation, for a limited range of parameters. A probability distribution for the phonon number, $P(n)$,
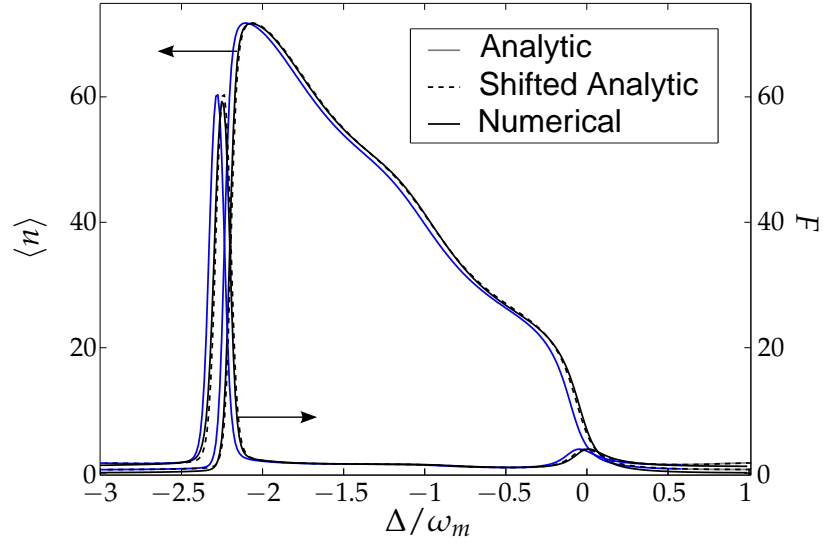
Figure 2.12: Comparison of analytic (blue) and numerical (solid black) calculations, along side a shifted analytic calculation (dashed). Parameters are those of case [i], shown in Figure 2.4.

is obtained from the density operator, $P(n) = \langle n|\hat{\rho}|n\rangle$. The two quantities are not equivalent; $P(E)$ is a continuous distribution on resonator energies whilst $P(n)$ describes the discrete distribution of phonon numbers. A simple comparison of these quantities is only appropriate when $n \gg 1$, as the distinction between the two becomes less important. The case of limit cycle oscillations provides such a regime.

Figure 2.13 compares $P(E)$ with $P(n)$ for the limit cycle state corresponding to the Wigner function in Figure 2.5b, at point B on the curve in Figure 2.12. The distribution is roughly Gaussian, with a peak at $E \approx 40$. The two curves closely match in this regime, as expected. Additionally the Gaussian approximation of Section 2.3.7 (shown in blue) provides an accurate description of the limit cycle. At point B, the Fano factor is close to a minimum, with $F \approx 1$, indicating small fluctuations. The average phonon number curves overlap at this point, and the truncated Wigner approximation captures the dynamics of the system with a high accuracy.

The resolved sideband limit is considered in Figure 2.14, where results are compared for the parameters of cases [ii] and [iii]. In the case of strong coupling (Figure 2.14b), the frequency shift is more obvious.
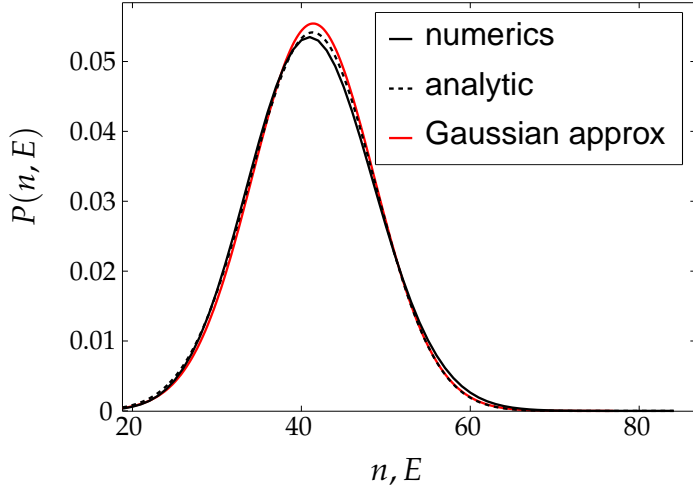
Figure 2.13: Comparison of probability distributions in $P(E)$ (dotted) and $P(n)$ (solid) for $\Delta = -\omega_m$, where the resonator performs limit cycle oscillations. The distribution forms a Gaussian peak at a high energy, resulting in two curve which closely match. Also shown is the Gaussian limit cycle approximation (red) from Section 2.3.7.
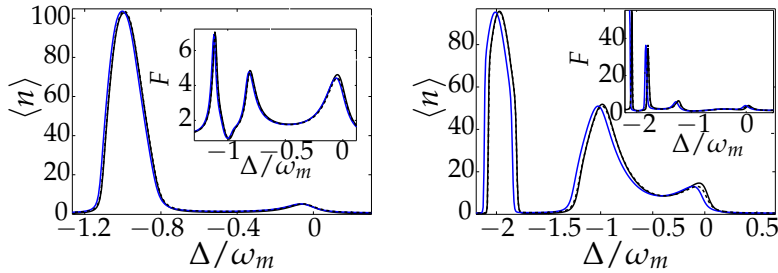
Figure 2.14: A comparison of numerics and analytics in the resolved sideband limit for (a) parameters [ii], where $\lambda = 1$ and (b) parameters [iii], where $\lambda = 2$. Numerics are in black, with analytics in blue. The shifted analytics are shown by dashed lines. The main plots show $\langle n \rangle$ with F in the inset. It is apparent that the larger coupling in (b) produces more noticeable discrepancies, particularly regarding the Δ shift.

2.5 EXPLORING THE BISTABILITY

The truncated Wigner approximation has proved successful in capturing the dynamics of the system, for the case of weak coupling[30]. Prior work using this approximation suggests limitations on the description of quantum tunnelling rates, when

describing switching between stable states of an oscillator[1, 54]. In dropping the third order differentials in Equation 2.27, a description of the system is obtained which only treats the zero point fluctuations exactly[31]. The objective of this section is to determine whether this description is sufficient to capture the dynamics of the system in the bistable state - in particular, to predict the rate of switching between the fixed point and limit cycle. This section deals with a system with parameters given by case [i] of Section 2.4.

In the bistable state the resonator has a finite probability of being found in a fixed point or limit cycle state[41], and fluctuations cause it to switch between the two (this can be seen by large spikes in the Fano factor around bistabilities in Figures 2.4 and 2.8). The probability distribution is described analytically by Equation 2.72 and consists of two peaks, which coincide with minima in the potential, given by the integral

$$U(E) = \int_0^E dE' \frac{\gamma + \gamma_{BA}(E')}{D_{th} + D_{BA}(E')}. \tag{2.86}$$

These minima are separated by a potential barrier. The potential is shown in Figure 2.15, with stationary points a and c (the minima) and b (the maximum) labelled.

The numerical calculation provides a solution to the master equation, giving the density matrix for the system. Analysis up to this point has addressed only the steady state part of the density matrix, which describes the system after transient behaviour has died out. In the shorter time limit however, the density matrix contains time dependent contributions which decay over different timescales. These different timescales encode the dynamical behaviour of the system, including the switching rate in the bistable regime. In Liouville space[60] (see Appendix C) Equation 2.21 can be written

$$|\dot{\rho}\rangle\rangle = \mathcal{L}|\rho\rangle\rangle. \tag{2.87}$$

The matrix $\mathcal{L}$ is constructed to act on the vector $|\rho\rangle\rangle$ to produce the same result as the action of operator $\hat{\mathcal{L}}$ on the density matrix, $|\rho\rangle$. The matrix $\mathcal{L}$ is non-Hermitian and therefore has a separate set of left and right eigenvectors[61], labelled $\langle\langle L_n|$ and $|R_n\rangle\rangle$, respectively. Equation 2.87 has a solution of the form

$$|\rho\rangle\rangle = |\rho_{SS}\rangle\rangle + \sum_{n=1} \langle\langle L_n|\rho(0)e^{\Lambda_n t} \mid R_n\rangle\rangle, \tag{2.88}$$

where Λ_n are the eigenvalues of both eigenvectors $\langle\langle L_n|$ and $|R_n\rangle\rangle$. The general solution is a sum of terms evolving on dif-
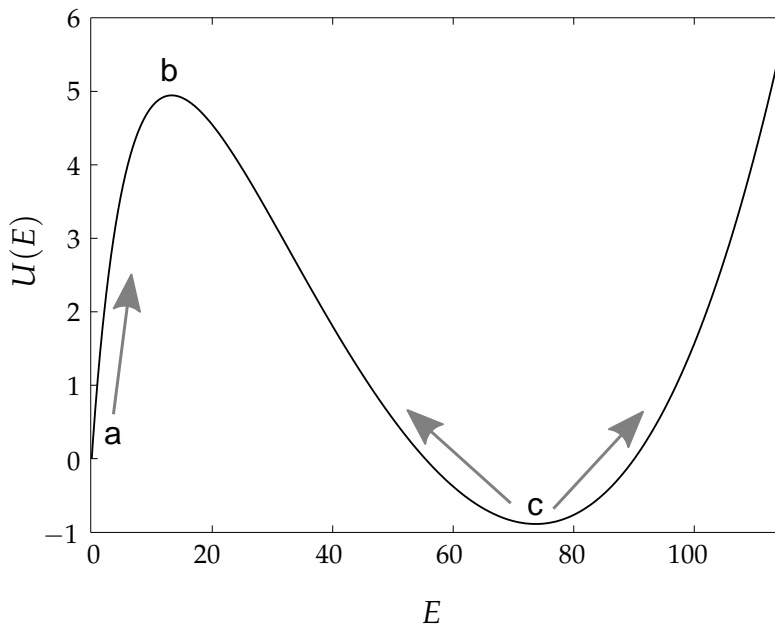
Figure 2.15: The potential barrier for the bistability shown in Figure 2.5c. Points *a* and *c* mark minima in the potential, possible stable states, while *b* marks the maximum of the potential barrier. The arrows show diffusion around the minima which facilitates switching.

ferent timescales[54], which decay at different rates to leave a steady state solution, $|\rho_{SS}\rangle\rangle$, with eigenvalue $\Lambda_0 = 0$.

In the case of a bistable system the longest timescale corresponds to the switching rate. In terms of Figure 2.15, the switching rate describes the rate at which fluctuations cause the system to cross point *b*, the potential barrier, starting at either *a* or *c*. The relaxation rate which describes the rate the system takes to diffuse to the minimum points *a* and *c*, having crossed point *b* will typically be much larger. The switching rate can be identified by the eigenvalue with the smallest magnitude non-zero real part[54].

2.5.1 *Calculating the switching rate in the bistable regime*

The semi-classical approximation of Section 2.3 does not include a description of the switching mechanism, but a classical treatment of the switching problem follows from the calculation of the probability distribution. The problem is modelled analytically, using statistical mechanics, and treated as a first passage time (FPT) problem for a particle moving between two potential

wells[50]. Results are then compared to numerics which solve the eigenvalue equation, as described below.

The analytic calculation employs a classical description of the problem within the truncated Wigner formalism described in Section 2.3. The objective is to calculate the average time for a particle in one potential well to overcome the energy barrier (by energy fluctuations) and reach the other well. This assumes the dynamics are governed by a Fokker-Planck equation. Turning points in the potential are found in order to calculate the FPT for a system initially in either potential well. The switching rate is then given by the sum of their inverses.

The calculation proceeds as follows. The points of interest in a sample potential are shown in Figure 2.15; a is an extremum at $E = 0$, treated as a well, with b the barrier and c the other well. Starting at an energy E_a near point a, the FPT is the average time the system takes takes to pass over the potential barrier of energy E_b at point b. Due to the separation of timescales for switching between and relaxation into the wells, the exact choices of starting/finishing points are not important[50] - so long as $E_{final} \geq E_{max}$ and $E_{start} \approx E_{min}$, where $E_{max(min)}$ is the maximum(minimum) in the potential.

The potential in question is defined for $E > 0$, so that E_a is an extremum, and diffusion from a can only occur in one direction. Point a is therefore identified as a reflecting barrier, since it cannot be crossed. Conversely, point b is an absorbing barrier, so that switching is defined as the system passing through b. To calculate the FPT, first $G(E, t)$ is defined - this is the probability that the system has not overcome the potential barrier at a time t, given that it starts at an energy E in the range $E_a < E < E_b$:

$$\int_{E_a}^{E_b} dE' P(E', t | E, 0) \equiv G(E, t). \tag{2.89}$$

The Fokker-Planck equation given in Equation 2.71 describes the evolution of the probability distribution $P(E', t)$ for $t > 0$, given that the system starts at an energy E at $t = 0$. A calculation of the FPT requires the evolution of $P(E', t)$ for $t < t'$, given a final condition at $t = t'$. This is achieved by writing a backward Fokker-Planck equation for the probability distribution[50]. In contrast to the forward equation, this is defined over a range of times prior to a 'target' state at time t', where the particle overcomes the potential barrier.

In terms of $P(E', t | E, 0)$ - the conditional probability of finding the system with an energy E', where $0 < E' < E_b$ at a

time t, given the system starts at an energy E at $t = 0$ (where $0 < E < E_b$) - the backward Fokker-Planck equation is

$$\partial_t P(E', t|E, 0) = (\gamma + \gamma_{BA}(E)) \, E \partial_E P(E', t|E, 0)$$
$$+ \frac{1}{2} (D_{th} + D_{BA}(E)) \, \partial_E^2 P(E', t|E, 0), \quad (2.90)$$

from which an equation for $G(E, t)$ is deduced:

$$\partial_t G(E, t)) = (\gamma + \gamma_{BA}(E)) \, E \partial_E G(E, t)$$
$$+ \frac{1}{2} (D_{th} + D_{BA}(E)) \, \partial_E^2 G(E, t), \quad (2.91)$$

The average time to reach E_b, given the starting point E_a, is given by

$$\langle T(E_a \to E_b) \rangle = \int_0^\infty \mathrm{d}t \, G(E_a, t), \quad (2.92)$$

which allows an equation of motion for the FPT to be deduced from Equation 2.91, and solved for T. The average time for the system to reach E_b as a function of starting point E_a is then

$$T(E_a \to E_b) = 2 \int_{E_a}^{E_{b2}} dE e^{U(E)} \int_0^E dE' \frac{e^{-U(E')}}{D(E')}, \quad (2.93)$$

where E_{b2} is a point along the potential curve where $E > E_b$, to ensure integration includes the point E_b. The FPT from E_c to $E_b (< E_c)$ where E_b is absorbing, is found in a similar way:

$$T(E_c \to E_b) = 2 \int_{E_{b1}}^{E_c} dE e^{U(E)} \int_E^\infty dE' \frac{e^{-U(E')}}{D(E')}, \quad (2.94)$$

where E_{b1} is a point along the potential curve where $E < E_b$.

The diffusion constant, $D(E) = D_{th} + D_{BA}(E)$, is a function of E, so must also be integrated in the first integral (which has variable limits). The switching rate between potential wells, Γ_{sw}, is then given by

$$\Gamma_{sw} = [T(E_a \to E_b)]^{-1} + [T(E_c \to E_b)]^{-1}. \quad (2.95)$$

2.5.1.1 *Comparing switch rate with lowest eigenvalue*

The eigenvalues Λ_n that describe the relaxation of the system (Equation 2.88) can also be calculated numerically. Figure 2.16 shows the lowest five eigenvalues from the expansion in Equation 2.88. On a logarithmic scale, the lowest eigenvalue Λ_1 is isolated from the others. The presence of an eigenvalue much
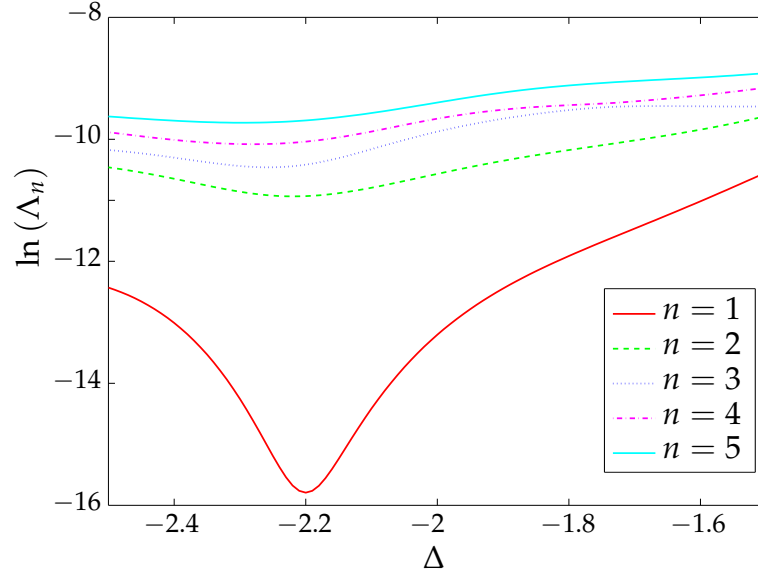
Figure 2.16: Eigenvalues, Λ_n, for $1 \leq n \leq 5$ on a log scale, shown over the bistable range. The lowest value Λ_1 is isolated and much smaller than the others. This is thought to be a characteristic of quantum tunnelling.

closer to zero than the others is often considered a characteristic of quantum tunnelling[54].

The eigenvalue with the smallest non-zero real part, Λ_1, is compared to the switching rate Γ_{sw} in Figure 2.17, for the bistable range. The analytic switching rate differs by up to an order of magnitude from the lowest eigenvalue. The two rates are plotted on a logarithmic scale.

The analytically calculated Γ_{sw} underestimates the switching rate for the range $-2.5 \leq \Delta \leq -1.7$. In the range $\Delta \leq -1.7$, however, it the rapidly increases by several orders of magnitude. In contrast the eigenvalue forms a roughly symmetric well shape over a much smaller range of values. These discrepancies are not unique to this particular calculation, and have been observed as a consistent failing in the truncated Wigner approximation[54].

Figure 2.18a shows the rates $T(a \rightarrow b)$ and $T(c \rightarrow b)$ separately for comparison. It is apparent that the rate from a to b reaches a much higher value than from c to b. As Δ is swept, the potential evolves so that the barrier moves from the vicinity of point a to the vicinity of point c (see Figure 2.18b). As a result $T(a \rightarrow b)$ increases with $|\Delta|$ while $T(c \rightarrow b)$ decreases. However, $T(a \rightarrow b)$ undergoes a rapid increase around $|\Delta| > 2.4$ compared to the increase in $T(c \rightarrow b)$ at $|\Delta| < 2$.
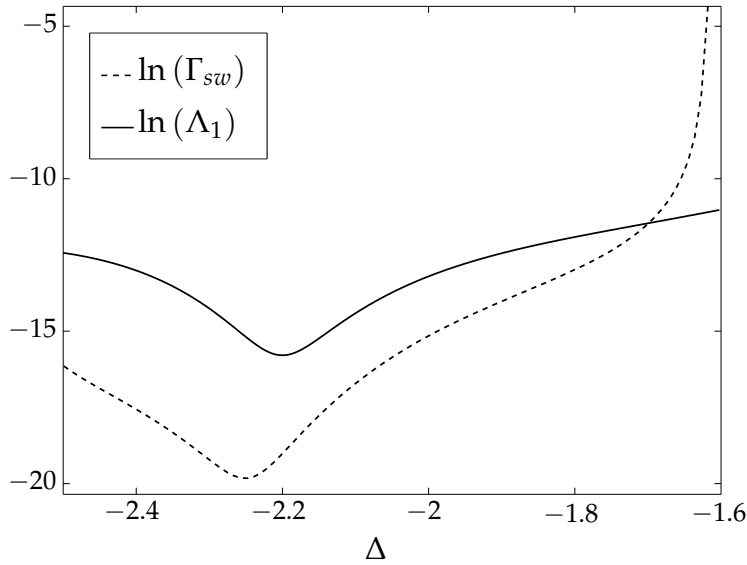
Figure 2.17: Comparison between the switching rates of the system, deduced from a numerical calculation of the eigenvalues (solid) and the classical FPT calculation (dashed). Results are plotted on a log scale as there is a large difference in the results.

(a)   (b)
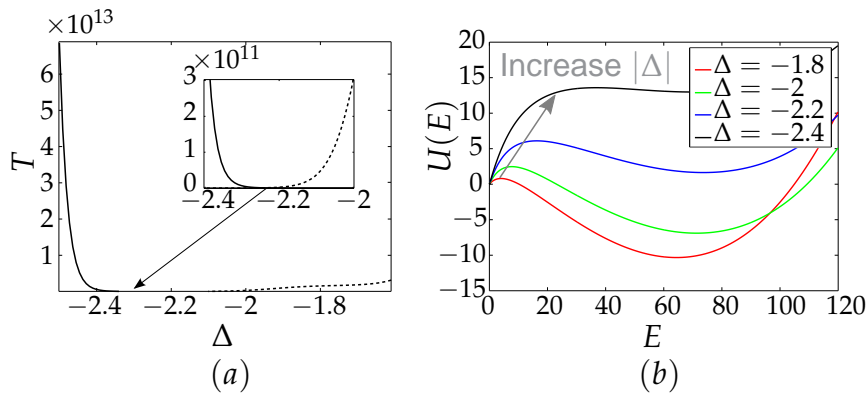
Figure 2.18: The separate switching times calculated, shown in (a) $T(a \rightarrow b)$ (solid) and $T(c \rightarrow b)$ (dashed) show maximum values at either end of the bistable regime which differ by an order of magnitude. Over this range the potential shown in (b) evolves such that the barrier height increases(decreases) relative to the point a(c).

The asymmetry is likely caused by the way the potential is defined. The energy can only take on positive values, and point a lies at the extremum $E = 0$. It is used as a minimum in the calculation, but it does not satisfy $U'(E) = 0$, nor is the system free to diffuse in the opposite direction when placed at $E = E_a$. The system is more confined about a, and therefore more likely

to diffuse up the slope towards b, as shown by the grey arrow in Figure 2.15. At point c, the system is free to diffuse up the slope in either direction. As a result the switching rate in the direction $a \to b$ is much larger than for $c \to b$.

The analytic calculation is clearly unable to describe the dynamics of the bistable state. The FPT calculation models the switching mechanism classically, as fluctuation in the system's energy causing it to overcome the potential barrier[50]. This does not account for the quantum tunnelling suggested by Figure 2.16. In systems where tunnelling occurs, the truncated Wigner approximation is known to fail at capturing the switching rate[1, 54]. The quantum fluctuations, which induce switching on a much faster timescale, are only partly included because the third order derivatives are dropped. This supports the fact that analytics predict a much slower switching rate.

2.5.2 *Relaxation rate calculation*

If the switching rate is given by the lowest non-zero eigenvalue, the next lowest should give the relaxation rate of the system within each potential well. Once a particle has overcome the barrier, this rate describes how long the system takes to relax into the potential well. These rates can be calculated analytically by looking at the dynamics of the average energy (eg by averaging Equation 2.61),

$$\langle \dot{E} \rangle = -[\gamma + \gamma_{BA}(E)]\langle E \rangle. \tag{2.96}$$

Equation 2.96 is expanded in terms of small fluctuations, $\delta E'$ about the limit cycle at E_0:

$$\dot{\delta E} = -[\gamma + \gamma_{BA}(E_0)]\, \delta E + E_0 \frac{d\gamma_{BA}}{dE}\bigg|_{E_0} \delta E, \tag{2.97}$$

where second order fluctuations are discarded.

One can consider the case of a fixed point (where $E_0 = 0$), giving a relaxation rate Γ_r of

$$\Gamma_r(E_0 = 0) = \gamma + \gamma_{BA}(0). \tag{2.98}$$

For a limit cycle the first term in Equation 2.97 will vanish giving the relaxation rate,

$$\Gamma_r(E_0 \neq 0) = E_0 \frac{d\gamma_{BA}}{dE}\big|_{E_0}. \tag{2.99}$$

2.5.2.1 *Comparing relaxation rate with eigenvalues*

Figure 2.19 shows the relaxation rates given by Equations 2.98 and 2.99, plotted alongside the eigenvalues, Λ_n, for $1 \leq n \leq 3$. Far from the bistable regime, in regions $|\Delta| \leq 1.5$ and $|\Delta| \geq 3.25$, the analytic calculation closely matches the lowest non-zero eigenvalue. In particular, the relaxation into the limit cycle state is captured well. Within the bistable regime, however, the calculation fails. Equations 2.98 and 2.99 are deduced by ignoring second order fluctuations in the energy, under the assumption that these are small. This does not hold in the bistable regime, so expressions 2.98 and 2.99 fail here.
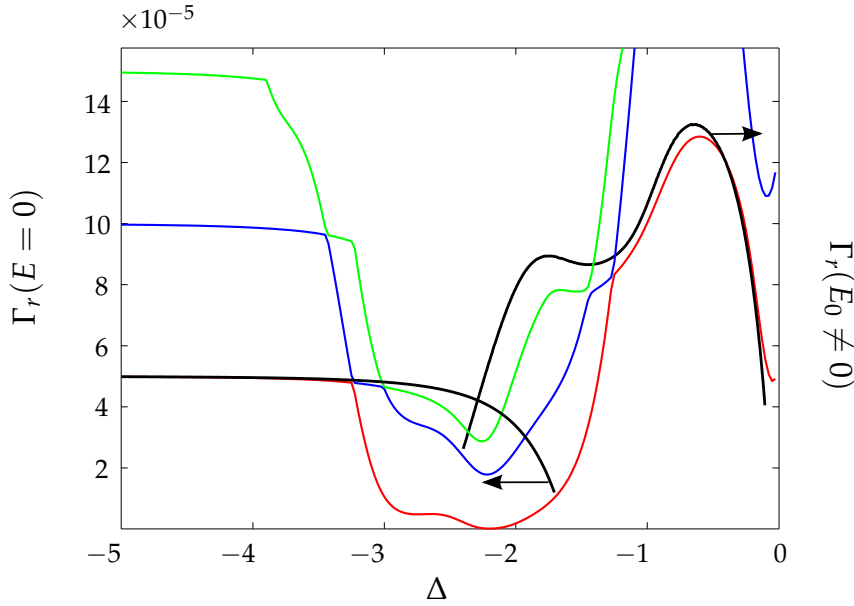
Figure 2.19: Comparison between analytic and numerical calculations of relaxation rates in the system. Thicker black lines show the relaxation rates Γ_r calculated analytically, for the fixed point and limit cycle state. The lowest three non zero eigenvalues Λ_n are also shown, the lowest of which matches Γ_r closely far from the bistable range.

From the analysis of this section, it is apparent that the bistable regime cannot be described by semi-classical analysis. The FPT calculation fails to describe the true quantum nature of the switching mechanism[54], whilst the simple linearized description of fluctuations misses the mark once the system enters the bistable regime. Whilst the truncated Wigner function successfully describes the steady-state properties of the resonator discussed in Section 2.4.4 - even in the bistable state - it falls

short of a more detailed analysis of the switching and relaxation rates.

2.6 CONCLUSION

This chapter has explored the dynamics of a linearly coupled optomechanical system, using the reflective setup. When a drive is applied to the cavity, the resonator transitions between three distinct states as the laser is tuned to different frequencies. These include a state where the system fluctuates about a fixed point, limit cycle oscillations and a bistability. The evolution of the resonator state looks very different depending on whether the system is in the resolved sideband regime. In the strong coupling limit, non-classical states can be generated[10, 43]. In the weak coupling limit, the system can be modelled analytically.

The truncated Wigner function approach provides a way of calculating the dynamics of the system analytically provided the optomechanical coupling is weak (i.e. $\lambda \ll 2\omega_m$). In particular this approach describes the dynamics accurately when the resonator is in a well defined limit cycle and the fluctuations are small, but fails to fully capture the bistable regime where fluctuations are large. An especially serious limitation of the truncated Wigner function is the switching time for a resonator in a bistable state. The quantum value of the switching time has been found to differ by more than an order of magnitude from that obtained using the truncated Wigner approximation.

QUADRATIC COUPLING IN A DISPERSIVE OPTOMECHANICAL SETUP

3.1 INTRODUCTION

Chapter 2 addressed the case of a system in which optical and mechanical modes are coupled via reflection of the light. This produces an interaction which depends linearly on the position of the mechanical oscillator. In this chapter, an alternative approach is considered in the form of a 'dispersive system' which uses the 'membrane-in-the-middle' geometry[25, 16]. A mechanical element placed at the centre of an optical field partially reflects radiation from both sides, so as to couple the optical frequency linearly or quadratically to position, depending on whether the element is placed at a node or anti-node of the optical field[25]. This ability to switch between linear and quadratic interactions, by altering only the membrane position, is an attractive feature of such a system. It allows precision measurements of both the position[62, 63] (in the linear case) and energy[22] (in the quadratic case) of the mechanical element, depending on the coupling chosen[17].

In Chapter 2 the non-linear dynamics of the reflective system were analysed using a numerical approach, as well as a semi-classical approximation. Analytics were generated using a truncated Wigner approximation. In this chapter a similar toolbox of mathematical techniques is applied to the quadratic system. The aim is to calculate a probability distribution for the state of the mechanical resonator, allowing its behaviour to be investigated under different conditions.

Using a Wigner transformation, Langevin type equations are found to describe the optical and mechanical modes. Solutions to these equations lead to an expression for the damping due to back action, which can be used to determine the presence of stable limit cycles in the resonator. In addition, the diffusion in the system is calculated. Together with the damping this allows a probability distribution of states of the resonator to be obtained. The analytic results are compared with numerical calculations and good agreement is found under certain circumstances. The regime of strong coupling is also investigated, and a number of

signatures of non-classical behaviour are found to occur in the mechanical resonator.

This chapter is organised as follows. In Section 3.2 the 'membrane in the middle' approach is introduced, detailing its formulation in terms of a Hamiltonian and master equation. Section 3.3 outlines a semi-classical analysis of the system via a similar set of approximations to those used in Chapter 2. Numerical calculations are described and analysed in Section 3.4. The numerics are compared to analytics in Section 3.5. Section 3.6 draws conclusions.

3.2   MEMBRANE IN THE MIDDLE SYSTEM

The system under consideration consists of two fixed mirrors with a membrane placed in between, as shown schematically in Figure 3.1a. The membrane divides the cavity into two chambers. Consider a pair of modes (one in each chamber) with almost identical frequencies, ω_L and ω_R. The membrane supports mechanical modes as it vibrates. The vibrations alter the lengths of each chamber, coupling the membrane displacement to the optical frequencies. A perfectly reflecting membrane displaced by an amount $q(t)$ would shift the two mode frequencies as follows,

$$\omega_L(q) \approx \omega_0 - \lambda q(t), \tag{3.1}$$

$$\omega_R(q) \approx \omega_0 + \lambda q(t), \tag{3.2}$$

where ω_0 is the cavity frequency in both chambers when the membrane is fixed at the centre and λ is the coupling between the optical and mechanical modes. This relates to the length of each chamber, L, by $\lambda = \omega_0/L$. In fact the membrane is partially transmitting, coupling the optical modes together into two new harmonic modes with frequencies ω_1 and ω_2 respectively (shown by the blue lines in Figure 3.1b). The strength of the coupling is parametrised by g, which relates to the rate at which photons tunnel through the membrane. This coupling creates an anti crossing in their dispersion diagram[16] as shown in Figure 3.1b. The dotted lines represent mode frequencies for a perfectly reflecting membrane. When radiation is allowed to pass through the membrane, the two modes become coupled, illustrated by the two solid blue curves. The energy gap $2g$ (which will be addressed in a later section) arises due to the coupling.
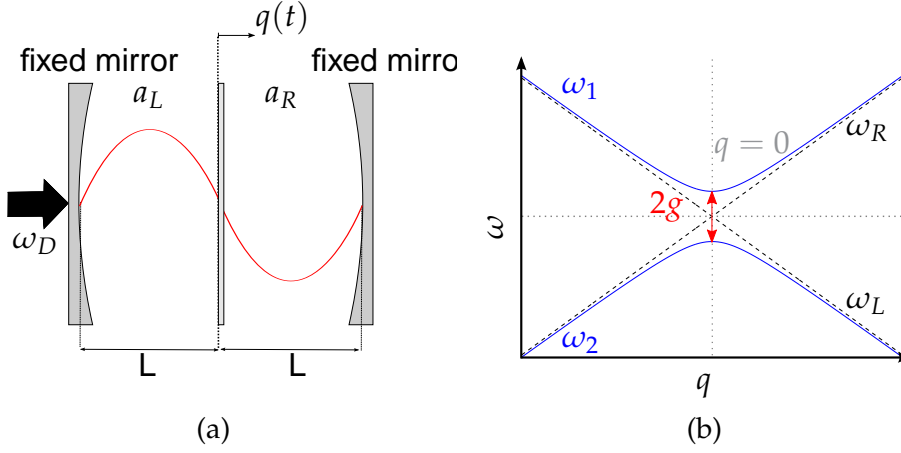
Figure 3.1: (a) Schematic of the system: two fixed mirrors form a cavity divided into two chambers of length L, by a membrane displaced by an amount $q(t)$ from the cavity centre. Each chamber supports an optical mode, a_L (left) or a_R (right). (b) Dispersion diagram for the optical modes showing two uncoupled modes when the membrane is perfectly reflecting (dashed lines) with frequencies $\omega_{L,R}$; when radiation is allowed through the membrane ($g \neq 0$) the modes couple together to create the solid blue dispersion curves with frequencies $\omega_{1,2}$. Close to $q = 0$ (labelled) the dispersion of these modes is approximately quadratic.

3.2.1 *Experimental considerations*

The 'membrane in the middle' geometry offers advantages in the fabrication of high Q-factor mechanical elements[19]. For the reflective approach this is not as easily achievable, as it can be difficult to manufacture mirrors with both a high Q-factor and high reflectivity[18]. Whilst various solutions are available, the dispersive approach eliminates this problem, as radiation is allowed to pass through the membrane[22]. High mechanical quality factors are possible when high-finesse SiN membranes are used, due to their low intrinsic losses[19, 18]. A high finesse is possible for the cavity when highly reflective mirrors are combined with low absorption in the membrane. This has been achieved via use of stoichiometric SiN in a thin membrane - typically $\sim$ 50 nm in thickness, compared to the cavity length of the order 10 cm. Typically a finesse of up to 50,000 is achievable[22, 25].

An example of a dispersive optomechanical system is presented in Figure 3.2[22, 25, 16, 64]. The SiN membrane is sup-

ported by a frame and positioned between two mirrors, M1 and M2, mounted on a cavity spacer, inside a vacuum chamber. An Nd:YAG laser provides the drive[1][65]. The beam is passed through an optical isolator (OFR) and into the cavity, via two steering mirrors, SM1 and SM2. The output from the cavity is fed through a photodiode (PD) which measures the optical power transmitted and feeds it into a digital storage oscilloscope. This way one can measure the optical frequency of modes in the cavity, from which the mechanical position can be deduced.
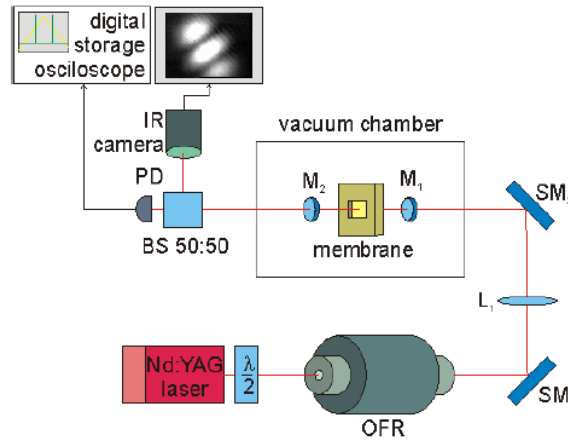
Figure 3.2: Schematic of a typical membrane in the middle experimental setup[64]. See text of Subsection 3.2.1 for further details.

3.2.2 *The Hamiltonian and master equation*

In this chapter, quadratic optomechanical coupling is explored. This can arise for the membrane in the middle geometry, illustrated in Figure 3.1a. The Hamiltonian can be derived by considering the modes of the whole cavity[18, 19]. Here the quadratic Hamiltonian is motivated using a simple model, which starts from a description in terms of the modes of the left and right sub-cavities (see Figure 3.1a) and allows for partial transmis-

---

1 neodymium-doped yttrium aluminium garnet is a crystal, widely used as a lasing medium for solid-state lasers. The neodymium ions provide a four-level system.

sion. In terms of these two modes (shown as dashed lines in Figure 3.1b) the Hamiltonian takes the form

$$
\begin{aligned}
H \;=\; & \omega_L(q)a_L^\dagger a_L + \omega_R(q)a_R^\dagger a_R + g(a_L^\dagger a_R + a_R^\dagger a_L) \\
& + \tfrac{1}{2}\omega_m(p^2 + q^2) + \Omega(a_L e^{i\omega_d t} + a_L^\dagger e^{-i\omega_d t}),
\end{aligned}
\tag{3.3}
$$

where $a_L(a_R)$ is the annihilation operator for the left(right) mode and the left mode is assumed to be driven with strength Ω, at frequency ω_d. The membrane's displacement is taken as q, with momentum p, and frequency ω_m. The optical frequencies are functions of q, given by Equations 3.1 and 3.2. Note that in terms of resonator raising(lowering) operators $b^\dagger(b)$, $q = (b + b^\dagger)/\sqrt{2}$ and $p = (b - b^\dagger)/(\sqrt{2}i)$.

Since the cavity modes couple together, it can be more intuitive to write the Hamiltonian in terms of the upper and lower dispersion bands (solid blue lines in Figure 3.1b), represented by annihilation operators a_1 and a_2. The transformation is linear and of the form (for details, see Appendix D):

$$
a_1 = ua_L + va_R, \tag{3.4}
$$

$$
a_2 = xa_L + ya_R, \tag{3.5}
$$

with coefficients

$$
u \;=\; \frac{g}{\sqrt{g^2 + (\omega_1 - \omega_L)^2}} \tag{3.6}
$$

$$
v \;=\; \frac{\omega_1 - \omega_L}{\sqrt{g^2 + (\omega_1 - \omega_L)^2}} \tag{3.7}
$$

$$
x \;=\; \frac{\omega_2 - \omega_R}{\sqrt{g^2 + (\omega_2 - \omega_R)^2}} \tag{3.8}
$$

$$
y \;=\; \frac{g}{\sqrt{g^2 + (\omega_2 - \omega_R)^2}}, \tag{3.9}
$$

where ω_1 and ω_2 are given by

$$
\omega_1 \;=\; \omega_0 + \sqrt{g^2 + (\lambda q)^2} \tag{3.10}
$$

$$
\omega_2 \;=\; \omega_0 - \sqrt{g^2 + (\lambda q)^2}. \tag{3.11}
$$

This then allows the Hamiltonian to be written in the following form:

$$
\begin{aligned}
H \;=\; & \omega_1 a_1^\dagger a_1 + \omega_2 a_2^\dagger a_2 + \tfrac{1}{2}\omega_m(p^2 + q^2) \\
& + \Omega[(Xa_1 - Ya_2)e^{i\omega_d t} + (Xa_1^\dagger - Ya_2^\dagger)e^{-i\omega_d t}],
\end{aligned}
\tag{3.12}
$$

where X and Y are given by

$$X = \frac{g\sqrt{g^2 + (\omega_1 - \omega_L)^2}}{g^2 - (\omega_1 - \omega_L)(\omega_2 - \omega_R)}, \tag{3.13}$$

$$Y = \frac{(\omega_1 - \omega_L)\sqrt{g^2 + (\omega_2 - \omega_R)^2}}{g^2 - (\omega_1 - \omega_L)(\omega_2 - \omega_R)}. \tag{3.14}$$

The coupled frequencies $\omega_{1,2}$ have a dependence on q which is approximately quadratic when $g \gg \lambda q$

$$\omega_1 \approx \omega_0 + \left[g + \frac{\lambda^2}{2g}q^2 \right], \tag{3.15}$$

$$\omega_2 \approx \omega_0 - \left[g + \frac{\lambda^2}{2g}q^2 \right]. \tag{3.16}$$

Thus by probing the dynamics around $q \approx 0$, the case of quadratic optomechanical coupling is explored.

The minimum frequency gap is $2g$, as shown in Figure 3.1b. For $g \gg \omega_m$, the upper and lower modes are separated by a large enough frequency that there is little chance of transitions between them. This allows a single mode to be considered by selecting a drive frequency close to its resonance. This chapter focuses on a single optical mode with frequency ω_1, and the corresponding annihilation operator is labelled simply a. The effects of quadratic coupling to the mechanical resonator can then be analysed.

In Chapter 2, Equations 2.11 to 2.15 detail a unitary transformation on the Hamiltonian. An identical transformation gives the effective Hamiltonian for the quadratically coupled system, in the rotating frame of the drive frequency:

$$H_{eff} = \Delta a^\dagger a + Gq^2 a^\dagger a + \frac{1}{2}\omega_m(p^2 + q^2) + \epsilon(a + a^\dagger), \tag{3.17}$$

where $\Delta = \omega_0 + g - \omega_d$, $\epsilon = \Omega X$, $G = \lambda^2/(2g)$. Note that the implicit q dependence in the drive term that arises through X is neglected in the following. The master equation is written in terms of $\tilde{\rho}$, the density operator in this rotating frame:

$$\dot{\tilde{\rho}} = -i\left[H_{eff}, \tilde{\rho}\right] + \hat{\mathcal{L}}_a\tilde{\rho} + \hat{\mathcal{L}}_b\tilde{\rho}. \tag{3.18}$$

The same model as that introduced in Chapter 2 is applied to describe dissipation in the cavity and resonator in terms of two separate environments of harmonic oscillators which couple to each set of modes separately. This results in operators $\hat{\mathcal{L}}_a$ and

$\hat{\mathcal{L}}_b$ identical to the linear case (where again it is assumed that $\overline{n}_a = 0$):

$$\hat{\mathcal{L}}_a\tilde{\rho} = -\frac{\kappa}{2}\left(a^\dagger a\tilde{\rho} + \tilde{\rho}a^\dagger a - 2a^\dagger\tilde{\rho}a\right), \qquad (3.19)$$

$$\hat{\mathcal{L}}_b\rho = -\frac{\gamma}{2}(\overline{n}+1)\left(b^\dagger b\rho + \rho b^\dagger b - 2b^\dagger\rho b\right)$$
$$-\frac{\gamma}{2}\overline{n}\left(bb^\dagger\rho + \rho bb^\dagger - 2b\rho b^\dagger\right). \qquad (3.20)$$

The analysis that follows employs a very similar combination of analytical and numerical methods to those used for the linearly coupled system. The next section details an analytic approach via a semi-classical approximation, before further sections discuss numerical results.

3.3   SEMI-CLASSICAL APPROXIMATION

3.3.0.1   *Wigner transformation*

The semi-classical approach follows an analogous procedure to Chapter 2. Once again, the truncated Wigner approximation is employed to obtain a Fokker-Planck equation describing the evolution of the quasi-probability distribution for the coupled system. Previously this proved effective in describing the linearly coupled system, with the only notable discrepancies being a shift in Δ[30] and a failure to predict quantum tunnelling rates[54].

The transformation is detailed in Appendix A. Here the results are presented in a similar framework to Chapter 2. The truncated equation is

$$\frac{\partial W}{\partial t} = \frac{\partial}{\partial\beta^*}\left(-i\omega_m\beta^* + \frac{\gamma}{2}\beta^* - 2iG(\beta^* + \beta)(\alpha^*\alpha - \frac{1}{2})\right)W$$
$$+\frac{\partial}{\partial\beta}\left(i\omega_m\beta + \frac{\gamma}{2}\beta + 2iG(\beta^* + \beta)(\alpha^*\alpha - \frac{1}{2})\right)W$$
$$+\frac{\partial}{\partial\alpha^*}\left(-i\Delta\alpha^* + \frac{\kappa}{2}\alpha^* - iG\alpha^*(\beta^* + \beta)^2 - i\epsilon^*\right)W$$
$$+\frac{\partial}{\partial\alpha}\left(i\Delta\alpha + \frac{\kappa}{2}\alpha + iG\alpha(\beta^* + \beta)^2 + i\epsilon\right)W$$
$$+\frac{\gamma}{2}(2\overline{n}+1)\frac{\partial^2 W}{\partial\beta\partial\beta^*} + \frac{\kappa}{2}\frac{\partial^2 W}{\partial\alpha\partial\alpha^*}, \qquad (3.21)$$

where once again the phase space variables α and β replace the quantum operators a and b, and the shorthand $W = W(\alpha, \beta)$ is

used for the Wigner function. Langevin equations for α, α^*, β and β^* follow from Equation 3.21[1]:

$$\dot{\alpha} = -i\Delta\alpha - iG\alpha(\beta + \beta^*)^2 - \frac{\kappa}{2}\alpha - i\epsilon + \eta_\alpha, \qquad (3.22)$$

$$\dot{\alpha^*} = i\Delta\alpha^* + iG\alpha^*(\beta + \beta^*)^2 - \frac{\kappa}{2}\alpha^* + i\epsilon + \eta_{\alpha^*}, \qquad (3.23)$$

$$\dot{\beta} = -i\omega_m\beta - 2iG(\beta + \beta^*)\left(\alpha^*\alpha - \frac{1}{2}\right) - \frac{\gamma}{2}\beta + \eta_\beta \qquad (3.24)$$

$$\dot{\beta^*} = i\omega_m\beta^* + 2iG(\beta + \beta^*)\left(\alpha^*\alpha - \frac{1}{2}\right) - \frac{\gamma}{2}\beta^* + \eta_{\beta^*}, \qquad (3.25)$$

where, as previously, η_α and η_β are Gaussian white noise variables, describing fluctuations in variables α and β.

3.3.1 *Analysis of the Langevin equations*

As in Chapter 2, an analytic calculation considers the regime where optical timescales are much faster than mechanical ones. In particular, it is assumed that $\kappa \gg \gamma, G$, so the rate at which the energy of the mechanical resonator changes is much slower than that of the optical mode. This allows $\beta = Be^{-i(\omega_m't + \phi)}$ to be substituted into Equation 3.22, where ϕ is a phase variable and $\omega_m' = \omega_m + \delta\omega$. The shifted mechanical frequency, ω_m', will be determined self-consistently. Since the coupling is quadratic with position, oscillations occur around the centre of the cavity, so that $\beta_c = 0$. With the quantities B, $\delta\omega$ and ϕ treated as constants (See Chapter 2, Section 2.3.1 for details), Equation 3.22 is written

$$\dot{\alpha} = -\left[i\Delta' + \frac{\kappa}{2} + 2iB^2G\cos\left(2(\omega_m't + \phi)\right)\right]\alpha - i\epsilon$$
$$+\eta_\alpha, \qquad (3.26)$$

where $\Delta' = \Delta + 2B^2G$. The calculation proceeds almost identically to Chapter 2. A substitution, $\tilde{\alpha} = \alpha e^{iz\sin\left(2(\omega_m't + \phi)\right)}$, is made, where $z = B^2G/\omega_m$:

$$\dot{\tilde{\alpha}} = -\left[i\Delta' + \frac{\kappa}{2}\right]\tilde{\alpha} - \frac{i\epsilon}{2\pi}e^{iz\sin\left(2(\omega_m't + \phi)\right)} + \tilde{\eta}_\alpha. \qquad (3.27)$$

The equation is Fourier transformed, separated into average and fluctuating parts, and the Jacobi-Anger expansion[55] applied to express $\tilde{\alpha}(\omega)$ in terms of a Bessel series:

$$\tilde{\alpha}(\omega) = \langle\tilde{\alpha}(\omega)\rangle + \delta\tilde{\alpha}(\omega), \qquad (3.28)$$

where

$$\langle \tilde{\alpha}(\omega) \rangle = \frac{-i\epsilon \sum_n \delta(\omega - 2n\omega'_m) J_n(z) e^{i2n\phi}}{i(\omega + \Delta') + \frac{\kappa}{2}}, \qquad (3.29)$$

$$\delta\tilde{\alpha}(\omega) = \frac{\tilde{\eta}_\alpha(\omega)}{i(\omega + \Delta') + \frac{\kappa}{2}}. \qquad (3.30)$$

Similar analysis, with the transformation $\tilde{\alpha}^* = \alpha^* e^{-iz \sin(2(\omega'_m t + \phi))}$, yields the expression $\tilde{\alpha} = \langle \tilde{\alpha}^* \rangle + \delta\tilde{\alpha}^*$, where

$$\langle \tilde{\alpha}^*(\omega) \rangle = \frac{i\epsilon \sum_n \delta(\omega + 2n\omega'_m) J_n(z) e^{-i2n\phi}}{i(\omega - \Delta') + \frac{\kappa}{2}}, \qquad (3.31)$$

$$\delta\tilde{\alpha}^*(\omega) = \frac{\tilde{\eta}_{\alpha^*}(\omega)}{i(\omega - \Delta') + \frac{\kappa}{2}}, \qquad (3.32)$$

3.3.2 *Damping due to back action*

Turning to Equation 3.24, analysis of the damping requires a calculation of the coupling term arising from the average dynamics of the cavity, this is given by

$$\langle \alpha^* \rangle \langle \alpha \rangle (\omega) = \epsilon^2 \frac{\sum_{n,n'} J_n(z) J_{n'}(z) e^{i2(n-n')\phi} \delta(f_{n,n'}(\omega))}{h_n^*(h_n + i\omega)}, \quad (3.33)$$

where the following have been defined:

$$h_n = \frac{\kappa}{2} + i\left(2n\omega'_m + \Delta'\right) \qquad (3.34)$$

$$f_{n,n'}(\omega) = \omega + 2\omega_m(n - n'). \qquad (3.35)$$

Equation 3.24 is then

$$\dot{\beta} = -\left(i\omega'_m + \frac{\gamma}{2}\right)\beta - 2iG\langle \alpha^* \rangle \langle \alpha \rangle \left(1 + e^{2i(\omega'_m t + \phi)}\right)\beta$$

$$-2iG\left(\langle \alpha^* \rangle \delta\alpha + \langle \alpha \rangle \delta\alpha^*\right)\left(1 + e^{2i(\omega'_m t + \phi)}\right)\beta + \eta_\beta, (3.36)$$

where the first two terms describe average dynamics and the final two describe fluctuations. Focusing on the average dynamics allows the damping due to back action and the frequency shift to be deduced. With the ansatz of Section 3.3.1, Equation 3.36 is written in terms of amplitude B,

$$\dot{B} = -\left(\frac{\gamma}{2} + 2iG\langle \alpha^* \rangle \langle \alpha \rangle \left(1 + e^{2i(\omega'_m t + \phi)}\right)\right)B. \quad (3.37)$$

To proceed, a rotating wave approximation is applied, as described in Chapter 2. This isolates contributions to the sum over

n' that produce terms oscillating at ω'_m, whilst other terms rotate rapidly and can be discarded[56]. The resulting equation is

$$\dot{B} = -\left(\frac{\gamma}{2} + \Gamma\right)B, \tag{3.38}$$

where

$$\Gamma = 2iG\epsilon^2 \sum_n \left(\frac{J_n^2(z)}{|h_n|^2} + \frac{J_n(z)J_{n+1}(z)}{h_{n+1}h_n^*}\right), \tag{3.39}$$

and

$$h_n = \frac{\kappa}{2} + i(2n\omega'_m + \Delta'). \tag{3.40}$$

Note that the ϕ dependence is lost and so the resulting damping expression will only depend on B and ω'_m. The damping and frequency shift are identified as the real and imaginary components of the coupled term, respectively:

$$\gamma_{BA}(z) = -4G\kappa\omega'_m\epsilon^2 \sum_n \frac{J_n(z)J_{n+1}(z)}{|\,h_n\,|^2|\,h_{n+1}\,|^2}, \tag{3.41}$$

$$\delta\omega(z) = 2G\epsilon^2 \sum_n \left[\frac{J_n(z)^2}{|\,h_n\,|^2} - \frac{J_n(z)J_{n+1}(z)\chi_n}{|\,h_n\,|^2|\,h_{n+1}\,|^2}\right], \tag{3.42}$$

where

$$\chi_n = \kappa^2/4 + \left(2(n+1)\omega'_m + \Delta'\right)\left(2n\omega'_m + \Delta'\right). \tag{3.43}$$

In Chapter 2 the correction $\omega' = \omega_m + \delta\omega$ results in negligible errors in γ_{BA}, so it was ignored and ω_m used throughout. For the quadratic case, the errors are slightly higher (around 10^{-2} for the parameters considered) and the correction is added in. The shift $\delta\omega(z)$ is calculated using the un-shifted frequency ω_m, before using the shifted frequency ω'_m to calculate $\gamma_{BA}(z)$ and $\delta\omega(z)$.

Figure 3.3 shows the damping due to back-action on a colour plot for different energies as Δ is varied. The white contour shows solutions to the energy balance condition for limit cycles:

$$\gamma + \gamma_{BA}(E_0) = 0, \tag{3.44}$$

where $\gamma_{BA}(E_0)$ is the damping due to back action as a function of energy, at point $E_0 = B_0^2$. For each value of Δ either two solutions occur, or there is no limit cycle. The stability condition for a limit cycle requires $\gamma'_{BA}(E_0) > 0$, which results in stable limit cycles at the higher energy end of the contour.
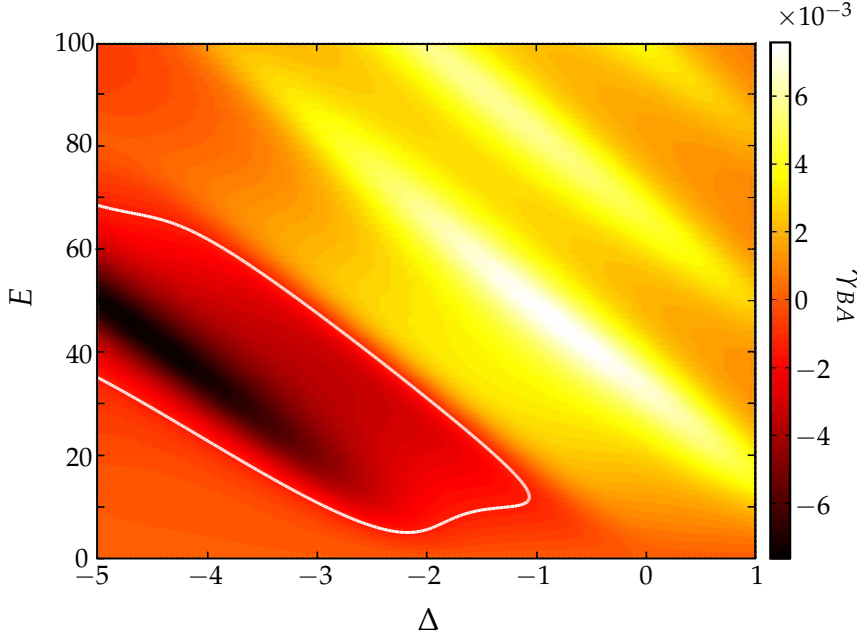
Figure 3.3: The damping due to back action, with respect to energy E and detuning Δ. White regions signify heavy damping whilst darker regions show strong driving. The white contour marks solutions to the energy balance condition, for limit cycles. For each value of Δ, there is either no limit cycle or two solutions occur at different energies. The higher energy solutions are found to be stable. Parameters used are $G = 0.03$, $\epsilon = 0.4$, $\gamma = 1.4 \times 10^{-3}$ and $\kappa = 1$.

It is worth noting the behaviour of γ_{BA} at $E = 0$. Taking $z \ll 1$, the asymptotic Bessel function behaviour is considered:

$$J_n(z) \approx \frac{1}{n!} \left(\frac{z}{2}\right)^n. \tag{3.45}$$

The damping is then approximated by the leading terms in the sum, $n = 0$ and $n = -1$,

$$\gamma_{BA} \approx \frac{16 G \kappa \omega_m^2 \epsilon^2 \Delta' z}{[\frac{\kappa^2}{4} + \Delta'][\frac{\kappa^2}{4} + (2\omega_m + \Delta')^2][\frac{\kappa^2}{4} + (2\omega_m - \Delta')^2]}. \tag{3.46}$$

The back action damping is thus proportional to E as $E \to 0$, so that $\gamma_{BA}(0) = 0$. This results in a total damping which is always positive in the low energy limit, so that the stability condition on the fixed point at the origin ($E = 0$), $\gamma + \gamma_{BA}(0) > 0$, is always satisfied. The fixed point is therefore always a stable solution for the case of quadratic coupling.

3.3.3 *Diffusion due to back action*

With the intention of including fluctuations in the analysis, Equation 3.24 is written in terms of energy:

$$\dot{E} \;=\; -\gamma_T E + \eta_T \sqrt{E}, \tag{3.47}$$

where $\gamma_T = \gamma + \gamma_{BA}(E)$, and $\gamma_{BA}(E)$ is given by Equation 3.41, noting that $z = GE/\omega_m$. The fluctuating terms are given by

$$\eta_T(\omega, E) \;=\; \left(\eta_\beta e^{i\omega_m t + \phi} + \eta_\beta^* e^{-(i\omega_m t + \phi)} + \eta_{BA}(\omega, E)\right), \tag{3.48}$$

where

$$\eta_{BA}(\omega, E) \;=\; 2\sqrt{E}\left(\eta_{eff} + \eta_{eff}^*\right)\sin\left(2\omega_m' t + 2\phi\right), \tag{3.49}$$

$$\eta_{eff} \;=\; 2G\langle\alpha^*\rangle\delta\alpha. \tag{3.50}$$

Note that, once again second order fluctuations have been approximated by their averages, and do not contribute towards the diffusion. Using the same approach as Chapter 2, Section 2.3.4, the diffusion is described by the expression

$$D_{BA}(z) \;=\; \lim_{\omega'\to 0}\frac{\omega'}{2\pi}\int_0^{2\pi/\omega'} dt \int_{-\infty}^{\infty} d\omega e^{i(\omega t + \omega' t')}\zeta(\omega, \omega') \tag{3.51}$$

where

$$\zeta(\omega, \omega') \;=\; \langle\eta_{BA}(\omega)\eta_{BA}(\omega')\rangle. \tag{3.52}$$

Following a similar series of steps to the linear case, the diffusion constant due to back action is given by

$$D_{BA}(z) \;=\; 2G\epsilon^2\omega_m^2\kappa z \sum_n \left[\frac{J_n^2(z)}{|h_n|^2}\left(\frac{1}{|h_{n+1}|^2} + \frac{1}{|h_{n-1}|^2}\right)\right.$$
$$\left. - \frac{J_n(z)J_{n+2}(z)}{|h_{n+1}|^2}\left(\frac{1}{h_n^* h_{n+2}} + \frac{1}{h_n h_{n+2}^*}\right)\right]. \tag{3.53}$$

In the small energy limit, $z \ll 1$, one can apply a similar approximation to that applied to the damping in Section 3.3.2. The resulting expression for D_{BA} then contains a contribution from the $n = 0$ term only:

$$D_{BA} \approx \frac{2G\kappa\omega_m\epsilon^2\left(\frac{\kappa^2}{4} + \Delta'^2 + 4\omega_m^2\right)z}{\left[\frac{\kappa^2}{4} + \Delta'^2\right]\left[\frac{\kappa^2}{4} + (2\omega_m + \Delta')^2\right]\left[\frac{\kappa^2}{4} + (2\omega_m - \Delta')^2\right]} \tag{3.54}$$

It is interesting to note that both the diffusion and damping due to back action are approximately linear at small energies, in contrast to the linearly coupled system, where both tend towards constants as $E \to 0$. This will be important when addressing the cooling regime.

3.3.4 *Probability distribution for the resonator*

Equation 3.47 takes the form of a Langevin equation in E, which is converted into a Fokker-Planck equation for the probability distribution for the energy, $P(E, t)$. This is achieved via an identical analysis to that applied in the linear case (see Section 2.3.5, Chapter 2). Solving for the steady state, $\dot{P}(E, t) = 0$, gives a probability distribution that takes the same form:

$$P(E) \propto e^{-U(E)}, \tag{3.55}$$

with

$$U(E) \;=\; \int_0^E dE' \frac{\gamma + \gamma_{BA}(E')}{D_{th} + D_{BA}(E')}, \tag{3.56}$$

where $\gamma_{BA}(E)$ and $D_{BA}(E)$ are given by Equations 3.41 and 3.53, respectively. Semi-classical expressions for observables in the resonator dynamics then follow.

3.3.5 *Cooling Regime*

When the system is in the red-detuned regime, energy is extracted from the resonator, and cooling is possible. This allows a series of approximations to further simplify the expressions of this section. In contrast to the linear coupling case, the back action contributions to both damping and diffusion are proportional to z, when $z \ll 1$. This results in a probability distribution that is slightly more complicated than that obtained in Chapter 2, Section 2.3.6. Quadratic coupling does not allow a thermal distribution to be reached at low resonator energies. Analysis of the distribution in the case of cooling therefore requires additional approximations; this section looks at the resolved sideband limit.

Sideband cooling in the resolved sideband limit puts the system in the regime of low resonator energies. The anti-Stokes process dominates and the system can be cooled close to its ground state, $z \ll 1$[9].

In the resolved sideband limit $\kappa \ll \omega_m$ and energy exchange is concentrated strongly at the resonance at $\Delta = 2\omega_m$. Since the cooling regime takes the system towards lower energies, one can further assume that $z \ll 1$, provided the initial temperature

is not too high. With these assumptions, Equations 3.46 and 3.54 gives

$$\gamma_{BA}(z) \approx \frac{2G\epsilon^2 z}{\kappa \omega_m} \tag{3.57}$$

$$D_{BA}(z) \approx \frac{G\epsilon^2 z}{\kappa \omega_m} \tag{3.58}$$

A simple expression for the probability distribution can be found when thermal fluctuations dominate, $D_{BA}/D_{th} \ll 1$. Equation 3.55 then approximates to

$$P(E) \propto e^{-\frac{\epsilon^2 G^2 E^2}{\kappa \gamma \omega_m^2 \bar{n}}} e^{-\frac{E}{\bar{n}}}, \tag{3.59}$$

In the limit $\epsilon^2 G^2 / \kappa \gamma \omega_m^2 \ll \bar{n}$ the distribution behaves as a decaying exponential. This limit is depicted in Figure 3.4, which shows the damping and probability distribution. Here the intrinsic damping dominates so the approximated probability distribution is accurate, whilst the approximation in Equation 3.57 begins to diverge for $E > 1$.
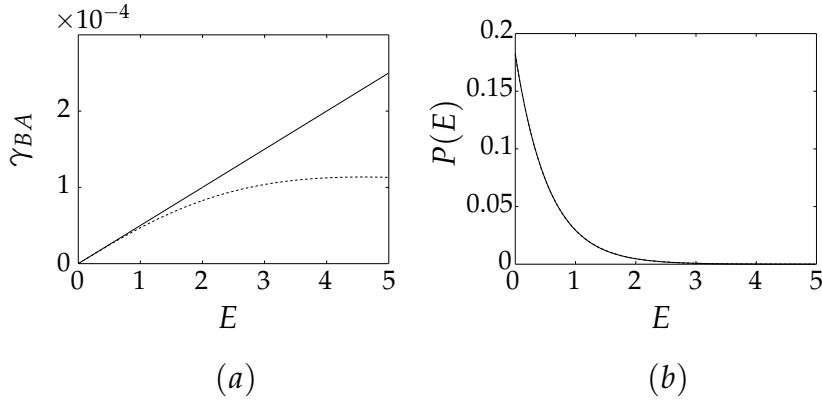
Figure 3.4: Analytics for $\omega_m = 5$, $\gamma = 0.1$, $\epsilon = 0.4$, $\bar{n} = 5$, $G = 0.03$. Solid lines represent the small energy approximation, whilst dashed lines give the semi-classical approximation. Figures show (a) damping due to back action and (b) probability distribution.

It should be noted that the results presented in this limit match those in recent work by Nunnenkamp et al.[45]. In contrast to the analysis of this section, Nunnenkamp et al. derive their expression for the probability distribution by deriving an effective classical master equation directly from the full quantum master equation.

3.4 NUMERICAL ANALYSIS

In this section the numerical solution to the master equation is explored, focusing especially on the blue-detuned regime where limit cycles occur. The analysis addresses the cases of strong and weak optomechanical coupling.

The coupling determines the strength of the non-linearity, which affects the type of behaviour seen in the resonator[66]. Analysis deals with the weak and strong coupling limits separately. At weak coupling, $G \ll \kappa$, the analytic calculations are expected to capture the behaviour of the resonator. In the strong coupling regime, $G \gg \kappa$, the fundamental assumption of the semi-classical approximation is expected to break down, since the third order differentials are proportional to G. This regime can therefore only be explored numerically. Since the two Hamiltonians differ only by a coupling term, the quadratic system is expected to show similar features to the linear system as $G \to 0$. Plots are presented which examine the average behaviour of the phonon number, $\langle n \rangle$, Fano factor, F and Wigner function of the resonator.

3.4.1 *Weak coupling*

For the case of weak coupling, the parameters of Table 3.1 are investigated.

Table 3.1: Table of parameters.

Parameter	Value (units $\kappa = 1$)
ω_m	1
κ	1
γ	1.4×10^{-3}
G	0.03
ϵ	0.4
$\overline{n}$	0.1

In the case of a quadratic interaction, sweeping through Δ would be expected to reveal a series of resonance peaks at intervals of $2\omega_m$ in the good cavity regime. This is due to interactions occurring where pairs of phonons are transferred to the resonator, a characteristic of the quadratic interaction. Analysis focuses on the 'bad cavity' limit, where the resonance peaks are not resolved, and the energy exchange occurs over a broad range of frequencies.

Figure 3.5 shows the average phonon number for the parameters of Table 3.1, as the detuning is swept. There are noticeable parallels to the behaviour observed in the case of linear coupling. Again, a broad resonance peak is observed, where several orders of resonance merge. The maximum in $\langle n \rangle$ at point D results from large numbers of phonons building up in the resonator, as multiple photons are absorbed. As previously the resonator evolves between three dynamical states, labelled A, C and D, representing a fixed point, limit cycle and bistability, respectively. These are illustrated via Wigner functions in Figure 3.6.
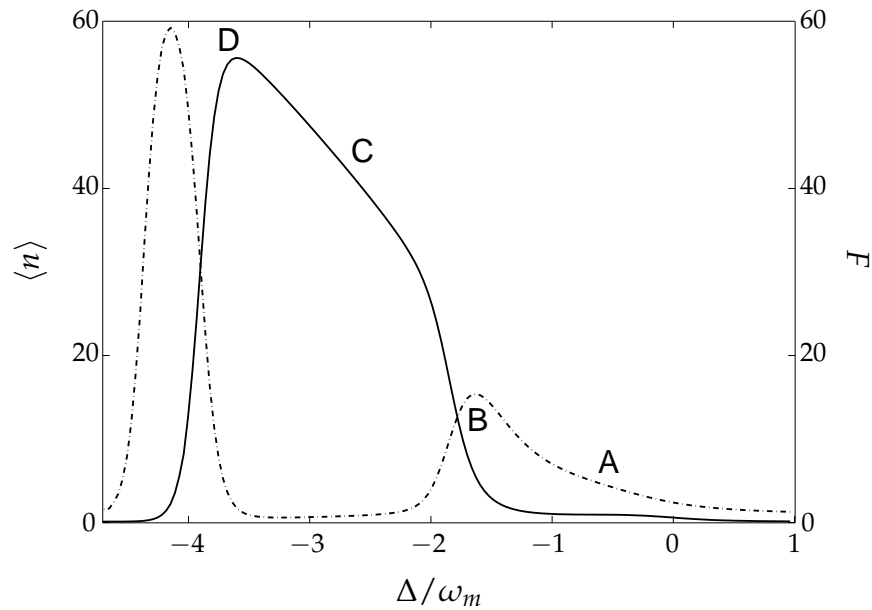
Figure 3.5: Average phonon number (solid line) alongside Fano factor (dot-dashed line) plotted as a function of the detuning, for parameters of Table 3.1.

Comparing the cases of linear and quadratic coupling, a notable difference is the transition between the fixed point and the limit cycle. Figure 3.6a shows the Wigner function in the regime where only the fixed point is stable, at low Δ. As Δ increases the limit cycle emerges whilst the fixed point remains stable, so that a bistability occurs at point B. This is predicted by the small amplitude approximation for γ_{BA}, which indicates that the stability condition for the fixed point is met over the entire range of Δ (see Chapter 2, Section 2.3.3). Although the fixed point solution remains stable as Δ increases, the probability of finding the resonator in this state is negligible at point C. This results in a state with an energy distribution which resembles

a Gaussian peak. The Wigner function here is shown in Figure 3.6b.

Near point D there is a large peak in F, as the probability density at the fixed point grows. The large separation of energies between the limit cycle and fixed point states causes a vast increase in the variance. Figure 3.6c shows the Wigner function. The peak in F is accompanied by a sharp drop in $\langle n \rangle$, as the limit cycle collapses.

(a) A: $\Delta = -0.5$ (b) C: $\Delta = -2.5$ (c) D: $\Delta = -3.6$
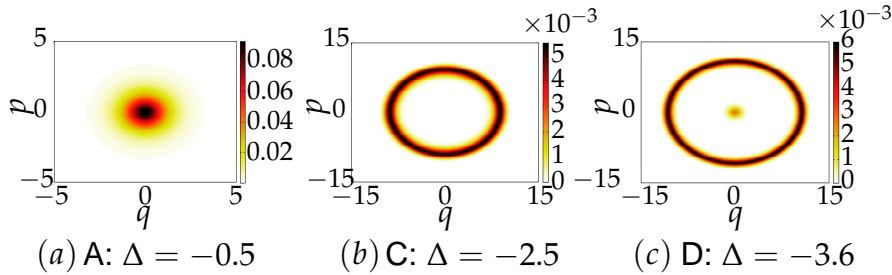
Figure 3.6: Evolution of the resonator Wigner density function as blue detuning is increased, corresponding to points in Figure 3.5, (a) Fixed point at A, (b) Limit cycle at C, (c) Bistability at D.

Figure 3.7 shows the evolution of the resonator state over the range of weak coupling, as G is varied and $\Delta = -2.5$. In this regime the resonator behaves in much the same way as for the case of linear coupling. Points A ,D and C mark the fixed point, bistability and limit cycle state, respectively. The inset shows a close up of the region where F drops to a minimum $F \approx 0.83$. The presence of sub-Poissonian states ($F < 1$) indicates a degree of number squeezing[10, 30] in the resonator. This will be explored further in the strong coupling regime.

3.4.2 *Behaviour at strong coupling*

Analysis of the resonator state where $G \sim \kappa$ reveals the emergence of multiple limit cycles, and a loss of the smooth Gaussian appearance to their probability peaks. Here, it is evident that the semi-classical description of the fluctuations will not be sufficient to describe the dynamics, and the non-linearity is strong (note that analytical and numerical results are compared in Section 3.5). Far into the strong coupling regime non-classical behaviour develops. The inset of Figure 3.7 illustrates the presence of sub-Poissonian states at low coupling. As with the linear case, the coupling strength must be increased further in order to see significant squeezing in the limit cycle, at the ex-
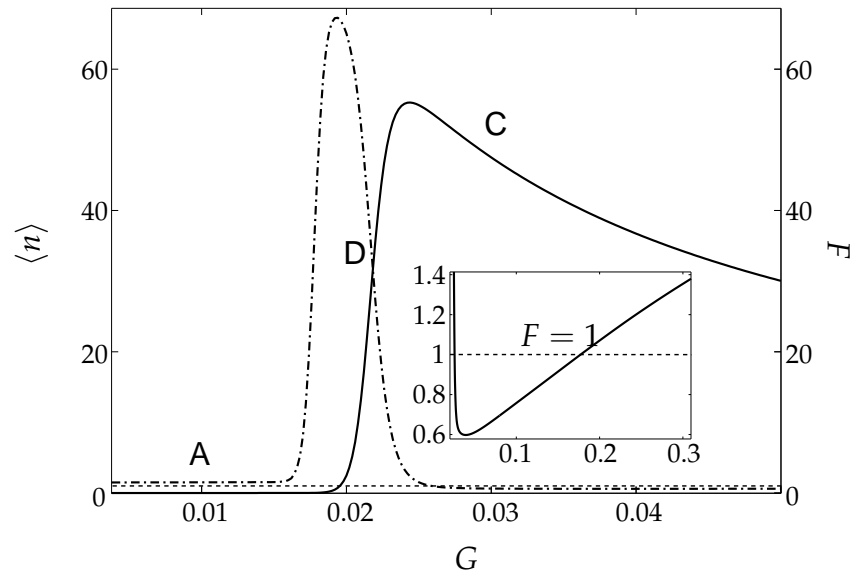
Figure 3.7: Average phonon number (solid) and Fano Factor (dot-dash) with respect to the mechanical coupling, G. The inset shows where the Fano factor passes below unity.

pense of encountering dynamical multistability, which causes $F \geq 1$. The dynamics in this regime are reminiscent of the linear coupling case, but some key differences are highlighted in the analysis to follow. As the coupling is increased negative regions occur in the Wigner function. These are explored separately below. The parameters used are the same as in Table 3.1, except $\bar{n} = 0$, whilst G is varied.

3.4.2.1 *Negative regions in the Wigner function*

Whilst Figure 3.7 displays the presence of sub-Poissonian states, non-classical features are stronger when $\bar{n} = 0$[12]. Figure 3.8 shows the Fano factor over a broad range of coupling values, with $\bar{n} = 0$. At $G = 0.04$ (labelled X) the Fano factor drops to a minimum $F \approx 0.6$. The corresponding probability distribution at this point is shown in the inset (red). These states are number squeezed[10, 12]. As the coupling is increased, the peak grows narrower as seen at point Y (green). With increasing coupling the peak grows narrower, but an additional peak emerges (shown by the blue distribution at point Y). This causes the Fano factor to increase, rising above above unity as the separation between the peaks increases.
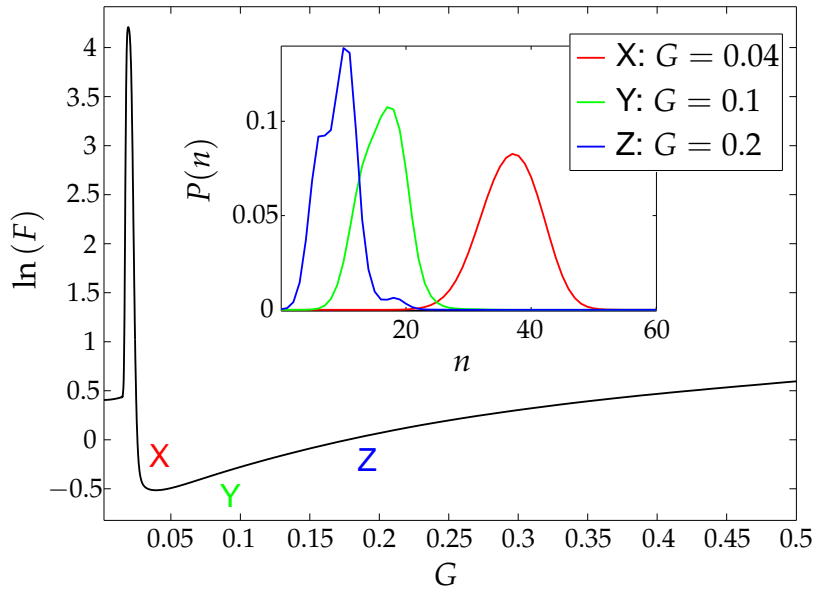
Figure 3.8: The Fano factor on a logarithmic scale, with respect to coupling. Inset shows the probability distribution for marked values of G.

As the coupling increases further, states emerge with negative regions in the associated Wigner functions. An example is given in Figure 3.9a, which shows the Wigner function alongside the corresponding probability distribution for $G = 1.35$. The probability peaks have lost their smooth Gaussian appearance and the Wigner function contains a ring of negative density.

(a)   (b)
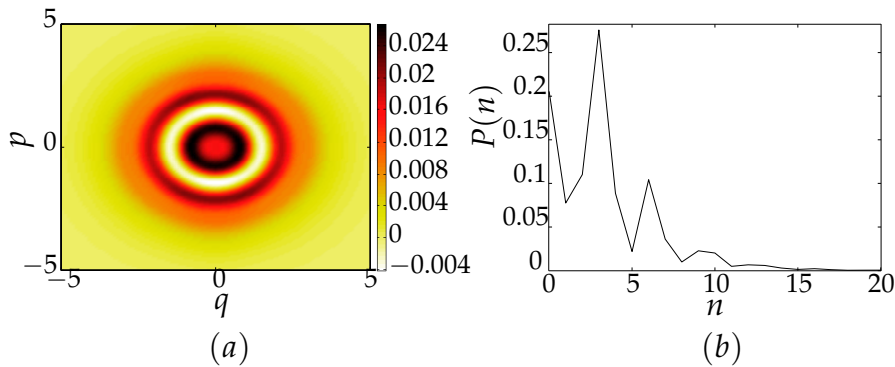
Figure 3.9: Non classical states of the resonator, indicated by the presence of negative densities in the Wigner function. (a) The Wigner function for $G = 1.35$, (b) the corresponding probability distribution in n, where multiple peaks appear.

For states in the strong coupling regime, the extent of negativity in the Wigner functions can be measured by the 'non-classical ratio'[12], η. This is defined as the ratio between the sums of the negative and positive elements in the Wigner function:

$$\eta = \frac{\sum_{i,j} |W_{ij}^{(-)}|}{\sum_{k,l} W_{kl}^{(+)}}, \tag{3.60}$$

where $W^{(+)}$ and $W^{(-)}$ are the amplitudes of positive and negative Wigner elements, respectively. The sums are over all elements in the Wigner density matrix, labelled by indices i, j and k, l.

Figure 3.10 shows numerical results in the strong coupling regime, as G and Δ are varied. The non-classical ratio is shown in Figure 3.10a, and displays a series of peaks. Looking at lines of constant coupling, at $G < 1$, the non-classical behaviour is concentrated towards higher order sidebands. As G is increased, the peaks in η shift towards lower $|\Delta|$, so that for $G = 3$, non-classical states are generated well below where two phonon resonance would be expected. It has been established in Chapter 2 that the effective value of Δ is shifted at strong coupling for the linear system, it seems likely that something similar is occurring here.

Over the strong coupling range, F remains above unity (Figure 3.10b), whilst highly non-classical states occur. This is due to the emergence of additional limit cycles at stronger couplings. As extra peaks in $P(n)$ emerge, F increases. As the peaks move inwards and merge with each other, this causes drops in F.

For highly non-classical states, the Wigner function is a series of concentric rings of densities alternating in sign, reminiscent of a Fock state (shown in Figure 2.11 of Chapter 2). The corresponding probability distribution consists of a number of sharp peaks, the separation of which results in an overall super-Poissonian state, $F > 1$, whilst displaying non-classicality[12]. This behaviour has been examined extensively for the case of linear coupling[10, 12], and is summarised in Chapter 2, Section 2.4.3.
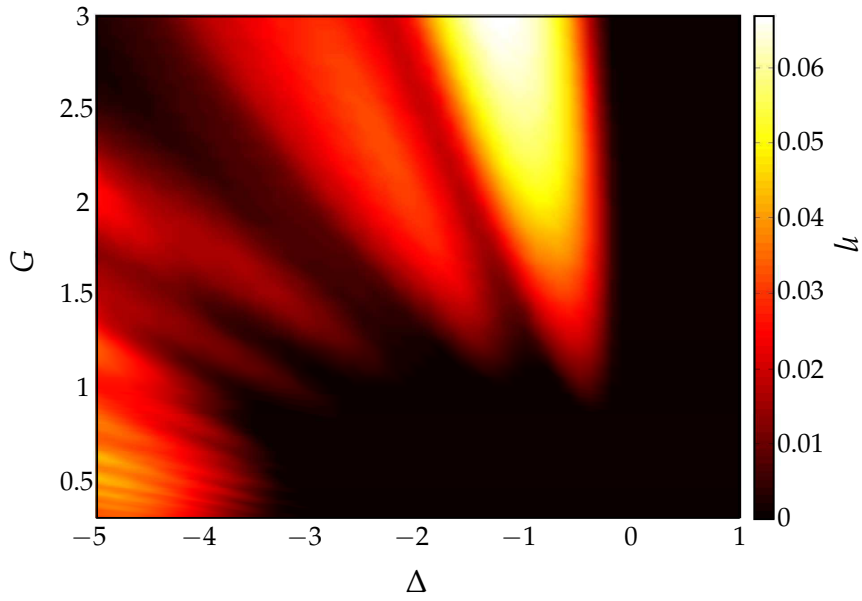
(a)
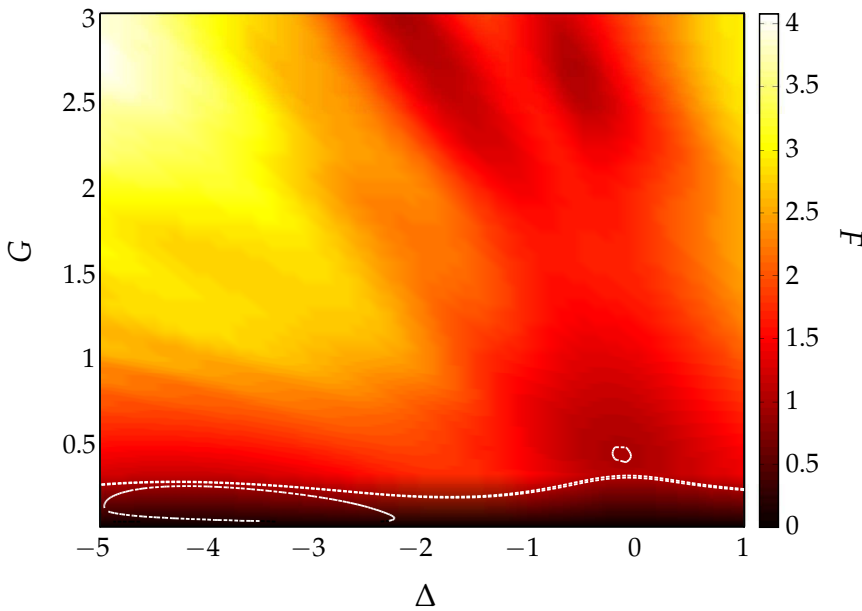
(b)

Figure 3.10: System dynamics in the strong coupling regime, as G and Δ are swept. (a) Non-classical ratio, as defined in Equation 3.60, and (b) Fano factor, with $\epsilon = 0.4$, $\omega_m = 1$, $\bar{n} = 0$, $\gamma = 0.0014$. In (b) the white contour indicates the region where $F < 1$ - generally the strong coupling regime produces state with $F > 1$, in spite of the high non-classical ratios.

3.5   COMPARISON BETWEEN ANALYTICS AND NUMERICS

The regime of weak coupling allows for a comparison between analytic and numerical calculations. For the parameters of Table 3.1, $\langle n \rangle$ and F are compared in Figures 3.11a and 3.11b for $\bar{n} = 0.1$, $\bar{n} = 1$, and $\bar{n} = 5$. Increasing the thermal phonon number results in a broadening of the curves in $\langle n \rangle$ and F. The off-resonance value of $\langle n \rangle$ increases and larger fluctuations allow phonons to build up over a wider range of Δ.

An increase in $\bar{n}$ results in greater thermal diffusion. Since the diffusion due to back action is independent of the thermal phonon number, at $\bar{n} = 5$, one approaches a regime where thermal fluctuations dominate[2]. Increasing $\bar{n}$ improves the accuracy of the analytic solution. Figure 3.11a shows some significant discrepancies, particularly at $\bar{n} = 0.1$. These include a frequency shift and an underestimate in the peak value of $\langle n \rangle$. As $\bar{n}$ increases the shift reduces, as does the discrepancy in the peak height. This suggests that inaccuracies in the semi-classical approximation arise largely from inaccuracies when calculating the diffusion due to back action, which plays a more prominent role in the dynamics as $\bar{n} \to 0$.

The Δ shift observed reduces as the thermal phonon number increases, but is also found to increase with G, indicating that it is a result of the approximate treatment of the non-linearity. In the thermal regime, the behaviour is dominated by thermal fluctuations which are described well by the semi-classical approximation. As the coupling is increased however, non-linear effects become more prominent, and the fluctuations not treated exactly by the truncated Wigner approximation cause a problem.

Figure 3.12 compares the limit cycle amplitudes deduced from numerical and analytic calculations. The solid line represents limit cycle energies found analytically by applying the energy balance condition. The crosses represent the position of numerical peaks in n. The data matches reasonably well, particularly over the region where the system strongly favours the limit cycle state, and Gaussian peaks are observed in $P(n)$. Discrepancies appear when the fixed point amplitude becomes much larger in comparison to the limit cycle amplitude.

Overall the analytic approximation provides an accurate picture of the limit cycle dynamics, suggesting again that the analytics of Figures 3.11a are limited by inaccuracies in the dif-

---

2 Over the range of energies considered, for parameters of case [i], $D_{BA}(E_0)$ is of the order 10^{-2}, compared to $D_{th} \approx 2.5$.
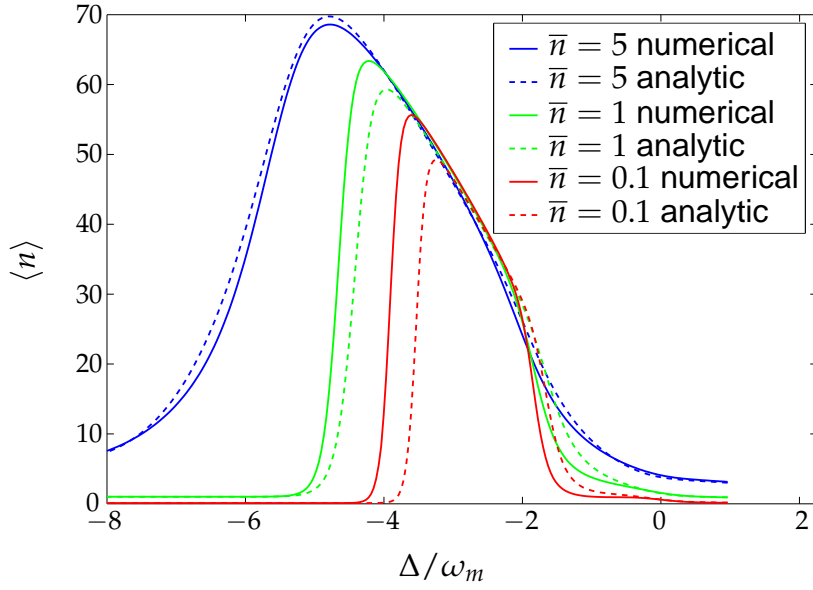
(a)
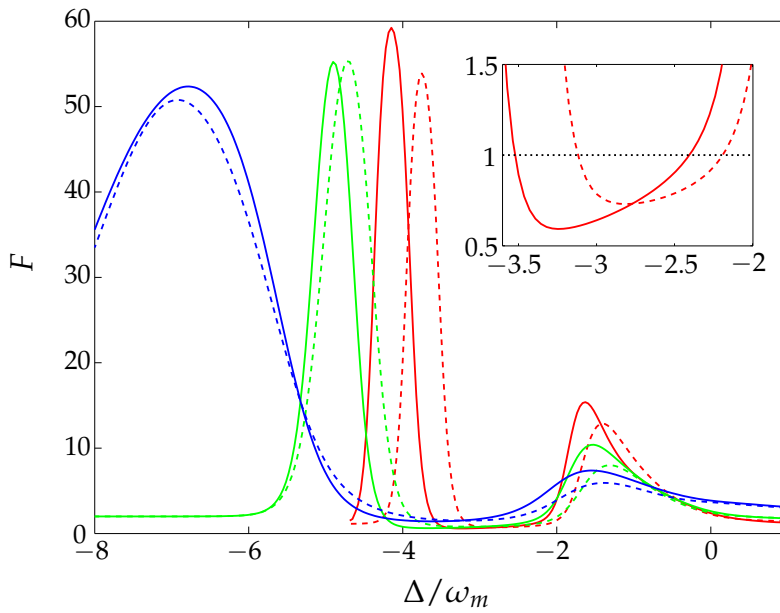
(b)

Figure 3.11: A comparison of (a) average phonon number and (b) Fano factor, for $\overline{n} = 0.1$ (red), $\overline{n} = 1$ (green) and $\overline{n} = 5$ (blue). Analytics are given by dashed lines and numerics in solid, remaining parameters are as in case [i]. Inset shows the minimum in the Fano factor for $\overline{n} = 0.1$, where sub-Poissonian statistics occur.

fusion calculation. Outside of the regions where the system favours the limit cycle state, large discrepancies are found in

$\langle n \rangle$ and F. The bistable state is marked by large fluctuations (peaks in F), resulting in greater inaccuracies in the calculation. It is apparent that the semi-classical approximation has difficulty capturing the large fluctuations of the quadratically coupled system.
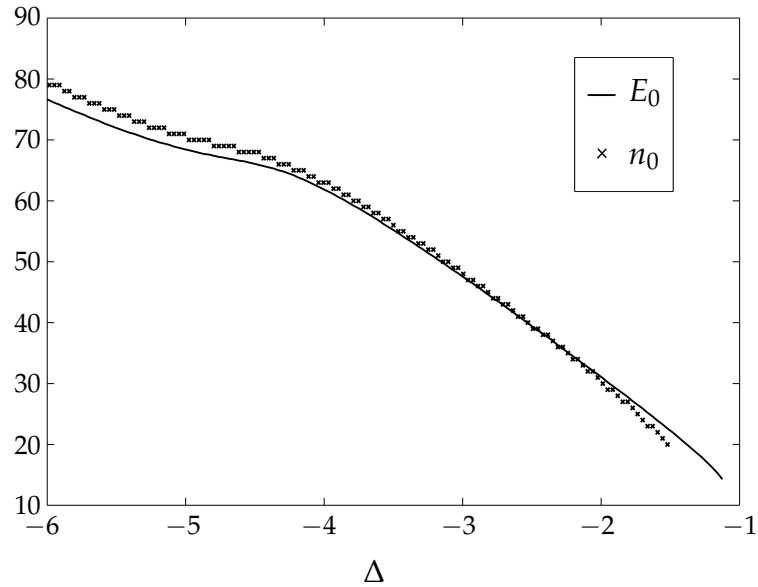
Figure 3.12: A comparison of the limit cycle dynamics for the parameters of the red curve in Figure 3.11a. Analytics (solid line) are generated via the energy balance and stability conditions, whilst numerical points (crosses) are peaks in $P(n)$.

For each value of $\overline{n}$, the agreement of the results depends on the state of the resonator. The analytics and numerics overlap quite closely in the region where the system favours a single limit cycle state. In this region, where higher energy states are occupied, the probability distributions can be usefully compared. This comparison is provided for each value of $\overline{n}$, in Figure 3.13. The analytic distribution $P(E)$ (blue) is plotted alongside numerical distribution $P(n)$ (black). The distribution is roughly Gaussian (the Gaussian approximation is shown in red) and fluctuations in this region are small. The increased accuracy of the semi-classical approximation is evident for $\overline{n} = 5$.

Figure 3.14 provides a comparison between the two calculations as G is varied. At low G (see inset), the fixed point is stable and low energies result in higher accuracy for the calculation. As G increases, and the bistability emerges, the curves begin to
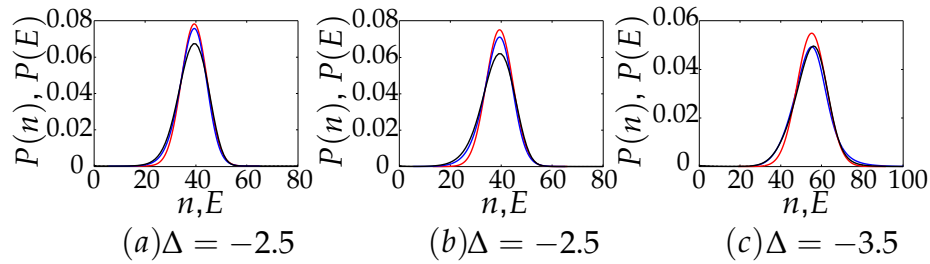
Figure 3.13: Probability distributions for the resonator in the limit cycle state for (a) $\bar{n} = 0.1$, (b) $\bar{n} = 1$ and (c) $\bar{n} = 5$, with numerics in black and analytics in blue. The Gaussian approximation is also shown in red.

diverge slightly. Larger discrepancies occur at the peak in $\langle n \rangle$. The large energies are accompanied by large fluctuations (the inset depicts this via a sharp peak in F). These fluctuations are not captured exactly and the analytics underestimate the peak. Once the resonator settles into a limit cycle at high G, the fluctuations reduce and the accuracy improves. The curves remain in agreement until $G \approx 0.3$, where they begin to diverge. Overall, the discrepancies in the curve are more pronounced as G increases, but are also dependent on the state of the resonator. The bistable state is generally the least accurately described by the semi-classical approximation. In contrast, the limit cycle is generally well described for $G \leq 0.3$.
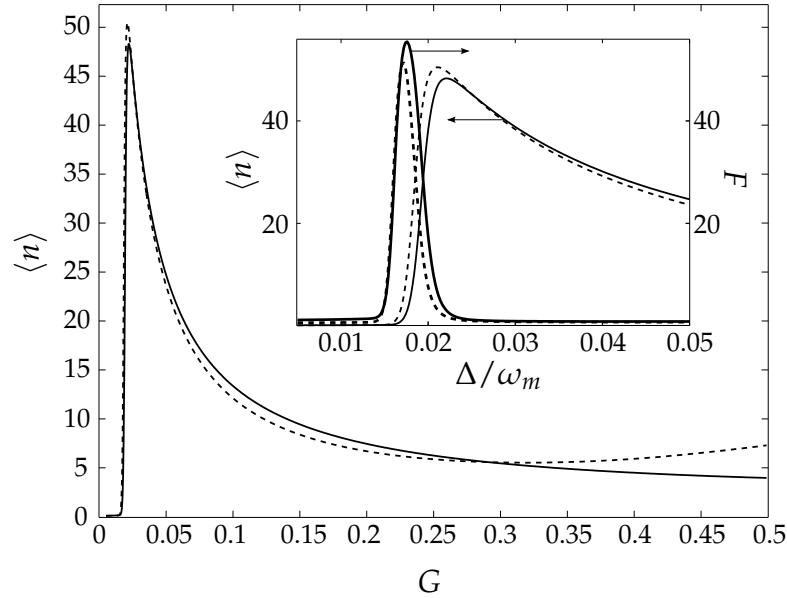
Figure 3.14: The average phonon number with respect to G, for $\Delta = -2.5$, for numerical (solid) and analytic (dashed) calculations. Inset shows $\langle n \rangle$ and F in the region of low G, where the calculation is approximately accurate.

3.6   CONCLUSION

This chapter has investigated an optomechanical system with rather different geometry compared to the previous chapter. By placing a mechanical element at the centre of a cavity and allowing partial transmission of radiation, quadratic coupling is achieved. In the blue detuned limit this system offers a range of dynamical behaviours, similar in many aspects to the linear case. One can observe transition between the same three resonator states: fixed point, limit cycle and bistability. However, differences are observed in the transitions. The resonator passes through two bistable regimes as the laser is tuned around the mechanical resonance, resulting in a more symmetric looking resonance peak in the phonon number.

The strong coupling regime offers some interesting behaviour. As in the linearly coupled system, negative regions are observed in the Wigner function for values of G close to unity. In addition, there are regions where number squeezing occurs ($F < 1$) but these occur at much weaker couplings. It is worth noting that, for the quadratic case, a lower value of $F = 0.6$ is reached, outside of the resolved sideband limit.

As in Chapter 2, the truncated Wigner approximation has been applied to the quadratic system. The result is a similar set of Langevin equations for the cavity and resonator. These have been solved by separating the timescales of the cavity and resonator, in order to obtain a probability distribution for the resonator. Unfortunately the third order derivatives, which were ignored in the approximation, turn out to have more significance in the quadratic system. The non-linearities are stronger, so that approximations which are valid for linear coupling lead to inaccuracies in calculating diffusion in the quadratic case, particularly when large fluctuations dominate the dynamics. This results in difficulty describing the bistable regime, and the weighting of peaks in the probability distribution are not accurately captured, which results in inaccuracies in $\langle n \rangle$. However, a certain amount of success is found in describing regions where fluctuations are small - for example limit cycles with Gaussian peaks. Additionally regimes such as cooling and large thermal fluctuations are described accurately.

4

STABILITY, DAMPING AND COOLING IN A TWO-MODE SYSTEM

4.1 INTRODUCTION

The previous chapter introduced the dispersive optomechanical system, where a membrane at the centre of the cavity provides the mechanical mode. The coupling between the resonator and cavity was found to range between approximately quadratic [45] and approximately linear[67], depending on the position of the mechanical element[17, 25]. Increasing the rate at which photons tunnelled through the membrane increased the separation between the frequencies of the two optical modes[16], prohibiting transitions and allowing a single mode to be probed with careful selection of the drive frequency.

In this chapter the focus is shifted towards a regime where energy exchange occurs between photonic modes as well as with the mechanical mode. A reduced tunnelling rate through the membrane brings the system into a regime where the frequency separation between optical modes is similar to the mechanical frequency. In this case, the absorption or emission of a phonon in the resonator induces transitions between photon modes[16, 68]. As a result, one must now account for energy exchange between different photon modes as well as between the cavity and resonator. The system is thus formulated in terms of the mechanical mode and photonic modes for the left and right chambers of the cavity.

This chapter explores the effect of damping and cooling, when $\omega_m \sim g$. The case of linear coupling to a single optical mode was addressed briefly in Chapter 2, where an approximate analytical expression was obtained for the effective temperature in the regime of sideband cooling. It has been shown theoretically [13, 35] and experimentally[14] that a resonator can be cooled to the quantum ground state, by coupling it to a single optical mode.

This chapter investigates whether ground state cooling is possible for the dispersive system, in the regime where both optical modes interact with the membrane. Since radiation is allowed to tunnel through the mechanical element, realisation of such

systems is possible without the problem of fabricating highly reflecting mirrors with large mechanical quality factors [18, 19]. Such a feat is desirable, as it would lend itself to less challenging experimental systems.

The chapter is organised as follows: The system is introduced in Section 4.2, and the equations of motion presented. Section 4.3 explores the static bistability, a phenomenon which arises in strongly driven systems[69]. This allows one to determine the regime in which the resonator reaches a stable state, a prerequisite for cooling. Section 4.4 explores the fluctuations and presents a linearized calculation of the mechanical noise spectrum. Section 4.4.1 uses the noise spectrum to determine the damping due to back action in the red detuned regime. This allows a comparison between the single mode and double mode systems by varying the tunnelling through the membrane. The linearized calculation then allows an effective phonon number to be deduced in Section 4.4.2, which also explores back action induced cooling and compares results to the single mode case.

4.2   THE SYSTEM

The system under consideration takes the same basic form as that introduced in Chapter 3 (and illustrated schematically in Figure 3.1a), but here a rather different set of parameters are explored. The membrane is mounted at a position q_0, and has a tunnelling rate g. In contrast to the previous Chapter, here a regime is explored where $g \sim \omega_m$, so that radiation is partially reflected and partially transmitted through the membrane. The dispersion diagram in Figure 4.1 illustrates the optical modes in the system. For the case $\omega_m > 2g$ (as is the case in Figure 4.1), the minimum mode spacing is small enough that there exists a displacement q' such that the upper and lower dispersion bands are separated by a factor of the mechanical frequency. Transitions between the optical modes then occur with the absorption or emission of a phonon[16], when the system is driven near one of the cavity frequencies.

Equation 3.3 of Chapter 3 introduces the Hamiltonian for the dispersive system. The effective Hamiltonian is obtained, this time, via a unitary transformation $U = e^{iH_0 t}$ with

$$H_0 = \omega_d \left(a_L^\dagger a_L + a_R^\dagger a_R \right), \tag{4.1}$$
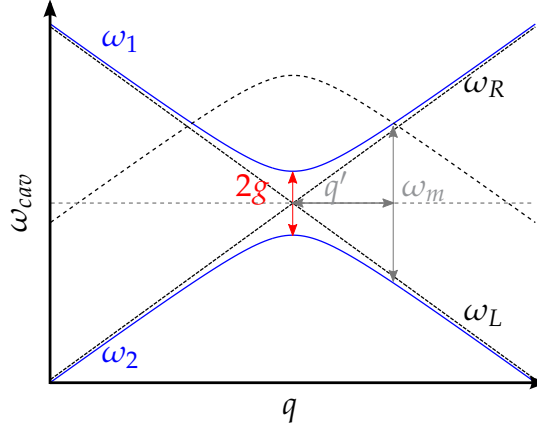
Figure 4.1: Dispersion diagram showing how the frequencies optical modes in the cavity vary with membrane displacement, q. Uncoupled modes of frequency ω_L and ω_R are illustrated by black dashed lines, whilst the coupled modes, ω_1 and ω_2, are shown in blue solid lines. The dotted grey line marks the cavity frequency when the membrane is at $q = 0$. For this example $\omega_m > 2g$ and there exists a displacement q' for which the upper and lower dispersion bands are separated by the mechanical frequency - this is illustrated by the sideband (dashed curve), which are displaced by ω_m from the curves.

giving

$$
\begin{aligned}
H_{eff} &= \Delta(a_L^\dagger a_L + a_R^\dagger a_R) + g(a_L^\dagger a_R + a_R^\dagger a_L) + \lambda q(a_R^\dagger a_R - a_L^\dagger a_L) \\
&\quad + \frac{1}{2}\omega_m(p^2 + q^2) + \Omega(a_L + a_L^\dagger),
\end{aligned} \tag{4.2}
$$

where the laser is detuned by $\Delta = \omega_0 - \omega_d$, and λ is a constant parametrising the coupling strength.

Equations of motion can be deduced for the resonator variables q and p, as well as the cavity operators, using the input-output formalism for optical cavities[1]. This approach takes into account the fact that the left and right cavities are weakly coupled to the large number of electromagnetic modes outside the fixed mirrors[1]. The Heisenberg equations of motion of the closed system are modified to include damping terms and fluctuations described by the operators ζ (for the resonator), a_L^{IN}

(for the left cavity) and a_R^{IN} (for the right cavity). The Heisenberg equations deduced take the form

$$\dot{a}_L = -i\Delta a_L + i\lambda q a_L - ig a_R - i\Omega - \frac{\kappa}{2}a_L + \sqrt{\kappa}a_L^{IN} \quad (4.3)$$

$$\dot{a}_R = -i\Delta a_R - i\lambda q a_R - ig a_R - \frac{\kappa}{2}a_R + \sqrt{\kappa}a_R^{IN} \quad (4.4)$$

$$\dot{q} = \omega_m p + \zeta \quad (4.5)$$

$$\dot{p} = -\omega_m q - \gamma p + \lambda(a_L^\dagger a_L - a_R^\dagger a_R). \quad (4.6)$$

Here the mechanical mode is subject to a viscous force, resulting in a damping rate γ and a Brownian stochastic force ζ[35]. This force has $\langle \zeta(t) \rangle = 0$ and is described by the correlator

$$\langle \zeta(t)\zeta(t') \rangle = \frac{\gamma}{\omega_m} \int \frac{d\omega}{2\pi} e^{-i\omega(t-t')} \omega \left[\coth\left(\frac{\omega}{2k_B T}\right) + 1 \right], (4.7)$$

at temperature T. The cavity, meanwhile is damped at rate κ and subject to vacuum radiation input noise, described by the following correlators:

$$\langle a_L^{IN}(t) a_L^{IN\dagger}(t') \rangle = \delta(t - t') \quad (4.8)$$

$$\langle a_R^{IN}(t) a_R^{IN\dagger}(t') \rangle = \delta(t - t') \quad (4.9)$$

where it is assumed that $\omega_L \gg k_B T$, so thermal fluctuations can be neglected. With the intention of investigating cooling in the two mode system, Equations 4.3 to 4.6 are expressed in terms of small fluctuations about the mean field values: $v = \langle v \rangle + \delta v$, where $v = q, p, a_L, a_R$. Separating fluctuating and average dynamics, one then has two sets of equations to deal with:

$$P = \frac{\gamma}{\omega_m}Q \quad (4.10)$$

$$Q = \frac{\lambda}{\omega_m}\left(|\alpha_L| - |\alpha_R|\right) \quad (4.11)$$

$$\alpha_L = \frac{-i\Omega\left[\frac{\kappa}{2} + i(\Delta_R + \lambda Q)\right]}{\left[\frac{\kappa}{2} + i(\Delta_R + \lambda Q)\right]\left[\frac{\kappa}{2} + i(\Delta_L - \lambda Q)\right] + g^2} \quad (4.12)$$

$$\alpha_R = \frac{-g\Omega}{\left[\frac{\kappa}{2} + i(\Delta_R + \lambda Q)\right]\left[\frac{\kappa}{2} + i(\Delta_L - \lambda Q)\right] + g^2}, \quad (4.13)$$

for the mean fields $Q = \langle q \rangle$, $P = \langle p \rangle$, $\alpha_L = \langle a_L \rangle$ and $\alpha_R = \langle a_R \rangle$. In Equations 4.12 and 4.13, the cavity equilibrium detunings Δ_L and Δ_R have been introduced:

$$\Delta_L = \Delta - \Delta\omega \quad (4.14)$$

$$\Delta_R = \Delta + \Delta\omega, \quad (4.15)$$

with $\Delta\omega = \lambda q_0$, which parametrises the detuning between the two cavity modes when the resonator is in the equilibrium position, q_0.

The fluctuations are found to obey

$$\dot{\delta q} = \omega_m \delta p \tag{4.16}$$

$$\dot{\delta p} = -\omega_m \delta q - \gamma \delta p + \zeta$$
$$\lambda(\alpha_L \delta a_L^\dagger + \alpha_L^* \delta a_L - \alpha_R \delta a_R^\dagger - \alpha_R^* \delta a_R), \tag{4.17}$$

$$\dot{\delta a_L} = -\left[i\Delta_L' + \frac{\kappa}{2}\right]\delta a_L + i\lambda\alpha_L\delta q - ig\delta a_R + \sqrt{\kappa}a_L^{IN} \tag{4.18}$$

$$\dot{\delta a_R} = -\left[i\Delta_R' + \frac{\kappa}{2}\right]\delta a_R - i\lambda\alpha_R\delta q - ig\delta a_L + \sqrt{\kappa}a_R^{IN}, \tag{4.19}$$

These equations have been linearized, so that squared fluctuation terms are discarded. This requires fluctuations to be small compared to mean field values associated with the cavity (α_L and α_R) which is an appropriate assumption to make when exploring the regime of cooling. The coupling λ should also be small. An additional frequency shift arises from the fixed point Q, so Δ_L' and Δ_R' are defined:

$$\Delta_L' = \Delta_L - \lambda Q \tag{4.20}$$

$$\Delta_R' = \Delta_R + \lambda Q. \tag{4.21}$$

The next section deals with the fixed point analysis, before fluctuations are addressed in Section 4.4.

4.3 FIXED POINT ANALYSIS AND THE STATIC BISTABILITY

This section investigates stable equilibrium positions of the resonator, and addresses the phenomenon of the static bistability. This occurs when multiple fixed point solutions emerge, so that the resonator can reach a stable state where it fluctuates about one of two different positions. Recent publications[35, 69] have addressed this issue, and its impact on cooling for the case of a single optical mode. This is now extended to the two mode case.

One can gain useful insight by considering a potential function for the mechanical resonator, deduced from the Hamiltonian [49]. This analysis does not account for dissipation[47, 48] and so will not serve only as a rough guide to the fixed point dynamics, but provides an intuitive picture of how bistability arises. More detailed analysis follows, accounting for dissipation in the cavity and resonator modes.

Assuming that the ring down time for the cavity modes is short compared to the mechanical period $\kappa > \omega_m$, one can adopt a simple effective potential description[1]. This effective potential, $V(q)$, contains a harmonic contribution, $V_h = \frac{1}{2}\omega_m Q^2$, as well as a contribution from the radiation pressure force acting on the membrane, V_{rad}. The radiation pressure arises when the cavity is driven, causing photons to build up in each chamber. Collisions with the membrane exert a net force, proportional to the difference in occupation between the left and right modes:

$$F_{rad} = \lambda(|\alpha_L|^2 - |\alpha_R|^2). \tag{4.22}$$

The assumption that $\kappa > \omega_m$ allows one to calculate α_L and α_R from Equations 4.12 and 4.13, assuming a fixed Q value. The force F_{rad} can be written as the derivative of a potential, V_{rad}:

$$F_{rad} = -\frac{\partial V_{rad}}{\partial Q} \tag{4.23}$$

The potential for the mechanical mode is the sum of contributions from V_{rad} and the harmonic restoring force,

$$V(Q) = V_{rad} + \frac{1}{2}\omega_m Q^2 \tag{4.24}$$

Examples of the effective potential are shown in Figure 4.2. The red and blue curves are single well potentials, signifying a single stability in the fixed point dynamics. As the drive strength passes through $\Omega = 35.35$ (green curve) a double well emerges, indicating the presence of a static bistability. This phenomenon has been investigated in the case of a resonator coupled to a single cavity mode[69, 35]. As a rough estimate, bistabilities appear where the correction to the mechanical frequency is negative and of the same order as the mechanical frequency, $\delta\omega \sim -\omega_m$[49]. For this to occur, both cavity modes must be red detuned ($\Delta_L, \Delta_R > 0$) and the drive strength must be large ($\Omega \gg \kappa$).

A more general (and more formal) approach is to analyse the stability of the fixed points in the system. The fixed points are found by solving Equations 4.10 to 4.13 simultaneously. The result is a fifth order polynomial in Q,

$$a_5 Q^5 + a_4 Q^4 + a_3 Q^3 + a_2 Q^2 + a_1 Q + a_0 = 0, \tag{4.25}$$

---

1 This means the cavity can be assumed to react instantaneously to the resonator's motion. This may not always be the case, but a more detailed analysis in Section 4.3.1 accounts for $\kappa \lesssim \omega_m$.
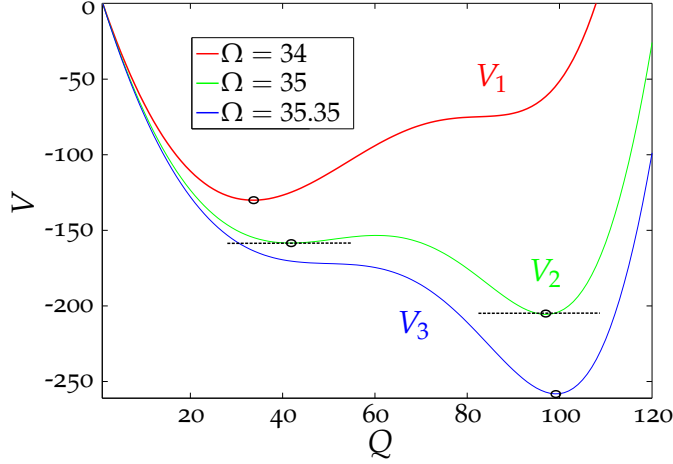
Figure 4.2: The mechanical potential, $V(Q) = V_{rad} + \frac{1}{2}\omega_m Q^2$, shown for three different drive strengths: $\Omega = 34$ (red), $\Omega = 35$ (green) and $\Omega = 35.35$ (blue). Stabilities (minima in the curve) are marked by circles, with a bistability occurring for $\Omega = 35$. Parameters are $\omega_m = 0.5$, $\kappa = 1$, $\gamma = 1 \times 10^{-4}$, $g = 0.1$, $\lambda = 0.01$, $\Delta\omega = 0$ and $\Delta = 2\omega_m$.

with coefficients

$$a_5 = \lambda^4 \tag{4.26}$$

$$a_4 = 4\Delta\omega\lambda^3 \tag{4.27}$$

$$a_3 = \left[2\left(\frac{\kappa^2}{4} - \Delta_R\Delta_L + g^2\right) + 4\Delta\omega^2\right]\lambda^2 \tag{4.28}$$

$$a_2 = 4\lambda\Delta\omega\left(\frac{\kappa^2}{4} - \Delta_R\Delta_L + g^2\right) - \frac{\Omega^2\lambda^3}{\omega_m} \tag{4.29}$$

$$a_1 = \left(\frac{\kappa^2}{4} - \Delta_R\Delta_L + g^2\right)^2 + \kappa^2\Delta^2 - 2\frac{\Omega^2\lambda^2\Delta_R}{\omega_m} \tag{4.30}$$

$$a_0 = -\frac{\lambda}{\omega_m}\Omega^2\left(\frac{\kappa^2}{4} + \Delta_R^2 - g^2\right), \tag{4.31}$$

The polynomial in Equation 4.25 yields five possible solutions for Q, not all of which are real. Since complex solutions always appear in conjugate pairs, one finds that only one, three or five real solutions can be found. The potential V_{rad} is proportional to the difference in photon numbers in each chamber. Since this is proportional to Ω^2, the driving strength can be varied to explore the emergence of bistabilities.

Figure 4.3a maps the presence of real solutions to Equation 4.25 as a function of Ω for the parameters of Figure 4.2. Over this range of driving strengths, three solutions emerge, corre-

sponding to the three branches of the curve. These are identified as extrema in the potential. Coloured vertical dotted lines identify the specific parameters which produce the potentials in Figure 4.2. Note the presence of three solutions for $\Omega_2 = 35$. The central branch of the curve (dotted line) represents the unstable solution, or the maximum in the potential. The stable branches coincide with minima in $V(q)$.

(a)   (b)
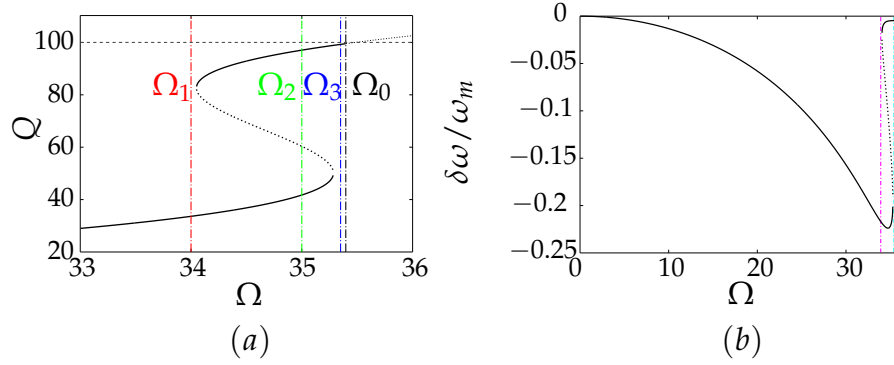
Figure 4.3: Illustration of the static bistability shown through (a) real solutions to Equation 4.25 and (b) the resonator frequency shift, $\delta\omega$ (calculated later in Section 4.4.1). Stable branches of the curves are in solid and unstable branches are dotted. In (a) the three coloured vertical lines correspond to the potentials shown in Figure 4.2, where intersections with the stable(unstable) branches correspond to minima(maxima) in the potential. The black vertical line is drawn at Ω_0, where the instability occurs. In (b) the coloured lines mark the region of bistability. Parameters are the same as for Figure 4.2.
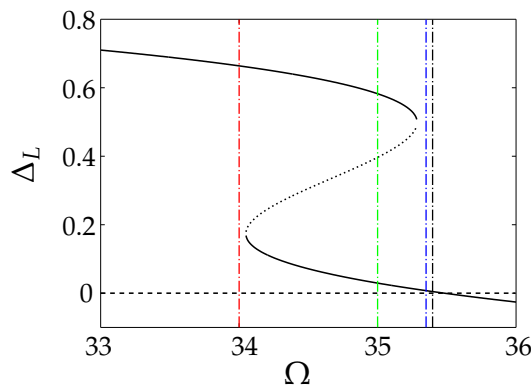
Figure 4.4: The detuning of the left cavity mode, as the drive strength (as thus the fixed point displacement) is varied, causing a cavity shift. At a point close to Ω_0, the detuning becomes negative, so that the left mode is driven above resonance.

Figure 4.3a shows the presence of fixed point solutions up to $\Omega = \Omega_0$. At this point, the fixed points all become unstable and the mechanical mode settles into a state of stable oscillations[69, 39]. Equation 4.20 describes how the red detuning in the left cavity reduces as the fixed point position Q increases. At the point where $\lambda Q = \Delta_L$ (marked by the horizontal dashed line), Δ_L' changes sign, such that the left optical mode is driven above resonance, and energy is no longer extracted from the resonator to drive the cavity. It is close to this point that the instability occurs (at Ω_0) and the resonator settles into a state of fixed amplitude oscillations. Figure 4.4 shows the detuning of the left cavity, Δ_L', as Ω is varied, with the onset of instability Ω_0 marked by a vertical black line. The three Ω values that produce the potentials in Figure 4.2 are also shown.

Figure 4.3b indicates the behaviour of the frequency shift over the range of Figure 4.3a. Towards the bistable region, the frequency shift drops to a minimum, satisfying the condition $\delta\omega \sim -\omega_m$. Far from the bistable range, $|\delta\omega| \ll \omega_m$, providing a rough estimate of where static bistabilities are likely to occur.

4.3.1   Routh Hurwitz analysis

Up to this point, solving Equation 4.25 has indicated possible fixed point solutions, with no explicit indication of their stability. Plotting the potential at a given Ω value (Figure 4.2) indicates which of the solutions occurring at that point are stable, in the limit where $\kappa > \omega_m$ and losses are small. A more accurate form of stability analysis is possible by applying the Routh Hurwitz criterion to the solutions of Equations 4.3 to 4.6. This will provide a method of analysis which accounts for the dissipation in optomechanical systems. This criterion takes the form of two conditions which, if met, determine that a fixed point solution is stable[70]. When the fixed point solutions are stable, one expects the system undergo decaying oscillations[69]. Routh-Hurwitz analysis will determine whether or not fluctuations in the system decay with time, for a given fixed point solution - thus indicating its stability. A full detailed description of the analysis is given in Appendix E.

4.3.1.1   Single mode case

The analysis has previously been applied to the reflective system (with a single optical mode), where analysis produces some

simple analytic expressions [35, 69]. Analysis for the single mode system is briefly reviewed [69] before the two mode case is considered. The equations of motion for the fluctuations in this case an be written as

$$\dot{\vec{v}}(t) = M\vec{v}(t),\tag{4.32}$$

with $\vec{v} = (\ \delta q \quad \delta p \quad X \quad Y\ )^{\text{T}}$, where X and Y defined as

$$X = \frac{\delta a + \delta a^{\dagger}}{\sqrt{2}}\tag{4.33}$$

$$Y = \frac{\delta a - \delta a^{\dagger}}{i\sqrt{2}},\tag{4.34}$$

for the single optical mode, a. The noise terms have been dropped to write Equation 4.32, and will be ignored for the remainder of this section, since they do not affect the fixed point analysis. The matrix M is given by

$$M = \begin{pmatrix} -0 & \omega_m & 0 & 0 \\ -\omega_m & -\gamma & G & 0 \\ 0 & 0 & -\frac{\kappa}{2} & \Delta' \\ G & 0 & -\Delta' & -\frac{\kappa}{2} \end{pmatrix},\tag{4.35}$$

where $\Delta' = \Delta - \lambda Q$ and $G = \sqrt{2}\lambda\alpha$, for fixed points Q and α. The fixed point values follow from the relations

$$\lambda^2 Q^3 - 2\Delta\lambda Q^2 + \left(\frac{\kappa^2}{4} + \Delta^2\right)Q - \frac{\lambda\Omega^2}{\omega_m} = 0,\tag{4.36}$$

and

$$\alpha = \frac{-i\Omega}{\frac{\kappa}{2} + i(\Delta - \lambda Q)}.\tag{4.37}$$

Since a single optical mode is present, up to three real solutions can exist for Q. Stability is expected when the eigenvalues, Λ, of matrix, M, satisfy $\Re[\Lambda] < 0$. Whether this condition is met can be determined by Routh Hurwitz analysis on the polynomial equations for the eigenvalues (outlined in Appendix E). This gives a method of determining whether roots of a polynomial have negative real coefficients and are therefore stable.

Analysis of the solutions for Q reveals stabilities are determined by a quantity η_s, given by

$$\eta_s = 1 - \frac{G^2\Delta}{\omega_m(\frac{\kappa^2}{4} + \Delta^2)}.\tag{4.38}$$

When this quantity lies in the range $0 < \eta_s < 1$, the solution Q is stable[35, 69]. Figure 4.5 details the results of stability analysis in the single mode case. When a static bistability arises, the curve forms three branches, with the upper and lower branches representing stable solutions and the central branch representing unstable solutions. This is illustrated by the solutions, Q, together with their corresponding η_s values.

$$(a) \qquad\qquad\qquad (b)$$
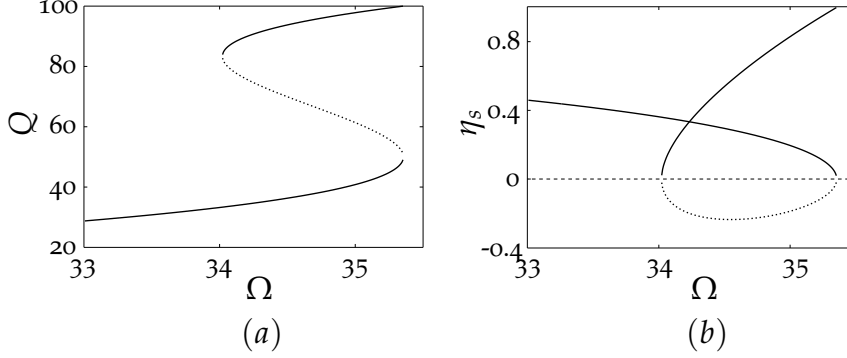
Figure 4.5: Stability analysis for the single mode case: (a) Real solutions to Q and (b) the bistability parameter η_s for the solutions. In regions of bistability, solutions for Q lie on one of three branches of a curve. The stable solutions lie along the upper and lower branches (where $0 < \eta < 1$), with the central branch being unstable - this corresponds to the negative branch of η_s. Parameters used are $\omega_m = 0.5$, $\Delta = 2\omega_m$, $\lambda = 0.01$, $\kappa = 1$ and $\gamma = 10^{-4}$.

4.3.1.2   *Double mode case*

Returning to the case of two optical modes, a more detailed account of the Routh Hurwitz analysis for solutions to Equation 4.25 follows. Defining the following variables,

$$X_{L(R)} = \frac{\delta a_{L(R)} + \delta a_{L(R)}^\dagger}{\sqrt{2}} \qquad (4.39)$$

$$Y_{L(R)} = \frac{\delta a_{L(R)} - \delta a_{L(R)}^\dagger}{\sqrt{2}} \qquad (4.40)$$

$$(4.41)$$

a similar matrix equation for Equations 4.16 to 4.19 is written:

$$\dot{\vec{v}}(t) = M\vec{v}(t), \qquad (4.42)$$

for vector $\vec{v}(t)^T = \begin{pmatrix} X_L(t) & Y_L(t) & X_R(t) & Y_R(t) & \delta q & \delta p \end{pmatrix}$, where the matrix M is given by

$$M = \begin{pmatrix} -\frac{\kappa}{2} & \Delta'_L & 0 & g & G'_L & 0 \\ -\Delta'_L & -\frac{\kappa}{2} & -g & 0 & G_L & 0 \\ 0 & g & -\frac{\kappa}{2} & \Delta'_R & -G'_R & 0 \\ -g & 0 & -\Delta'_R & -\frac{\kappa}{2} & -G_R & 0 \\ 0 & 0 & 0 & 0 & 0 & \omega_m \\ G_L & -G'_L & -G_R & G'_R & -\omega_m & -\gamma \end{pmatrix}, \quad (4.43)$$

and the following are defined by the fixed point values,

$$G^+_{L(R)} = \lambda \frac{\alpha_{L(R)} + \alpha^*_{L(R)}}{\sqrt{2}} \quad (4.44)$$

$$G^-_{L(R)} = i\lambda \frac{\alpha_{L(R)} - \alpha^*_{L(R)}}{\sqrt{2}} \quad (4.45)$$

Note that the fixed point variables have an implicit Q dependence. Stability is again determined by the eigenvalues, Λ, of the matrix M. Solving for these gives

$$|M - \Lambda| = 0. \quad (4.46)$$

Recall that Δ'_L and Δ'_R are functions of Q, so that there exists a different matrix for each branch of the curve in Figure 4.3a. Solving the eigenvalue problem, a sixth order polynomial is obtained to determine Λ:

$$a_6\Lambda^6 + a_5\Lambda^5 + a_4\Lambda^4 + a_3\Lambda^3 + a_2\Lambda^2 + a_1\Lambda + a_0 = 0, \quad (4.47)$$

where the coefficients are given by

$$a_6 = 1 \quad (4.48)$$

$$a_5 = 2\kappa + \frac{\gamma}{2} \quad (4.49)$$

$$a_4 = a + \kappa(\kappa + 2\gamma) \quad (4.50)$$

$$a_3 = \kappa a + \gamma b + \kappa\left(\omega_m^2 + \kappa\gamma\right) \quad (4.51)$$

$$a_2 = \kappa\gamma b + \kappa^2\omega_m^2 + \beta + \epsilon \quad (4.52)$$

$$a_1 = \kappa\beta + \gamma\epsilon \quad (4.53)$$

$$a_0 = \omega_m^2\epsilon - 2\lambda^2\omega_m|\alpha_L|^2\chi_L - 2\lambda^2\omega_m|\alpha_R|^2\chi_r$$
$$+ \omega_m g\lambda^2 \left(\alpha^*_R\alpha_L + \alpha^*_L\alpha_R\right)\chi_1, \quad (4.54)$$

with

$$a = 2g^2 + \omega_m^2 + \frac{\kappa^2}{2} + (\Delta_L')^2 + (\Delta_R')^2, \tag{4.55}$$

$$b = a - \omega_m^2 \tag{4.56}$$

$$\beta = 2\omega_m\lambda^2 \left[g(\alpha_L^*\alpha_R + \alpha_R^*\alpha_L) - \Delta_L'|\alpha_L|^2 - \Delta_R'|\alpha_R|^2 \right]$$
$$+ \omega_m^2, \tag{4.57}$$

$$\epsilon = \frac{\kappa^4}{16} + \frac{\kappa^2}{4}\left((\Delta_L')^2 + (\Delta_R')^2\right) + (\Delta_L'\Delta_R' - g^2)^2$$
$$+ \frac{\kappa^2}{2}g^2, \tag{4.58}$$

$$\chi_L = \Delta_L'(\Delta_R')^2 + 4\gamma^2\Delta_L' - g^2\Delta_R' \tag{4.59}$$

$$\chi_R = \Delta_R'(\Delta_L')^2 + 4\gamma^2\Delta_R' - g^2\Delta_L' \tag{4.60}$$

$$\chi_1 = 2g(g^2 - \Delta_L'\Delta_R' + \gamma^2). \tag{4.61}$$

With a different polynomial in Equation 4.47 for each set of fixed points, one must apply the Routh-Hurwitz analysis to each set in turn (or each branch of the curve). For a stable set of fixed points, the polynomial in Equation 4.47 has 6 solutions, each with a negative real part, so that $\vec{v}(t)$ decays with time.

The first condition of the Routh-Hurwitz criterion requires the coefficients a_n (where $0 \leq n \leq 6$) be the same sign. This is satisfied when $\eta_d > 0$, where η_d is defined

$$\eta_d = 1 - \frac{\lambda^2\left(2\chi_L|\alpha_L|^2 + 2\chi_R|\alpha_R|^2 - \chi_1 g(\alpha_L^*\alpha_R + \alpha_R^*\alpha_L)\right)}{\omega_m\epsilon}. \tag{4.62}$$

This is the bistability parameter for the system, which falls in the range $0 < \eta_d < 1$, for the red detuned regime ($\Delta_L', \Delta_R' > 0$), when the fixed point solution is stable.

The second condition requires that the first column of the Routh Array (see Appendix E) contains no sign changes between elements. Whereas in the single mode case it is found that $0 < \eta_s < 1$ is sufficient to ensure the first and second criteria are satisfied, the two mode case is more complicated. When moving from an eigenvalue equation for a 4×4 matrix to a 6×6 matrix, the eigenvalue analysis rapidly becomes more complicated.

This second condition is examined in Table E.2 of Appendix E. The first column contains six elements, labelled a_6, a_5, b_1, c_1, d_1, e_1 and f_1. Equation 4.48 shows $a_6 > 0$, and it is simple to show that $f_1 = a_0$. Full expressions for elements b_1, c_1, d_1 and e_1 are cumbersome, and not very illuminating, thus will be omitted from this thesis. Suffice to say, whilst $b_1 > 0$ for the red

detuned regime, it cannot be guaranteed via analytic expressions that the rest are positive when $0 < \eta_d < 1$, $\Delta'_L, \Delta'_R > 0$. That said, numerical evaluation of these elements over a range of parameters suggests they are indeed positive for the conditions mentioned, suggesting $0 < \eta_d < 1$ as the sole condition on stability. However, a full analytic proof of this remains to be found.

Figure 4.6a shows the bistability parameter, η_d, for the fixed point solutions plotted in Figure 4.3a. The graph comprises three branches, where $\eta_d < 0$ corresponds to the unstable branch, shown by a dashed line. Applying the remainder of the Routh Hurwitz criteria confirms that the two branches where $\eta_d > 0$ satisfy the stability criteria, up until $\eta_d = 1$, where the system transitions to a limit cycle. These results are consistent with the results deduced from the potential $V(q)$. As Figure 4.2 shows, the positions of minima in the potential correspond to cases where $0 < \eta_d < 1$, whilst the maximum corresponds to $\eta_d < 0$. The Routh Hurwitz analysis, however, is more systematic and allows the behaviour of the fixed points to be observed more clearly as parameters are varied.

(a) $\qquad\qquad$ (b)
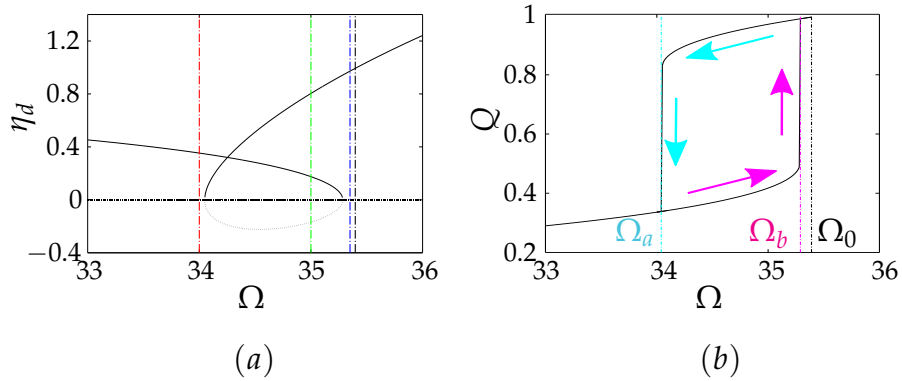
Figure 4.6: For solutions shown in Figure 4.3a, stability is demonstrated via (a) the stability parameter, η_d, defined in Equation 4.62, and (b) a hysteresis curve, showing the fixed points reached as the driving strength is swept up and down, as indicated by arrows along the separate branches. The vertical dotted lines in (a) mark Ω values which produce the potentials in corresponding colours in Figure 4.2, as well as the onset of instability at Ω_0 (in black). In (b), the instability is marked alongside Ω_a (cyan) and Ω_b (magenta) which mark the points where the systems switches between fixed points as the drive strength is reduced and increased, respectively.

With varying laser power, hysteresis is observed in the bistable system. This is illustrated in Figure 4.6b, which shows the fixed points reached via numerically plotted trajectories in $q(t)$. As the driving strength increases, the system moves along the lower branch of the curve in Figure 4.3a, right up until this branch becomes unstable at Ω_b. At this point, the fluctuations become large and the fixed point ceases to be stable. One then observes a discontinuous transition (vertical line in Figure 4.6b) to the upper branch. Sweeping the driving strength down, however, causes the system to follow the upper branch until this solution becomes unstable at Ω_a.

The switching between branches of the curve is expected to be accompanied by large fluctuations in the resonator[35, 69], as such the presence of the bistability interferes with the process of cooling the resonator. One must therefore be sure to confine the system to a regime where a single fixed point is present.

In this example, the mechanical potential provides an accurate picture of the fixed point dynamics. The two stable branches of Figure 4.3a are identified as minima in the potentials plotted in Figure 4.2. This may not, in general, be the case. Parameters selected in this section put the system in a regime where losses are small, yet since $\omega_m < \kappa$, the time delay in the cavity's response is also small, so that the picture offered via the effective Hamiltonian is sufficient to determine the stability of fixed points. In general, however one needs to account for the full dynamics of the system in order to obtain an accurate picture[47, 49].

In addition to the effective potential description, Figure 4.3b shows that the effective frequency shift $\delta\omega$ provides a useful tool in determining that the system is in a regime where static bistabilities are absent. When $|\delta\omega| \ll \omega_m$, one can be confident that the fixed point state will remain stable with small variations in Ω[49]. A calculation of $\delta\omega$ is presented in Section 4.4.1 below.

4.4   LINEARIZED CALCULATION

Having explored the presence of static bistabilities in the system, analysis now focuses on the regime where there is a single stable fixed point. The fluctuations in the system about the fixed point are analysed in order to determine the extent to which the cavity can be said to cool the resonator. The starting point is Equations 4.16 to 4.19, which describe the linearized

dynamics[16] of the system with small fluctuations about its mean field values.

The calculation proceeds by solving the system of Equations (4.16 to 4.19) to obtain the spectrum of the resonator's position fluctuations. By comparing this spectrum with that of a damped harmonic oscillator in thermal equilibrium, with a bath at a given temperature T, an effective frequency, damping rate and temperature can be deduced for a resonator coupled to a two mode cavity system. The following analysis focuses on the back action of the cavity on the resonator, as such the effects of the thermal bath are ignored, and the damping, γ, and thermal fluctuations, ζ, are dropped in Equations 4.16 and 4.17.

The symmetrised spectrum of position fluctuations is defined as

$$S_q(\omega) = \frac{1}{2\pi} \int_{-\infty}^{\infty} dt e^{-i\omega t} \left[\langle \delta q(t)\delta q(0) \rangle + \langle \delta q(0)\delta q(t) \rangle \right]. \quad (4.63)$$

For an oscillator with frequency ω_0, damped at a rate γ which is in contact with a bath at temperature T, it is known that[71]

$$S_q(\omega) = \frac{1}{2\pi} \frac{(2\bar{n}+1)\omega\omega_m\gamma}{(\omega^2 - \omega_m^2)^2 + \gamma^2\omega^2}, \quad (4.64)$$

where $\bar{n} = [e^{\frac{\omega}{k_B T}} - 1]^{-1}$. For a weakly damped system ($\gamma \ll \omega_m$) $S_q(\omega)$ is strongly peaked about $\omega = \omega_m$ and the thermal occupation can be approximated as $\bar{n} = [e^{\omega_m/k_B T} - 1]^{-1}$. Noting that $\langle \delta q^2 \rangle = \bar{n} + \frac{1}{2}$, the spectrum can be written

$$S_q(\omega) \approx \frac{1}{2\pi} \frac{2\omega_m^2 \langle \delta q^2 \rangle \gamma}{(\omega^2 - \omega_m^2)^2 + \gamma^2\omega^2}. \quad (4.65)$$

The denominator in Equation 4.65 can be written as

$$|dw_q|^2 = |\omega^2 - \omega_m^2 + i\gamma\omega|^2. \quad (4.66)$$

4.4.1 *Effective damping of the mechanical mode*

Analysis of the mechanical fluctuations proceeds by Fourier transforming Equations 4.16 to 4.19

$$\delta q(\omega) = \frac{\omega_m \lambda}{\omega^2 - \omega_m^2} \Big[\alpha_R^* \delta a_R(\omega) + \alpha_R \delta a_R^\dagger(\omega) - \alpha_L^* \delta a_L(\omega)$$
$$-\alpha_L \delta a_R^\dagger(\omega) \Big] \tag{4.67}$$

$$\delta p(\omega) = \frac{i\omega}{\omega_m} \delta q(\omega) \tag{4.68}$$

$$\delta a_L(\omega) = [h_L(\omega)]^{-1} \Big[i\lambda \alpha_L \delta q(\omega) - ig\delta a_R(\omega) + \sqrt{\kappa} a_L^{IN} \Big] \tag{4.69}$$

$$\delta a_R(\omega) = [h_R(\omega)]^{-1} \Big[-i\lambda \alpha_R \delta q(\omega) - ig\delta a_L(\omega) + \sqrt{\kappa} a_R^{IN} \Big] \tag{4.70}$$

where

$$h_{L(R)} = \frac{\kappa}{2} + i\left(\omega + \Delta'_{L(R)}\right). \tag{4.71}$$

Some rearranging decouples equations 4.67 to 4.70, giving an expression for $\delta q(\omega)$ of the form

$$\delta q(\omega) = \frac{\omega_m \lambda}{A'(\omega)} \Big[D_1(\omega) B_2(\omega) a_L^{IN} + D_2(\omega) B_1(\omega) a_L^{IN\dagger}$$
$$+ E_1(\omega) B_2(\omega) a_R^{IN} + E_2(\omega) B_1(\omega) a_R^{IN\dagger} \Big], \tag{4.72}$$

where the following are defined:

$$B_1(\omega) = h_L(\omega) h_R(\omega) + g^2 \tag{4.73}$$

$$B_2(\omega) = k_L(\omega) k_R(\omega) + g^2 \tag{4.74}$$

$$C_1(\omega) = -i\lambda \left[|\alpha_L|^2 h_R(\omega) + |\alpha_R|^2 h_L(\omega) \right]$$
$$+ g\lambda \left(\alpha_L^* \alpha_R + \alpha_R^* \alpha_L \right) \tag{4.75}$$

$$C_2(\omega) = i\lambda \left[|\alpha_R|^2 k_L(\omega) + |\alpha_L|^2 k_R(\omega) \right]$$
$$+ g\lambda \left(\alpha_R \alpha_L^* + \alpha_L \alpha_R^* \right) \tag{4.76}$$

$$D_1(\omega) = \left[ig\alpha_R^* + \alpha_L^* h_R(\omega) \right] \sqrt{\kappa} \tag{4.77}$$

$$D_2(\omega) = \left[-ig\alpha_R + \alpha_L k_R(\omega) \right] \sqrt{\kappa} \tag{4.78}$$

$$E_1(\omega) = -\left[\alpha_R^* h_L(\omega) + ig\alpha_L^* \right] \sqrt{\kappa} \tag{4.79}$$

$$E_2(\omega) = -\left[\alpha_R k_L(\omega) - ig\alpha_L \right] \sqrt{\kappa} \tag{4.80}$$

$$A(\omega) = \left(\omega^2 - \omega_m^2 \right) H(\omega) K(\omega) \tag{4.81}$$

$$A'(\omega) = \frac{\omega_m \lambda}{-\omega_m \lambda \left[C_1(\omega) B_2(\omega) + C_2(\omega) B_1(\omega) \right] + A(\omega)} \tag{4.82}$$

where

$$k_{L(R)} = \frac{\kappa}{2} + i\left(\omega - \Delta'_{L(R)}\right). \tag{4.83}$$

The two point correlator $\langle \delta q(\omega) \delta q(\omega') \rangle$ is then a sum of combinations of $a^{IN}_{L(R)}$ and $a^{IN\dagger}_{L(R)}$, of which Equations 4.8 and 4.9 give the only non-zero contributions. The only non-zero correlators follow from Equations 4.8 and 4.9:

$$\langle a^{IN}_{L(R)}(\omega) a^{IN\dagger}_{L(R)}(\omega') \rangle = \frac{1}{2\pi}\delta(\omega + \omega'). \tag{4.84}$$

Picking out the two non-zero contributions, the 2 point correlator, $\langle \delta q(\omega) \delta q(\omega') \rangle$ is given by

$$\langle \delta q(\omega) \delta q(\omega') \rangle = \frac{A'(\omega)A'(\omega')}{2\pi}\bigg[D_1(\omega)D_2(\omega')B_2(\omega)B_1(\omega')$$

$$+E_1(\omega)E_2(\omega')B_2(\omega)B_1(\omega')\bigg]\delta(\omega + \omega'). \tag{4.85}$$

The spectrum is then found via Equation 4.63, where integrating over the delta functions amounts to setting $\omega' = -\omega$. Analysis of the expressions given in Equations 4.73 to 4.82 reveals $B_1(-\omega) = B_1^*(\omega)$, and so on for each expression. This allows the spectrum to be written as

$$S_q(\omega) = \frac{(\omega_m\lambda)^2}{2\pi|dw(\omega)|^2}\left[F_1(\omega) + F_2(\omega)\right], \tag{4.86}$$

where the following are defined:

$$F_{1(2)} = \frac{|D_{1(2)}(\omega)|^2 + |E_{1(2)}(\omega)|^2}{|B_{1(2)}(\omega)|^2} \tag{4.87}$$

$$dw(\omega) = \omega^2 - \omega_m^2 + \chi(\omega), \tag{4.88}$$

and

$$\chi(\omega) = \omega_m\lambda\left[\frac{C_1(\omega)}{B_1(\omega)} + \frac{C_2(\omega)}{B_2(\omega)}\right]. \tag{4.89}$$

A direct comparison can be made between $dw(\omega)$ and the denominator in Equation 4.65. This allows an 'effective' damping and frequency shift to be deduced, in analogy with the case of the standard damped oscillator by identification

$$|dw(\omega)|^2 = |\omega^2 - \omega_m^2 + i\gamma_{eff}\omega|^2. \tag{4.90}$$

The effective damping is therefore identified by extracting the imaginary component of $\chi(\omega)$,

$$\gamma_{eff}(\omega) \quad = \quad \frac{\omega_m \lambda}{\omega} \Im \left[\frac{C_2}{B_2} + \frac{C_1}{B_1} \right]. \qquad (4.91)$$

With this expression in terms of ω, the approximation of a weakly damped system is applied. Equation 4.65 was written with the assumption that the spectrum is strongly peaked around ω_m. This same assumption allows the approximation $\omega = \omega_m$ to be used to calculate a fixed value of γ_{eff}:

$$\gamma_{eff}(\omega) \quad = \quad \lambda \Im \left[\frac{C_2(\omega_m)}{B_2(\omega_m)} + \frac{C_1(\omega_m)}{B_1(\omega_m)} \right]. \qquad (4.92)$$

In general, however, there is a small frequency shift, so that the spectrum is actually peaked about a value ω_{eff}, which relates to the mechanical frequency by $\omega_{eff} = \omega_m + \delta\omega$, where $\delta\omega$ is a small frequency shift. The frequency ω_{eff} can be identified as the square root of the real component of $\chi(\omega_m)$ - taking the frequency as ω_m to make an initial calculation, which provides a reasonable approximation when the shift is small, $\delta\omega \ll \omega_m$:

$$\omega_{eff}^2 \quad = \quad \omega_m^2 + \lambda \Re \left[\frac{C_2(\omega_m)}{B_2(\omega_m)} + \frac{C_1(\omega_m)}{B_1(\omega_m)} \right]. \qquad (4.93)$$

Given that $\delta\omega \ll \omega_m$, the frequency shift can be approximated

$$\omega_{eff}(\omega) \quad \approx \quad \omega_m + \frac{\lambda}{2} \Re \left[\frac{C_1}{B_1} + \frac{C_2}{B_2} \right], \qquad (4.94)$$

$$\delta\omega(\omega) \quad \approx \quad \frac{\lambda}{2} \Re \left[\frac{C_1}{B_1} + \frac{C_2}{B_2} \right]. \qquad (4.95)$$

With regards to Equations 4.92 and 4.95, recall the assumption of small fluctuations, which is required to linearize the equations. The result is expressions for γ_{eff} and $\delta\omega$ which apply in the regime where the fixed point is stable. This allows the regime of cooling to be investigated with these expressions. One might also expect these expressions to accurately predict the onset of instability. This will be addressed in the next chapter. In the regime of limit cycles, amplitude dependent expressions are expected, as in Chapters 2 and 3.

In the limit $g \to 0$, Equation 4.92 matches the case of a single linearly coupled mode, for small energy (see Equation 2.76 of Chapter 2). This is the linearized single mode result achieved via a similar process by Genes et. al.[35].

4.4.1.1   *Numerical analysis*

The effective damping is investigated by varying two parameters: the laser detuning, Δ, and the frequency shift arising from the equilibrium displacement of the resonator, $\Delta\omega$. These two parameters navigate the dispersion diagram of Figure 4.1, bringing the system into resonance with the various modes shown. This determines the interplay between optical and mechanical modes. Colour plots in figures 4.7a and 4.7c show the behaviour of γ_{eff} under different circumstances of note. There are two distinct scenarios to consider, in terms of parameters chosen:

- $\omega_m < 2g$ - interactions between quadratic modes are weak and the energy gap is too large for transitions between modes. The behaviour of the system is similar to that of the single mode case.

- $\omega_m > 2g$ - interactions between quadratic modes are strong and there exists a value of $\Delta\omega$ where the energy gap between modes matches the mechanical frequency, so that transitions between upper and lower bands are stimulated by the absorption or emission of a phonon.

The optical modes are displayed as white dashed lines alongside the damping, to illustrate how the proximity to optical resonances affects the resonator motion. Also shown are the modes shifted by the mechanical frequency.

The effective damping for the case where $\omega_m < 2g$ is shown in Figure 4.7a. The resonator is most strongly driven and damped when the cavity is driven close to the quadratic mode frequencies, resulting in features along the quadratic dispersion curves. Strong anti-damping (negative values for the effective damping) occurs when the cavity is driven just above an optical frequency, whilst strong damping occurs just below. Since the left mode is driven directly by radiation, the features are stronger when the dispersion curve (frequencies $\omega_{1,2}$) approaches the driven mode (frequency ω_L). This occurs along lines where the mode frequencies coincide with $-\Delta = \Delta\omega$.

Figure 4.7c shows the damping for a small energy gap, $\omega_m > 2g$. The dispersion curves and sidebands, shown in white, illustrate where the Stokes and anti-Stokes resonances occur[49, 16]. The form of the graph is distinctly different to Figure 4.7a; features do not lie along the entirety of the dispersion curves but are confined to regions where the curves cross. Here the

system moves between optical modes by exchanging mechanical quanta: $\omega_m = \omega_1 - \omega_2$. The energy exchange is stronger near the driven mode. The result is a graph with features at A - where emission from the cavity causes driving ($\gamma_{eff} < 0$) - and B - where the cavity absorbs energy, causing damping ($\gamma_{eff} > 0$).
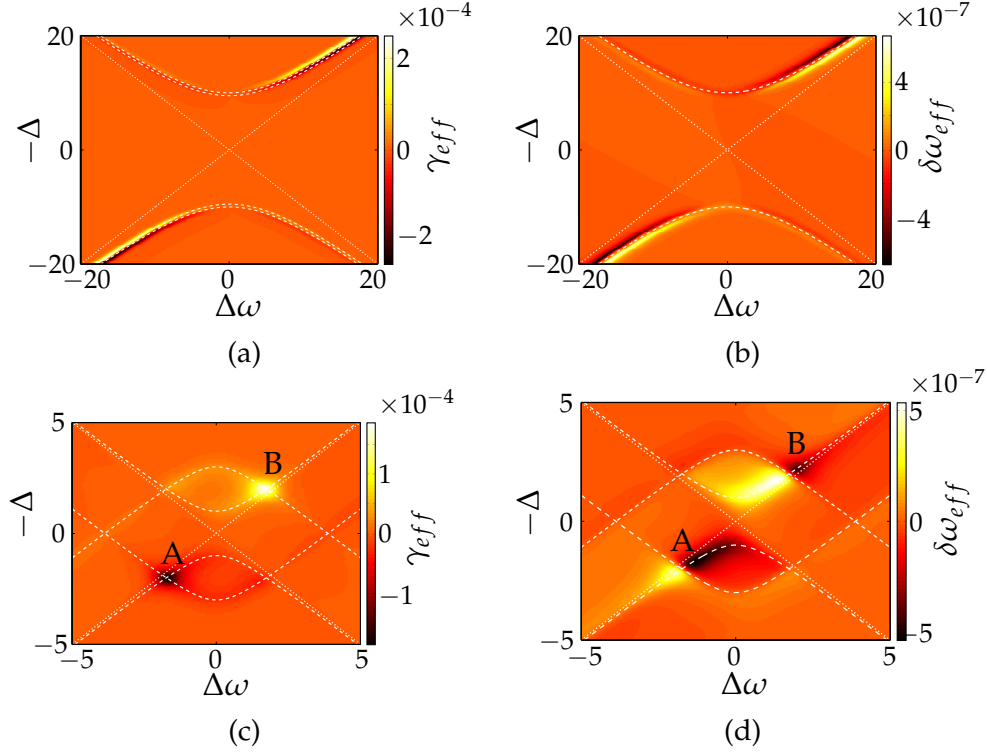
Figure 4.7: Effective damping and frequency shift in the resonator, with respect to Δ and $\Delta\omega$, for two different regimes: (a) and (b) show γ_{eff} and $\delta\omega$ for $g = 10$ and $\omega_m = 0.5$, where the energy gap between the photon modes is large, and so driving and damping occur when the cavity is driven just above or below the quadratic modes. Figures (c) and (d) show γ_{eff} and $\delta\omega$ for $g = 1$, $\omega_m = 4$, where a small energy gap results strong interactions at $\omega_m = 2\sqrt{g^2 + \Delta\omega^2}$, allowing transitions between photon modes. The remaining parameters are $\Omega = 1$ and $\lambda = 10^{-2}$ in both cases.

Figures 4.7d and 4.7b show the frequency shift in the resonator, deduced in Equation 4.95. Since the shift doesn't become any larger than $\Delta\omega \sim 10^{-4}$, the resonator dynamics lies well within the range $\Delta\omega \ll \omega_m$, so that the static bistability is unlikely to cause an issue.

4.4.2 *Thermal phonon number*

In Chapter 2, sideband cooling was investigated for a single linear mode. In the regime of low energies, the phonon number was deduced via the probability distribution. It was found to take the form[13, 31]

$$n_{eff} = \frac{\gamma \bar{n} + \gamma_{BA} n_{BA}}{\gamma + \gamma_{BA}}, \qquad (4.96)$$

where n_{BA} was deduced from the diffusion, $D_{BA} = \gamma_{BA}(n_{BA} + \frac{1}{2})$. Something similar happens in the two mode case considered here. However, as the focus of this section is on the ultimate limit of cooling, which is set by n_{BA} in the limit $\gamma \ll \gamma_{eff}$, the quantity n_{BA} is explored, rather than n_{eff}.

Once the effective damping has been defined (given in Equation 4.92), the comparison of $S_q(\omega)$ (given by Equation 4.86) with the thermal result (given in Equation 4.65) can be completed by identifying

$$n_{eff} = 2\pi S_q(\omega) \frac{|\omega_m^2 - \omega^2 - i\gamma_{eff}\omega|^2}{2\omega_m^2 \gamma_{eff}} - \frac{1}{2}. \qquad (4.97)$$

Given Equations 4.86 and 4.92, the resulting expression is

$$n_{eff} = \frac{\lambda}{2} \frac{|B_1|^2 |B_2|^2 (F_1 + F_2)}{|B_2|^2 \Im[C_1 B_1^*] + |B_1|^2 \Im[C_2 B_2^*]} - \frac{1}{2}. \qquad (4.98)$$

In the limit that $g \to 0$, at small energy, the expression from Equation 2.79 of Chapter 2 is recovered:

$$n_{BA} = \frac{\frac{\kappa^2}{4} + (\omega_m - \Delta_L)^2}{4\omega_m \Delta_L}, \qquad (4.99)$$

which matches the known result for a single cavity mode, with linear coupling[13]. Equations 4.99 and 4.92 offer a basis of comparison between the lowest achievable phonon numbers when considering cooling for the single and double mode systems. For the single mode system, n_{BA} is minimised when $\Delta_L = \sqrt{\omega_m^2 + \kappa^2/4}$. Recall from Chapter 2 Section 2.3.6, one can deduce a limit in the case of resolved sideband cooling ($\Delta \approx \omega_m$, in the limit $\kappa \ll \omega_m$):

$$n_{BA} = \left(\frac{\kappa}{4\omega_m}\right)^2. \qquad (4.100)$$

For the two mode case, analysis is not so simple, as energy is exchanged between optical modes as well as with the resonator. The complicated expression of Equation 4.98 is therefore analysed numerically.

4.4.2.1 *Numerical analysis*

In the interest of obtaining as low a phonon number as possible, analysis focuses on cooling in the resolved sideband limit, where the anti-Stokes process[49] is dominant. This occurs when the following condition is met:

$$\Delta \;=\; \omega_m - \sqrt{g^2 + \Delta\omega^2}. \tag{4.101}$$

This means that the drive frequency is offset from the upper optical mode by a factor of the mechanical frequency, so that the absorption of a phonon puts photons in resonance with the cavity. Figures 4.7c and 4.7a show heavy damping occurring along such sidebands. It is found numerically that the minimum phonon number, n_{min}, does indeed occur when this condition is approximately met. Figure 4.8 verifies this result; as g is varied, the values of Δ and $\Delta\omega$ which produce a minimum in n_{BA} are recorded. With the left and right hand side of equation 4.101 plotted for varying g, a straight line with a gradient of unity is obtained.
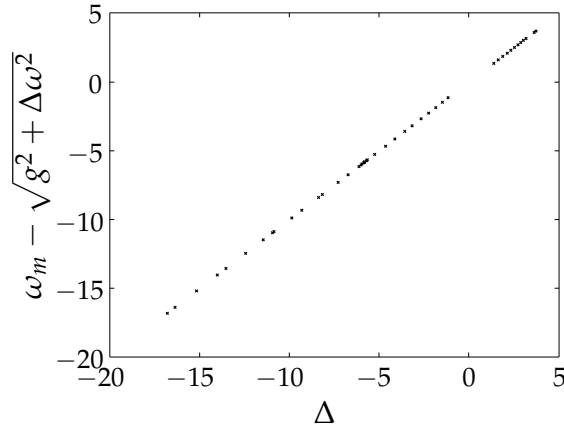
Figure 4.8: Plot verifying that the minimum phonon number is achieved when cooling at the sidebands, such that Equation 4.101 is satisfied. The coupling g is varied, and the values of Δ and $\Delta\omega$ which produce a minimum if n_{BA} are recorded and plotted such that a straight line is obtained.

Having established where to seek the lowest values of n_{BA}, it is interesting to make a comparison between the case of single mode ($g = 0$) and double mode ($g \neq 0$) coupling. This essentially gives a comparison between the minimum temperature achievable via the reflective and dispersive setups in an optomechanical system. The central question posed by this chapter is

whether or not it is possible to achieve temperatures as low as in the reflective case by using the dispersive system, which offers a much simpler method of fabrication. The parameter N_{min} is therefore defined, for use within this section:

$$N_{min}(g) = \frac{n_{min}(g)}{n_{min}(g=0)}. \tag{4.102}$$

The minimum achievable phonon number is investigated for varying tunnelling rate, g. Equation 4.100 suggests that increasing ω_m will reduce the minimum phonon number for the single mode case, so that cooling is more effective in the resolved sideband limit[13]. Figure 4.9 verifies this, showing that $n_{BA} \ll 1$ as the resolved sideband limit is approached, for $\Omega = 1$, $\lambda = 10^{-2}$, $\kappa = 1$.
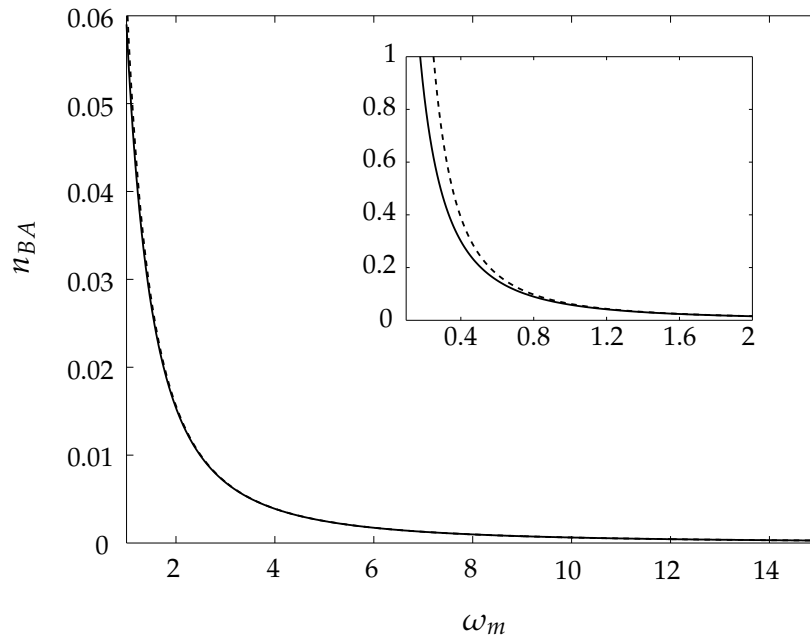
Figure 4.9: Minimum effective phonon number for the single mode case (solid) for varying ω_m, plotted alongside Equation 4.100 (dashed). The inset shows where the curves begin to diverge in the bad cavity limit. At each value of ω_m, n_{BA} is calculated for $\Delta = \sqrt{\omega_m^2 + \kappa^2/4}$. The remaining parameters are $\Omega = 1$, $\lambda = 10^{-2}$, $\kappa = 1$.

Turning to the case where $g \neq 0$, Figure 4.10 shows the quantity N_m for the resolved sideband regime, as g is varied. The ratio generally remains close to 1, with the exception of a peak which occurs in the vicinity of $\omega_m = g$, increasing in magnitude as ω_m and g increase.

As g is increased along lines of constant ω_m, the value of N_m tends to peak before decreasing rapidly (see Figure 4.11, which shows cross sections through Figure 4.10). The height of the peaks in the ratio N_m increase as ω_m is increased, though as in the single mode case (Figure 4.9), the value of n_{BA} generally decreases with ω_m far from the peak. The white contours in Figure 4.10 mark regions where $N_m < 1.001$. Whilst the larger of these regions occurs as $g \to 0$, the region marked X shows where tunnelling rates close to the mechanical frequency produce $N_m < 1.001$. This implies that, by choosing the tunnelling rate and mechanical frequency carefully, one may observe phonon numbers as small as in the single mode case.
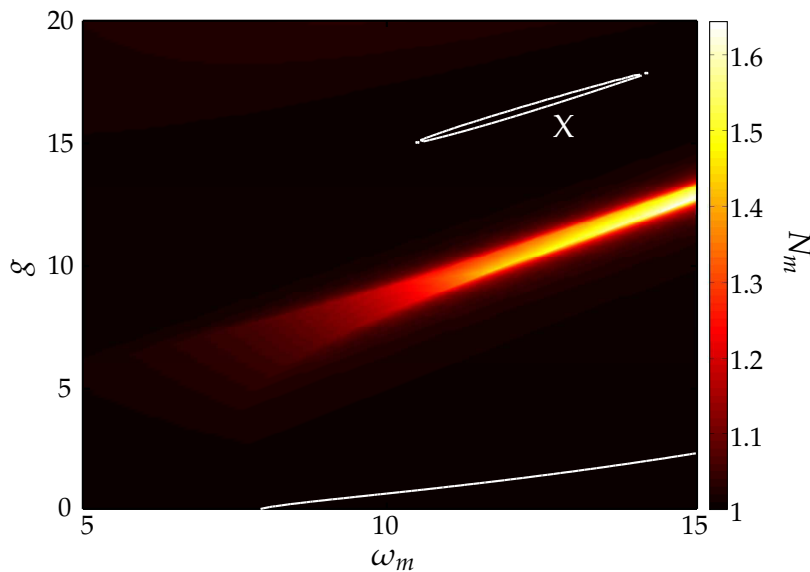
Figure 4.10: Analysis of the ratio N_m as ω_m and g are varied. Contours of $N_m = 10^{-3}$ are shown in white. For the majority of parameters the ratio is close to unity, but a large peak in sees cooling significantly reduced for $g \neq 0$.

It is worth noting that this analysis applies in the case where the system is weakly coupled, such that $\gamma_{eff} \ll \kappa$. Increasingly, experiments in optomechanics have made the strong coupling regime accessible[44, 66, 72]. Analysis on the single mode system, in the strong coupling regime, finds cooling to be less efficient than in the weak coupling case[13, 34].

4.5   CONCLUSIONS

This chapter has explored interactions between the mechanical element and two optical modes, with the interest of draw-
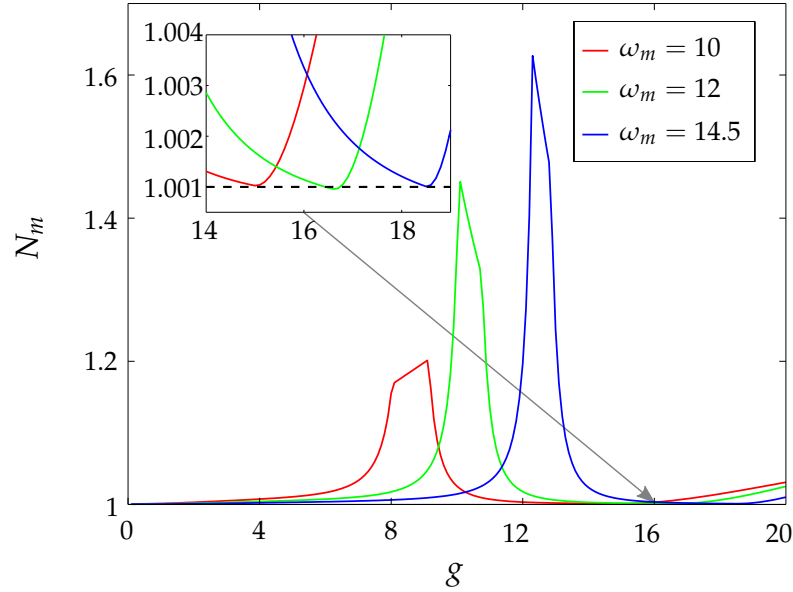
Figure 4.11: Cross sections through Figure 4.10, at constant ω_m for $\omega_m = 10$, $\omega_m = 12$ and $\omega_m = 14.5$. The line for $\omega_m = 12$ passes through the contour at X in Figure 4.10, so that a minimum is reached where $N_m < 1.001$.

ing comparison to the case where a single optical mode was present. In particular, this chapter focused on the feat of cooling a system to its quantum ground state, and whether such an achievement would be possible for the dispersive optomechanical system.

By decreasing the tunnelling rate through the membrane, a different scenario was observed where the optical modes interacted with one another[16]. The system was described by a similar Hamiltonian to the previous chapter, and equations of motion formulated from input-output theory. Since only the cooling regime was considered, analytical expressions were produced by linearizing the equations of motion. This allowed an effective optomechanical damping and frequency shift to be deduced by calculating the noise spectrum[71].

As the laser detuning was varied, the regions of strongest driving and damping were found at sidebands, where phonons were transferred between optical and mechanical modes. This identified a regime where cooling was expected to be most efficient. In order to ensure the lowest phonon number could be achieved, care was taken to avoid the static bistability - the presence of which was indicated by sudden drops in the effective frequency of the mechanical mode.

Cooling was investigated by deducing the effective phonon number via the mechanical noise spectrum. By varying the tunnelling rate, the efficiency of cooling was compared between single and double mode systems. It was found that there existed combinations of $g \neq 0$ and ω_m which produce effective phonon numbers within 0.1% of the lowest achievable phonon number, in the single mode case. The conclusion drawn is that allowing radiation to pass through the membrane can produce cooling effects as efficient in the red detuned regime. This provides a possible method of cooling an oscillator to its quantum ground state, whilst overcoming the issue of fabricating highly reflective elements with a high mechanical quality factor[17].

5

TWO MODE DYNAMICS: FROM LIMIT CYCLES TO CHAOS

5.1 INTRODUCTION

Previously, the driven non-linear regime has been explored for systems where single optical modes are coupled linearly and quadratically to the mechanical mode. In these cases, the non-linear dynamics and quantum fluctuations have been explored with a combination of numerical and analytic calculations. Further to this, Chapter 4 explored the linear dynamics of the system when two optical modes were present, in the red detuned regime. This chapter progresses by exploring the two optical mode system for the case of blue detuning. However, the presence of three harmonic oscillators results in a more complex system, and analysis for this system is more difficult than for those studied in Chapters 2 and 3.

Owing to the complexity of the two optical mode system, analysis of this chapter focuses on the average dynamics of the system. This is made possible by exploring the regime of strong driving, where the system is driven to large amplitude oscillations, and fluctuations become less important. The dynamics of the resulting limit cycles will be explored, as well as the transition to chaos. Numerical analysis explores the trajectory of variables characterising the system, comparing the long time behaviour as the mechanical coupling is swept. An analytical calculation is presented in the form of a rotating wave approximation on the photon mode equations, allowing a description of the limit cycle dynamics.

This chapter is organised as follows. In section 5.2 the two mode driven system is introduced, and the equations of motion deduced. Section 5.3 presents a numerical analysis of the equations, first addressing the case where the drive is provided by a thermal bath, before exploring the case where the system is driven by a laser source. The dynamics are mapped out over the blue detuned range. Section 5.4 presents an analytical calculation of the limit cycle amplitudes in the regime where periodic oscillations occur, for weaker coupling strengths. This is achieved via a rotating wave approximation. The predictions

of the calculation are compared to numerical results in Section 5.4.6, and conclusions drawn in Section 5.5.

5.2   THE SYSTEM

This chapter deals with the dispersive system introduced in Chapter 3, where optical modes a_L and a_R are coupled to the mechanical membrane at position $q(t)$[17, 18]. A schematic diagram of the system is shown in Figure 5.1a. As in Chapter 4, the tunnelling rate through the membrane, g, is assumed to be small enough in comparison to the mechanical frequency to allow phonon mediated transitions between optical modes[16]. This is illustrated by the grey arrow in the dispersion diagram of Figure 5.1b, indicating where a displacement q_0 creates a situation where $\omega_1 - \omega_2 = n\omega_m$.

The regime of blue detuning is investigated, over a range of parameters which induce limit cycles in the resonator. Figure 5.1a shows a resonator mounted at an equilibrium position, q', with respect to the cavity centre. This causes an equilibrium detuning $2\Delta\omega$ between the cavity modes, where the quantity $\Delta\omega = \lambda q'$ is shown in green in Figure 5.1b. As the cavity is driven by laser radiation, the resonator is driven into oscillations about point q_0 (measured from the centre, where $q_0 = q' + Q$ and marked in red). These oscillations result in a time dependence for the optical modes,

$$\omega_L = \omega_0 - \lambda q(t) \tag{5.1}$$
$$\omega_R = \omega_0 + \lambda q(t). \tag{5.2}$$

A drive of frequency ω_d is applied to the left mode, a_L, such that the detuning $\Delta = \omega_0 - \omega_d$ is negative. The effective Hamiltonian takes the same form as in Chapter 4:

$$\begin{aligned} H_{eff} = {} & \frac{1}{2}\omega_m \left(p^2 + q^2 \right) + \Delta'_L(q)a_L^\dagger a_L + \Delta'_R(q)a_R^\dagger a_R \\ & + g \left(a_L^\dagger a_R + a_R^\dagger a_L \right) + \Omega \left(a_L + a_L^\dagger \right), \end{aligned} \tag{5.3}$$

where λ is the optomechanical coupling strength, ω_m the mechanical frequency and the strength of the drive is parametrised by Ω. The detunings of the cavity modes are given by

$$\Delta'_L(q) = \Delta - \lambda q(t) \tag{5.4}$$
$$\Delta'_R(q) = \Delta + \lambda q(t). \tag{5.5}$$
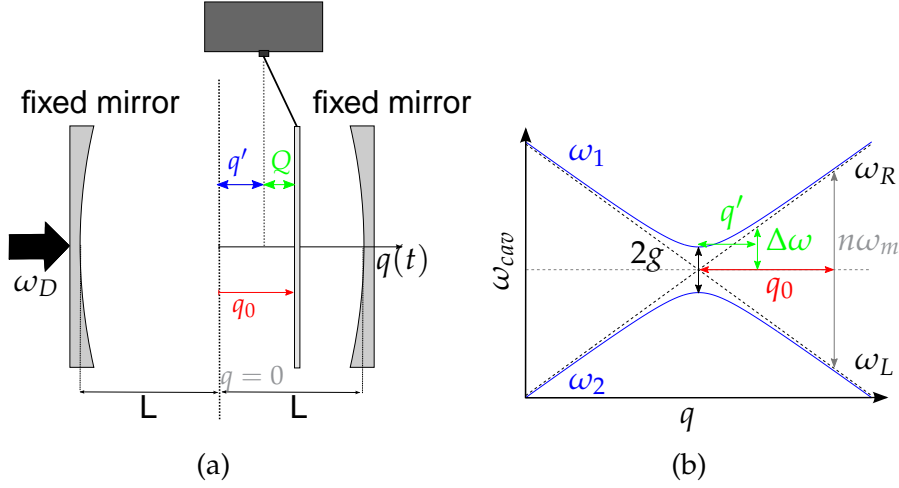
Figure 5.1: The system, represented by (a) schematic and (b) the dispersion diagram. The displacement $q(t)$ of the membrane is measured relative to the centre of the cavity. The equilibrium position of the resonator is set by the position at which it is clamped, at $q = q'$. When the cavity is driven at frequency ω_d the membrane is made to oscillate around a point $q_0 = q' + Q$, where Q is the fixed point. When $2g < \omega_m$ there exists a value of q_0 such that the optical modes are separated by an integer multiple of the mechanical frequency, so that transitions between the modes occur with exchange of phonons in the resonator.

The master equation for the system takes the same form as in previous chapters:

$$\frac{d\rho}{dt} = -i\left[H_{eff}, \rho\right] + \hat{\mathcal{L}}_{tot}, \tag{5.6}$$

where the dissipation is described by $\mathcal{L}_{tot} = \hat{\mathcal{L}}_b + \hat{\mathcal{L}}_L + \hat{\mathcal{L}}_R$:

$$\hat{\mathcal{L}}_b = -\frac{\gamma}{2}\left(b^\dagger b\rho + \rho b^\dagger b - 2b\rho b^\dagger\right) \tag{5.7}$$

$$\hat{\mathcal{L}}_{L(R)} = -\frac{\kappa}{2}\left(a^\dagger_{L(R)}a_{L(R)}\rho + \rho a^\dagger_{L(R)}a_{L(R)} - 2a^\dagger_{L(R)}\rho a_{L(R)}\right), \tag{5.8}$$

where it is assumed that the entire system is at $T = 0$, and the damping constant κ describes dissipation of the cavity modes, whilst the damping constant γ applies to the mechanical mode.

5.2.1 Equations of motion for the system

The semi classical dynamics of the system can be determined from equations of motion for the expectation values of cavity amplitudes and mechanical coordinates by tracing over the

master equation (Equation 5.6)[1] - For example, the average occupation of the left cavity mode, $\langle a_L \rangle = \alpha_L$ obeys the equation

$$\dot{\alpha_L} = \text{Tr}\left[a_L \dot{\rho}\right] \tag{5.9}$$
$$= -\left[i\Delta'_L(q) + \frac{\kappa}{2}\right]\alpha_L - ig\alpha_R - i\Omega. \tag{5.10}$$

Similarly, equations of motion are obtained for the average dynamics of the right cavity, α_R, and membrane co-ordinates:

$$\dot{\alpha_L^*} = \left[i\Delta'_L(q) - \frac{\kappa}{2}\right]\alpha_L^* + ig\alpha_R^* + i\Omega \tag{5.11}$$
$$\dot{\alpha_R} = -\left[i\Delta'_R(q) + \frac{\kappa}{2}\right]\alpha_R - ig\alpha_L \tag{5.12}$$
$$\dot{\alpha_R^*} = \left[i\Delta'_R(q) - \frac{\kappa}{2}\right]\alpha_R^* + ig\alpha_L^*. \tag{5.13}$$
$$\dot{q} = \omega_m p \tag{5.14}$$
$$\dot{p} = -\omega_m q - \gamma p + \lambda(\alpha_L^* \alpha_L - \alpha_R^* \alpha_R), \tag{5.15}$$

where the semi classical approximation $a_L^\dagger a_L = \alpha_L^* \alpha_L$ and $a_R^\dagger a_R = \alpha_R^* \alpha_R$ is made in the last line.

5.3 NUMERICAL ANALYSIS

When the laser drive is blue detuned so that the system is driven, Equations 5.10 to 5.15 lead to a complex non-linear dynamics. Aspects of this dynamics have been described previously in the literature[39, 40, 41, 42], and these approaches are extended in the analysis to follow, starting with a straight forward numerical calculation.

This chapter aims to explore this varied behaviour in the system, in the regime of blue detuning. Equations 5.10 to 5.15 cannot be solved exactly. Instead a numerical approach is taken, using a range of carefully selected parameters that allow one to explore the different behaviours that arise. The coupled equations are solved directly, by numerical integration. The integration is performed using the Adams-Bashforth-Moulton method [73]. This method lends itself well to the system of interest, given the chaotic nature of the dynamics at high coupling. In contrast to single step methods, every data point calculated is dependent on four prior data points. This method allows one to calculate the local truncation error and correct it, improving the accuracy. This is a desirable property for a method dealing with chaotic motion, where small deviations from the initial trajectory grow exponentially with time[9, 49].

The analysis in the rest of this section explores the evolution of the mean field variables as λ is increased in an attempt to map out the full dynamics of the driven system. For varying parameters the system follows a complicated path, before settling into one of 3 different long time behaviours; these are

1. Fixed point - decaying fluctuations,

2. Stable oscillations - limit cycles,

3. Chaos.

Numerical plots are made of the trajectory $x(t)$, where q has been shifted by the equilibrium displacement, so that $x = q - q'$.

5.3.1 *Dynamics in the presence of a thermal bath*

A recent publication investigated this same system numerically [40], in the absence of a laser drive: $\Omega = 0$. Instead a drive is supplied in the form of a heat bath, by assuming the cavity is at a finite temperature. This is described by a finite thermal occupation number n_{th}, which is assumed for the optical cavity. The advantage of this is that the resulting Hamiltonian contains a symmetry which can be exploited, by defining a photon depletion number, y, and photon inversion number, z, in terms of the initial photon number N_0:

$$y = \frac{a_L^\dagger a_L + a_R^\dagger a_R}{N_0} \tag{5.16}$$

$$z = \frac{a_L^\dagger a_L - a_R^\dagger a_R}{N_0}, \tag{5.17}$$

and the phase, ϕ, determined by $\phi = \arg(a_L^\dagger a_R)$. Formulating the system in terms of these operators reduces the number of equations required to describe the corresponding semi-classical dynamics. The equations for the average values now take the form

$$\dot{q} = \omega_m p \tag{5.18}$$

$$\dot{x} = -\omega_m x - \gamma p + \lambda N_0 z \tag{5.19}$$

$$\dot{z} = 2g\sqrt{x^2 - z^2} \sin \phi - \frac{\kappa}{2} z \tag{5.20}$$

$$\dot{\phi} = 2\lambda x - \frac{2gz}{\sqrt{y^2 - z^2}} \cos \phi \tag{5.21}$$

$$\dot{y} = -\frac{\kappa}{2} y + \frac{2\kappa n_{th}}{N_0}, \tag{5.22}$$

instead of Equations 5.10 to 5.15. The first two equations describe a damped harmonic oscillator, driven by the term $\lambda N_0 z$, whilst the next two describe the motion of a pendulum of varying length, with a drive of $2\lambda x$. With numerical analysis of the trajectories, one finds oscillations can only be sustained for the case $\kappa = \gamma = 0$, where the dynamics are chaotic[40].

The presence of a non-zero cavity mode thermal occupation ($n_{th} \neq 0$) acts as an effective drive (instead of the Ω term in Equations 5.10 to 5.15) but this is an unphysical scenario; as explained in Chapter 2, the cavity occupation at room temperature is negligible. In order to generate $n_{th} = 100$, as is used in [40], the cavity would need to be at a significantly higher temperature, whilst maintaining the resonator at zero temperature, which is impractical.

5.3.2 *Driven oscillations*

Here the laser drive is included, and it is assumed that the cavity thermal occupation can be neglected. The drive provides an energy source, allowing for a variety of long time behaviours as the optomechanical coupling is swept. These behaviours will be mapped out, showing how they evolve as a function of the optomechanical coupling, λ. The coupling determines the energy exchange between the optical and mechanical modes, which determines how strongly the resonator is driven. Table 5.1 details the parameters selected to explore the system.

Table 5.1: Parameters for numerical analysis

Parameter	value (units $\kappa = 1$)
ω_m	2
Ω	10
g	0.1
Δ	-1
$\Delta\omega$	1
γ	0.01
$\bar{n}$	0

Varying the coupling takes the system through a series of transitions. Broadly speaking, four different regimes of behaviour can be identified in the resonator, as the coupling is swept. The weak coupling regime is dominated by the fixed point solution. For the parameters of Table 5.1, a single stable fixed point is

present and oscillations about it decay (see Chapter 4 for an analysis of the fixed point solution). At the onset of instability, $\lambda = \lambda_c$, lies a regime of stable limit cycles, where oscillations prevail in the long time limit. These two regimes display long time behaviour that is independent of initial conditions.

The third regime is encountered as λ is increased past a value, λ_{DM}, where dynamical multistability emerges. In this region the long time behaviour is strongly dependent on the initial conditions. There exist a number of attractors for each value of λ, which the system may reach in the long time limit. These include multiple limit cycles, at varying amplitudes, and chaotic trajectories[40, 42]. In addition, one might observe period doubling, where the resonator switches from a series of single period regular oscillations to a pattern of motion which repeats every second oscillation - effectively halving the frequency [42].

Different types of trajectory can be identified by stroboscopic plots of their dynamics, in which points are plotted once per mechanical time period[1]. For a single-period limit cycle, one observes a single dot as a period's oscillation brings the system back to the same point. For period doubling a pair of dots is seen. Figure 5.2 together with Figure 5.3 gives examples of each of each of the behaviours seen in the resonator. In this example, all three types of motion are observed for $\lambda = 0.88$, by varying only the initial conditions $x(0)$ and $p(0)$.

The process of period doubling may occur repeatedly as initial conditions and coupling are altered, so that the frequency halves several times. A final transition at high λ takes the resonator into a regime where oscillations appear chaotic. An example of such a trajectory is given in Figure 5.3.

5.3.2.1 *Fixed point regime*

The radiation pressure force is directly proportional to the optomechanical coupling, therefore at low coupling the energy transferred to the membrane from the external drive via the optical modes is insufficient to overcome losses. Oscillations in the resonator's position therefore decay and it reaches a fixed point state in the long time limit. This range is shown in Figure 5.4a, which compares the Q values deduced from numerics with those found by solving for the fixed point in the weak

---

1 In the stroboscopic plots the shifted mechanical frequency is used - this is the frequency at which the mechanical mode is observed to oscillate, and is within 0.5% of ω_m for both of the diagrams shown.

(a)   (b)
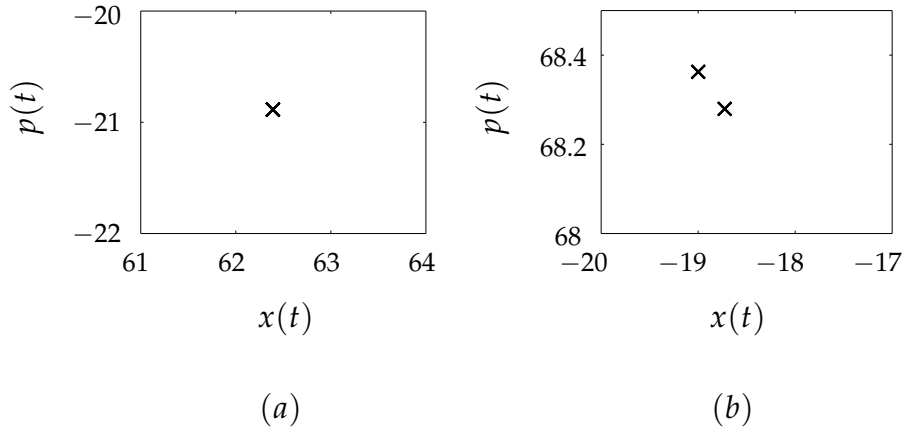
Figure 5.2: Stroboscopic plots for $\lambda = 0.88$, with remaining parameters given in Table 5.1. By specifying different initial conditions, the system reaches different attractors in the long time limit, two examples are shown: (a) a limit cycle, with initial conditions $q(0) = 15$, $p(0) = 65$, (b) period doubling when $x(0) = 5$ and $p(0) = 75$. For both cases, initial values of $a_L(0)$ and $a_R(0)$ are selected by solving for the fixed points, α_L and α_R when $Q = 0$ (see Equations 4.12 and 4.13 of Chapter 4). Each diagram shows the position and momentum plotted every period for 20 periods.
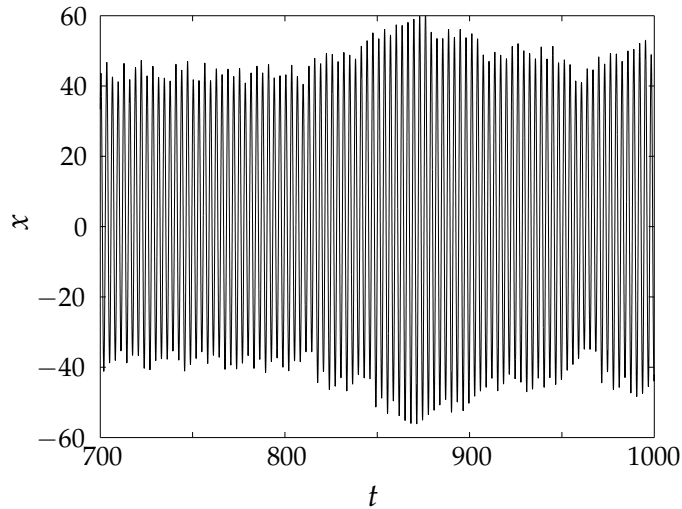
Figure 5.3: Trajectory of $x(t)$ for $\lambda = 0.88$, with initial conditions $x(0) = 5$, $p(0) = 45$. The motion appears to be chaotic and does not settle into periodic oscillations in the long time limit.

coupling regime (see below). The quantity Q is the centre of oscillations measured from the equilibrium displacement, such that $Q = q_0 - q'$.

At weak coupling, Q increases approximately linearly with λ:

$$Q \;=\; \frac{\lambda}{\omega_m}\left(|\alpha_L|^2 - |\alpha_R|^2\right), \qquad (5.23)$$

where α_L and α_R can be approximated by

$$\alpha_L \;\approx\; \frac{-i\Omega\left[\frac{\kappa}{2} + i\Delta_R\right]}{\left[\frac{\kappa}{2} + i\Delta_R\right]\left[\frac{\kappa}{2} + i\Delta_L\right] + g^2} \qquad (5.24)$$

$$\alpha_R \;\approx\; \frac{-g\Omega}{\left[\frac{\kappa}{2} + i\Delta_R\right]\left[\frac{\kappa}{2} + i\Delta_L\right] + g^2}. \qquad (5.25)$$

where Δ_L and Δ_R are taken as Q independent:

$$\Delta_L \;=\; \Delta - \Delta\omega \qquad (5.26)$$

$$\Delta_R \;=\; \Delta + \Delta\omega. \qquad (5.27)$$

Throughout this regime, the short time oscillations occur at approximately the mechanical frequency.

(a)   (b)
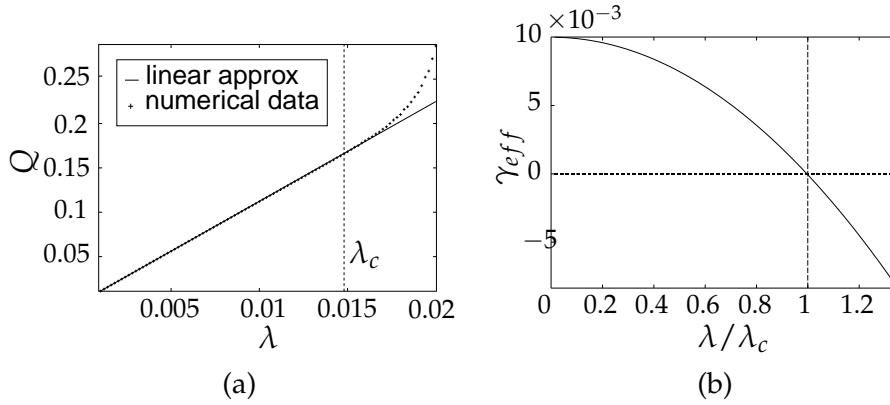
Figure 5.4: Fixed point dynamics (a) in stable regime, where oscillations decay - showing how Q varies with λ and (b) prediction of the instability at $\lambda_c = 0.0148$, using the linearised calculation of Chapter 4. The instability is predicted to occur when $\gamma_{eff} = \gamma + \gamma_{BA} = 0$.

5.3.2.2 *Limit cycle regime*

As the coupling is increased, a value λ_c is approached, where the work done via the radiation pressure force balances the dissipation, and an instability occurs. In terms of the linearized analysis of Chapter 4 this is where the (negative) back action damping matches the intrinsic damping. Here oscillations are sustained, and a limit cycle state becomes stable. At this point

the approximation in Equation 5.23 breaks down (as shown in Figure 5.4a); Q is no longer linear with λ, and represents the centre of stable oscillations. The linearized calculation of Chapter 4 provides an accurate estimate of the onset of limit cycles. This calculation is shown in Figure 5.4b.

Figure 5.5 shows how the limit cycle solutions evolve as λ is increased. The dotted line marks $\lambda_c = 0.0148$, where a smooth transition from fixed point to increasing amplitude oscillations (at approximately ω_m) occurs. The transition is continuous, in that the amplitude, A, increases smoothly from $A = 0$. The curve peaks around $\lambda = 0.024$, showing a smooth, steep incline, before falling asymptotically towards $A = 0$. At $\lambda = 0.12$, dynamical multistability occurs and multiple attractors begin to emerge. Throughout this regime the oscillation frequency remains close to the mechanical frequency.

As the coupling increases, the number of attractors increases. The limit cycle amplitudes follow smooth curves at increasingly higher amplitudes, which fall off asymptotically, never crossing each other. As λ increases, the long time behaviour becomes more sensitive to initial conditions. For a given limit cycle, the range of initial conditions which produce the corresponding trajectory then becomes very narrow.

For $\lambda \geq 0.87$, period doubling and chaos are observed for certain initial conditions. As λ increases, these behaviours occur for a wider range of initial conditions, up to a point where chaos appears to dominate the long time behaviour. The exact value of λ at which the transition to chaotic behaviour occurs has not been found. In order to determine it with any certainty, one would need to map out a series of trajectories with varying initial conditions in the six dimensional parameter space. This is time consuming and it is not possible to ensure all possible limit cycles have been eliminated, as some attractors may only be approached from arbitrarily close to the trajectory.

Numerical analysis allows one to map out the dynamics of the system over a range of optomechanical couplings ranging from very weak ($\lambda \ll \omega_m$) through to the strong coupling regime ($\lambda \sim \omega_m$). There are limitations to this method, however, owing to the presence of dynamical multistability in the system. With the presence of multiple trajectories, which can be very sensitive to initial conditions, it is necessary to search for different types of motion by shear brute force; sweeping initial parameters through a range of values with the aim of picking up all possible long time behaviours.
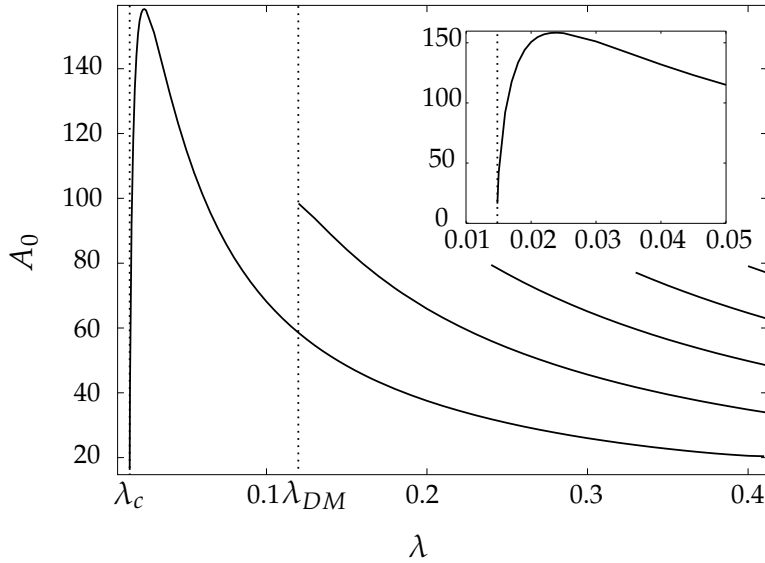
Figure 5.5: Amplitude of stable limit cycles, showing the onset of instabilities (λ_c) and dynamical multistability (λ_{DM}) as vertical dotted lines. Limit cycles are shown for a range of λ values, and occur along a series of branches. Inset shows a closeup of the weak coupling regime, where limit cycles appear at $\lambda_c = 0.0148$.

Since the limit cycles lie along several smooth curves, a limit cycle can usually be found at λ by selecting initial conditions which lie along the trajectory of a limit cycle at $\lambda - \delta\lambda$, where $\delta\lambda \ll \lambda$. This allows most curves to be completed once a couple of points along the curve have been found. This method does not, however, offer any certainty that all possible limit cycles and chaotic or period-doubled trajectories have been identified. In particular, the limit cycle curves have a start and end point, towards which the limit cycle attractor becomes more difficult to approach, unless an initial condition can be guessed close to, or along, the trajectory of interest.

To offer a more systematic method of mapping out the dynamics, an analytic description of the system is sought. The next section presents a calculation of the limit cycle amplitudes. This will require a series of approximations, which limit analysis to small λ values, such that $\lambda Q \ll \Delta\omega$. Whilst this approximation is not valid for the entire range of Figure 5.5, it will provide a systematic method of searching for limit cycles over the weak coupling range.

In this section the membrane motion is modelled by driven oscillations about the fixed position q_0 (as labelled in red in figure 5.1a), at a fixed amplitude, A, and fixed frequency, ω_m:

$$q(t) \;=\; q_0 + A\cos(\omega_m t), \tag{5.28}$$

This ansatz is supported by the numerical analysis of Section 5.3, where the limit cycle regime sees regular oscillations at approximately the mechanical frequency. Prior studies also support this ansatz[13, 67]. By selecting fixed parameters q_0, A and ω_m, one can search for periodic motion, seeking out parameters which fit this ansatz. The approach taken in this section utilises a similar method to that employed by Heinrich et. al.[67], extending the analysis to generalise the results.

Stable limit cycles occur when losses in the system are balanced by the radiation pressure forces[37, 41]. This is the case when the total damping in the system is zero. Applying this condition gives an estimate of where limit cycles occur. This requires an amplitude dependent expression for the damping due to back action, which is expressed in terms of the cavity mode operators. These will be deduced by writing down a Schrödinger equation and applying a rotating wave approximation.

5.4.1 *Damping due to Back Action*

In the regime where limit cycles are observed, the resonator behaves as a harmonic oscillator, undergoing periodic oscillations (see Figure 5.2a). With this in mind, the membrane motion is modelled via Equation 5.28. The classical equation of motion takes the form[9, 67]

$$\ddot{q} + \gamma\dot{q} + \omega_m^2 q \;=\; F_{rad}, \tag{5.29}$$

where F_{rad} is the radiation pressure force, introduced in Chapter 4, Section 4.3:

$$F_{rad} \;=\; \lambda\left(\alpha_L^* \alpha_L - \alpha_R^* \alpha_R\right). \tag{5.30}$$

The average mechanical power produced by the radiation pressure force is $\langle F_{rad}\dot{q}\rangle$ with the average taken over one oscillation cycle. An amplitude dependent damping due to back action can then defined in terms of this average power[49, 74],

$$\gamma_{BA}\langle\dot{q}^2\rangle \;=\; -\lambda\langle\left(|\alpha_L|^2 - |\alpha_R|^2\right)\dot{q}\rangle. \tag{5.31}$$

An expression for $\dot{q}$ follows when Equation 5.28 is differentiated,

$$\dot{q} \;=\; -A\omega_m \sin\left(\omega_m t\right), \tag{5.32}$$

with its average given by

$$\langle \dot{q}^2 \rangle \;=\; \frac{2\pi}{\omega_m} \int_0^{2\pi/\omega_m} \mathrm{d}t\, \dot{q}^2 \tag{5.33}$$

$$=\; \frac{A^2 \omega_m^2}{2}. \tag{5.34}$$

Stable limit cycles of amplitude A_0 are sought, by applying the energy balance condition:

$$\langle \dot{q} F_{rad} \rangle \;=\; -\gamma \langle \dot{q}^2 \rangle, \tag{5.35}$$

hence using Equation 5.31,

$$\gamma_{BA}(A_0) = -\gamma. \tag{5.36}$$

The displacement q is assumed to obey Equation 5.28 - this ansatz is then used to solve Equations 5.10 to 5.15. The expression for γ_{BA} in equation 5.31 is then given in terms of α_L, α_R and q, which are all functions of A. In multiplying by $\dot{q}$ and averaging, Equation 5.31 isolates the terms, in the expression $|\alpha_L|^2 - |\alpha_R|^2$, which oscillate at the driven mechanical frequency. This essentially picks out oscillations occurring at the correct frequency to become stable.

5.4.2   *Expressions for cavity variables*

Expressions for the cavity amplitudes are sought for fixed values of A and q_0, in order to obtain γ_{BA} using Equation 5.31. The equations of motion for the cavity variables, 5.12 and 5.10, are represented in matrix form,

$$\begin{pmatrix} \dot{\alpha}_R \\ \dot{\alpha}_L \end{pmatrix} = \frac{1}{i} \begin{pmatrix} \Delta'_R(q) - i\frac{\kappa}{2} & g \\ g & \Delta'_L(q) - i\frac{\kappa}{2} \end{pmatrix} \begin{pmatrix} \alpha_R \\ \alpha_L \end{pmatrix} + B_{in}(t), \tag{5.37}$$

where the input power, $B_{in}(t)$ is given by

$$B_{in}(t) = \begin{pmatrix} 0 \\ -i\Omega \end{pmatrix}. \tag{5.38}$$

To proceed, Equation 5.37 is transformed into a non-uniformly rotating frame, and expressed in terms of vectors $\begin{pmatrix} \tilde{a}_R & \tilde{a}_L \end{pmatrix}^T$, which relate to the cavity variables $\begin{pmatrix} \alpha_R & \alpha_L \end{pmatrix}^T$ by[67]

$$\alpha_j(t) = -i\Omega e^{\pm i\phi(t)} \int_{-\infty}^{0} dt' \left[\tilde{\alpha}_j(t,t') e^{-i\phi(t')} \right] e^{-\frac{\kappa}{2}(t-t')} e^{i\Delta t'}, \tag{5.39}$$

for $j = L, R$, where the phase factor is given by

$$\phi(t) = \frac{A\lambda}{\omega_m} \sin(\omega_m t), \tag{5.40}$$

and initial conditions are $\tilde{\alpha}_L(t', t') = 1$ and $\tilde{\alpha}_R(t', t') = 0$. This represents a single photon in the left chamber and an empty right chamber.

The variables $\tilde{\alpha}_i(t)$ obey the equation

$$\frac{d}{dt} \begin{pmatrix} \tilde{\alpha}_R \\ \tilde{\alpha}_L \end{pmatrix} = \frac{1}{i} \begin{pmatrix} \lambda q_0 & g e^{2i\phi(t)} \\ g e^{-2i\phi(t)} & -\lambda q_0 \end{pmatrix} \begin{pmatrix} \tilde{\alpha}_R \\ \tilde{\alpha}_L \end{pmatrix}. \tag{5.41}$$

Recall that q_0 is a constant representing the centre of mechanical oscillations. The time dependence then comes from the phase factor $\phi(t)$. This term is re-written using the Jacobi-Anger expansion[55],

$$g e^{2i\phi(t)} = \sum_{\nu=-\infty}^{\infty} g_\nu e^{i\nu\omega_m t}, \tag{5.42}$$

where the variable g_ν is defined

$$g_\nu = g J_\nu \left(\frac{2\overline{A}}{\omega_m} \right), \tag{5.43}$$

with $\overline{A} = \lambda A$. Equation 5.41 can then be written as a time dependent Schrödinger equation (TDSE),

$$i \frac{d}{dt} |\psi\rangle = H_1 |\psi\rangle, \tag{5.44}$$

where the wave vector takes the form

$$|\psi\rangle = \begin{pmatrix} \tilde{\alpha}_R & \tilde{\alpha}_L \end{pmatrix}^T \tag{5.45}$$

and Hamiltonian is given by

$$H_1 = \begin{pmatrix} \lambda q_0 & \sum_{\nu=-\infty}^{\infty} g_\nu e^{i\nu\omega_m t} \\ \sum_{\nu=-\infty}^{\infty} g_\nu e^{-i\nu\omega_m t} & -\lambda q_0 \end{pmatrix}, \tag{5.46}$$

which can be separated into time dependent and time independent parts:

$$H_1 = H_0 + V(t), \tag{5.47}$$

where

$$H_0 = \begin{pmatrix} \lambda q_0 & g_0 \\ g_0 & -\lambda q_0 \end{pmatrix}, \tag{5.48}$$

$$V(t) = \sum_{\substack{\nu=-\infty \\ \nu \neq 0}}^{\infty} g_\nu \begin{pmatrix} 0 & e^{i\nu\omega_m t} \\ e^{-i\nu\omega_m t} & 0 \end{pmatrix}. \tag{5.49}$$

Defining the following,

$$f_\nu(t) = e^{i\nu\omega_m t} + (-1)^\nu e^{-i\nu\omega_m t}, \tag{5.50}$$

The matrix $V(t)$ is then written

$$V(t) = \sum_{\nu=1}^{\infty} g_\nu \begin{pmatrix} 0 & f_\nu \\ (-1)^\nu f_\nu & 0 \end{pmatrix}, \tag{5.51}$$

where the relation $J_{-\nu}(x) = (-1)^\nu J_\nu(x)$ is used to change the limits of the sum[55].

5.4.3 *Solution to the Schrödinger equation and bases of the system*

States of the system, described by wave vectors $|\psi(t, t')\rangle$ (defined in Equation 5.45) obey the TDSE given in Equation 5.44. Figure 5.1b shows the cavity frequencies for the case where $g = 0$ (dashed black lines) and when $g \neq 0$ (solid blue curves). The transformed cavity modes can be expressed in terms of two different bases. These are the eigenmodes of H_0, when $g = 0$ and $g \neq 0$.

When $g = 0$, the system evolves under the Hamiltonian

$$H_0(g = 0) = \begin{pmatrix} \lambda q_0 & 0 \\ 0 & -\lambda q_0 \end{pmatrix}. \tag{5.52}$$

The basis of this matrix is described by eigenvectors $|R\rangle = \begin{pmatrix} 1 & 0 \end{pmatrix}$, for a photon in the right chamber, and $|L\rangle = \begin{pmatrix} 0 & 1 \end{pmatrix}$, for a photon in the left chamber. Initially, the left chamber is occupied, so that $|\psi(t', t')\rangle = \begin{pmatrix} 0 & 1 \end{pmatrix}^T$. The corresponding eigenvalues to $|R, L\rangle$ are frequencies $\pm\lambda q_0$.

For the general case $g \neq 0$, the system evolves under the Hamiltonian H_1. Treating $V(t)$ as a perturbation, the basis can be approximately described using eigenvectors of H_0, labelled $|\pm\rangle$. These have eigenvalues, $\omega_\pm$,

$$H_0|\pm\rangle = \omega_\pm|\pm\rangle, \tag{5.53}$$

where $\omega_\pm = \pm\sqrt{g_0^2 + (\lambda q_0)^2}$. The initial condition is given in terms of the basis $|R, L\rangle$, so a transformation between the two bases must be defined. This takes the form

$$\begin{pmatrix} \alpha_+ \\ \alpha_- \end{pmatrix} = \begin{pmatrix} u & v \\ x & y \end{pmatrix} \begin{pmatrix} \tilde{\alpha}_R \\ \tilde{\alpha}_L \end{pmatrix}, \qquad (5.54)$$

where u, v, x, y are time independent constants[2]. The basis vectors $|+\rangle$ and $|-\rangle$, describe photons in the upper and lower dispersion bands, respectively.

The state vector $|\psi(t, t')\rangle$ expanded in terms of the basis $|\pm\rangle$ is

$$|\psi(t, t')\rangle = \sum_{p=\pm} e^{-i\omega_p(t-t')} c_p(t)|p\rangle, \qquad (5.55)$$

where $c_p(t)$ are time dependent coefficients, yet to be determined.

Expressions for $\tilde{\alpha}_L$ and $\tilde{\alpha}_R$ are obtained by projecting $|\psi\rangle$ onto $|R\rangle$ and $|L\rangle$:

$$\tilde{\alpha}_R = \langle 1|\psi\rangle \qquad (5.56)$$
$$= \sum_{p=\pm} e^{-i\omega_p(t-t')} c_p \langle 1|p\rangle \qquad (5.57)$$
$$= e^{-i\omega_+(t-t')} c_+ \langle 1|+\rangle + e^{-i\omega_-(t-t')} c_- \langle 1|-\rangle, \quad (5.58)$$
$$\tilde{\alpha}_L = e^{-i\omega_+(t-t')} c_+ \langle 2|+\rangle + e^{-i\omega_-(t-t')} c_- \langle 2|-\rangle. \quad (5.59)$$

The time dependent coefficients are determined by

$$i\frac{d}{dt} c_p(t) = \sum_{q=\pm} V_{pq} e^{i(\omega_p - \omega_q)(t-t')} c_q. \qquad (5.60)$$

where

$$V_{pq} = \langle p|V|q\rangle. \qquad (5.61)$$

In order to determine the coefficients c_p, Equation 5.55 is differentiated:

$$\frac{d}{dt}|\psi\rangle = \sum_{p=\pm} \left(-i\omega_p c_p + \dot{c}_p\right) e^{-i\omega_p(t-t')}|p\rangle. \qquad (5.62)$$

Using Equation 5.55, the first term in the sum can be identified as the right hand side of equation 5.53, and substituting results into Equation 5.44 gives

$$V(t)|\psi\rangle = i\dot{c}_+ e^{-i\omega_+(t-t')}|+\rangle + i\dot{c}_- e^{-i\omega_-(t-t')}|-\rangle. \quad (5.63)$$

---

2 This transformation follows a similar process to that used in Chapter 3, detailed in Appendix D.

Splitting $V(t)$ into components allows for separate equations to be written for $\dot{c}_p(t)$. Given Equation 5.61, $V(t)$ can be written

$$V(t) = \sum_{p,q} V_{pq} |p\rangle\langle q|, \qquad (5.64)$$

which, combined with Equation 5.55, gives

$$V(t)|\psi\rangle = V_{++}|+\rangle c_+ e^{-i\omega_+(t-t')} + V_{+-}|+\rangle c_- e^{-i\omega_-(t-t')}$$
$$+ V_{-+}|-\rangle c_+ e^{-i\omega_+(t-t')} + V_{--}|-\rangle c_- e^{-i\omega_-(t-t')}. \qquad (5.65)$$

By equating equations 5.63 and 5.65, coefficients in $|+\rangle$ and $|-\rangle$ can be matched up.

$$i\dot{c}_+ = V_{++}c_+ + V_{+-}c_- e^{i\Delta_E(t-t')}, \qquad (5.66)$$
$$i\dot{c}_- = V_{--}c_- + V_{-+}c_+ e^{-i\Delta_E(t-t')}, \qquad (5.67)$$

where $\Delta_E = \omega_+ - \omega_-$.

In order to calculate $c_\pm(t)$, expressions for $V_{pq}(t)$ are required in the basis of $|\pm\rangle$. Consider the transformation in equation 5.54, which allows states $|\pm\rangle$ to be expressed as

$$|+\rangle = u|R\rangle + v|L\rangle \qquad (5.68)$$
$$|-\rangle = x|R\rangle + y|L\rangle. \qquad (5.69)$$

where the coefficients are

$$u = \frac{g_0}{\sqrt{\left(\frac{\Delta_E}{2} - \lambda q_0\right)^2 + g_0^2}}, \qquad (5.70)$$

$$v = \frac{\frac{\Delta_E}{2} - \lambda q_0}{\sqrt{\left(\frac{\Delta_E}{2} - \lambda q_0\right)^2 + g_0^2}}, \qquad (5.71)$$

$$x = \frac{g_0}{\sqrt{\left(\frac{\Delta_E}{2} + \lambda q_0\right)^2 + g_0^2}}, \qquad (5.72)$$

$$y = \frac{-\left(\frac{\Delta_E}{2} + \lambda q_0\right)}{\sqrt{\left(\frac{\Delta_E}{2} + \lambda q_0\right)^2 + g_0^2}}. \qquad (5.73)$$

This transformation allows elements of $V(t)$ to be expressed in the basis $|\pm\rangle$:

$$V_{++} = \langle +|V|+\rangle \qquad (5.74)$$
$$= \sum_\nu g_\nu f_\nu \left(1 + (-1)^\nu\right) ux \qquad (5.75)$$

By similar analysis,

$$V_{+-} = \sum_{\nu} g_{\nu} f_{\nu} \left(uy + (-1)^{\nu} vx \right) \tag{5.76}$$

$$V_{-+} = \sum_{\nu} g_{\nu} f_{\nu} \left(vx + (-1)^{\nu} uy \right) \tag{5.77}$$

$$V_{--} = \sum_{\nu} g_{\nu} f_{\nu} \left(1 + (-1)^{\nu} \right) vy. \tag{5.78}$$

5.4.4 *The Rabi problem*

This section has described an effective two level system, where the two levels can be identified as states in the cavity where a photon is in either the left or right chamber of the cavity. The presence of coupling, $g \neq 0$, causes the two modes to hybridise forming an upper and lower dispersion band with an anti-crossing (see Figure 5.1b). One can draw an analogy between this and the Rabi problem[1, 68], where a two level atom interacts with a laser field close to its transition frequency, creating hybridised upper and lower modes in the system.
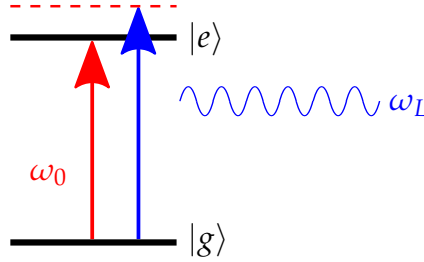
Figure 5.6: The Rabi problem: a two level atom with energy levels $|g\rangle$ and $|e\rangle$, separated by frequency ω_0 (red), driven close to resonance by a laser of frequency ω_L (blue), resulting in transitions between the two levels.

Consider the two level atom shown in Figure 5.6, with ground state $|g\rangle$ and excited state $|e\rangle$ separated by a frequency ω_0. The atom is initially in the ground state and driven close to resonance, by a laser of frequency ω_L. The laser is tuned such that $|\omega_0 - \omega_L| \ll |\omega_0 + \omega_L|$. The Hamiltonian can be expressed

$$H_R = \frac{1}{2}\omega_0 \sigma_z - \Lambda \cos\left(\omega_L t\right)\sigma_x, \tag{5.79}$$

where Λ is a constant and σ_x and σ_z are the Pauli matrices[75], given by

$$\sigma_z = |e\rangle\langle e| - |g\rangle\langle g| \tag{5.80}$$

$$\sigma_x = |e\rangle\langle g| + |g\rangle\langle e|. \tag{5.81}$$

This problem has been examined extensively[76], by implementing a rotating wave approximation (RWA). This allows a simple analytic description of the transition probabilities, by solving the TDSE, to express the wave vector $|\psi\rangle$ in terms of the basis $|g, e\rangle$:

$$i\frac{d|\psi\rangle}{dt} = H_R|\psi\rangle. \tag{5.82}$$

Writing

$$|\psi\rangle = c_g(t)e^{-i\omega_g t}|g\rangle + c_e(t)e^{-i\omega_e t}|e\rangle, \tag{5.83}$$

one can then deduce equations of motion for c_g and c_e from the TDSE:

$$\dot{c_g} = i\Lambda \cos\omega_L t e^{-i\omega_0 t} c_e \tag{5.84}$$

$$\dot{c_e} = i\Lambda \cos\omega_L t e^{i\omega_0 t} c_g. \tag{5.85}$$

Expanding the cosine term results in a pair of rotating terms in each equation:

$$\dot{c_g} = i\Lambda c_e \frac{1}{2}\left(e^{-i(\omega_L+\omega_0)t} + e^{i(\omega_L-\omega_0)t}\right) \tag{5.86}$$

$$\dot{c_e} = i\Lambda c_g \frac{1}{2}\left(e^{i(\omega_L+\omega_0)t} + e^{-i(\omega_L-\omega_0)t}\right). \tag{5.87}$$

The RWA is applied by noting that, since $|\omega_L - \omega_0| \ll |\omega_L + \omega_0|$, the first term in each equation is fast oscillating in comparison to the second term. Provided then, that the coupling Λ is also small, when an average is taken over any appreciable timescale, the contribution from the first term is negligible in comparison to that of the second term[56, 76]. As a result, the fast oscillating first term in each equation can be dropped, leaving two equations of motion which are analytically soluble. This allows for a relatively straight forward calculation of the transition probability, $|c_e|^2$.

Given the analogy that can be drawn between the Rabi problem and the two mode system of this chapter, the next section explores the case where the separation between the optical modes is close to an integer multiple of the mechanical frequency: $\Delta_E \approx n\omega_m$. In this case the mechanical mode acts like

the near-resonant laser, whilst the optical bands (at frequencies $\omega_\pm$) provide an effective two-level system. Here, however, the initial state is excited to the upper level so that energy is extracted to drive the resonator[16, 67]. By applying a RWA, the next section seeks to model the energy exchange analytically in order to describe limit cycle oscillations.

5.4.5   *Rotating Wave Approximation*

In order to deduce expressions for α_L and α_R, one must solve Equations 5.66 and 5.67 for $c_\pm$. Each element of V in the equations contains an infinite sum over ν. In this section the RWA allows these sums to be truncated, simplifying the calculation.

To motivate this approximation, consider the case where $2g \sim \omega_m$. As discussed in Chapter 4, analysis of the damping due to back action reveals the strongest driving and damping in the resonator when $\omega_+ - \omega_- = \omega_m$. As a result, when the cavity is driven close to the upper dispersion band ($\Delta = -\omega_+$), transitions to the lower dispersion band (at frequency ω_-) are possible, where a single phonon is created, driving oscillations in the resonator. One can generalise this effect to n phonons, when $\omega_+ - \omega_- = n\omega_m$.

Equations describing the constants $c_\pm$ contain sums over different exponents, $\pm\nu\omega_m t$ and $\pm(\Delta_E \pm \nu\omega_m)(t - t')$:

$$
\begin{aligned}
i\dot{c}_+ \; = \; \sum_\nu \Bigg[& H_\nu ux \left[e^{i\nu\omega_m t} + (-1)^\nu e^{-i\nu\omega_m t} \right] c_+ \\
& + G_\nu \left[e^{i\nu\omega_m t} + (-1)^\nu e^{-i\nu\omega_m t} \right] e^{i\Delta_E(t-t')} c_- \Bigg]
\end{aligned}
\tag{5.88}
$$

$$
\begin{aligned}
i\dot{c}_- \; = \; \sum_\nu \Bigg[& (-1)^\nu G_\nu \left[e^{i\nu\omega_m t} + (-1)^\nu e^{-i\nu\omega_m t} \right] e^{-i\Delta_E(t-t')} c_+ \\
& + H_\nu vy \left[e^{i\nu\omega_m t} + (-1)^\nu e^{-i\nu\omega_m t} \right] c_- \Bigg],
\end{aligned}
\tag{5.89}
$$

where Equations 5.75 to 5.78 have been substituted into Equation 5.66 and 5.67, and

$$
\begin{aligned}
G_\nu &= g_\nu \left(uy + (-1)^\nu vx \right) & (5.90) \\
H_\nu &= g_\nu \left(1 + (-1)^\nu \right). & (5.91)
\end{aligned}
$$

Applying the RWA allows one to discard all terms except those with exponents $\pm(\Delta_E - n\omega_m)$. This allows the sums over ν to

be truncated so that only a single term, n, in the sum remains. For this to work, the system must be driven close to resonance ($\Delta \approx \omega_+$) - in order to excite the upper cavity mode - and the energy gap between the optical modes must be close to an integer multiple, n, of the mechanical frequency. Specifically, one requires $|\Delta_E - n\omega_m| \ll |\Delta_E + n\omega_m|$. In addition, it is required that the coupling is small, $g_n \ll \Delta_E$, so that the averages of the fast rotating terms remain small. As stated in Section 5.4.2, this is assumed to be the case.

The calculation is generalized for an integer number, n, but results are shown for $n = 1$. With n odd, the only non-zero matrix elements are

$$V_{+-} = g_n f_n, \tag{5.92}$$
$$V_{-+} = -g_n f_n. \tag{5.93}$$

Given Equations 5.66 and 5.67, equations of motion for the coefficients $c_\pm$ are written:

$$\dot{c}_+(t) = i g_n e^{-in\omega_m t'} e^{i(\Delta_E - n\omega_m)(t-t')} c_- \tag{5.94}$$
$$\dot{c}_-(t) = i g_n e^{in\omega_m t'} e^{-i(\Delta_E - n\omega_m)(t-t')} c_+, \tag{5.95}$$

where the RWA allows the term of frequency $\Delta_E + n\omega_m$ to be discarded. Note that whilst the above analysis assumed n is odd, for the case of even n, a similar set of equations are reached, with the addition of a factor $2\lambda q_0/\Delta_E$ on the right hand side of each equation. The elements V_{++} and V_{--} are non-zero, but their contributions can also be discarded in the RWA, owing to the weak coupling and exponents $\pm \omega_m t$, which result in rapidly rotating terms. Details are given in Appendix F.

Equation 5.39 expresses $\begin{pmatrix} \alpha_R & \alpha_L \end{pmatrix}^T$ in terms of $\begin{pmatrix} \tilde{a}_R & \tilde{a}_L \end{pmatrix}^T$, which are expressed in terms of coefficients $c_\pm$ in equations 5.58 and 5.59. The coefficients are found by solving Equations 5.94 and 5.95 simultaneously. An ansatz, $c_+(t) = C_0 e^{\theta(t-t')}$, is made, with constants c_0 and θ. Initial conditions are $c_+(t', t') = \langle +|2 \rangle$

and $c_-(t', t') = \langle -|2 \rangle$. Defining $\Omega_n = \Delta_E - n\omega_m$, the resulting expressions are

$$c_+(t, t') = \frac{1}{2}\left[\left(A_n\langle L|+\rangle + \frac{g_n}{2\omega_R}e^{-in\omega_m t'}\langle L|-\rangle \right) e^{i\omega_R(t-t')} \quad (5.96) \right.$$

$$\left. + \left(B_n\langle L|+\rangle - \frac{g_n}{2\omega_R}e^{-in\omega_m t'}\langle L|-\rangle \right)e^{-i\omega_R(t-t')} \right] e^{i\Omega_n(t-t')},$$

$$c_-(t, t') = \frac{1}{2}\left[\left(B_n\langle L|-\rangle + \frac{g_n}{2\omega_R}e^{in\omega_m t'}\langle L|+\rangle \right) e^{i\omega_R(t-t')} \quad (5.97) \right.$$

$$\left. + \left(A_n\langle L|-\rangle - \frac{g_n}{2\omega_R}e^{in\omega_m t'}\langle L|+\rangle \right)e^{-i\omega_R(t-t')} \right] e^{-i\Omega_n(t-t')},$$

where

$$A_n = \frac{\omega_R - (\Delta_E - n\omega_m)/2}{\omega_R} \quad (5.98)$$

$$B_n = \frac{\omega_R + (\Delta_E - n\omega_m)/2}{\omega_R}, \quad (5.99)$$

and ω_R is the Rabi frequency, defined by

$$\omega_R = \sqrt{g_n^2 + (\Delta_E - n\omega_m)^2/4}. \quad (5.100)$$

Expressions for the average light field operators follow, from equations 5.58 and 5.59,

$$\alpha_L(t) = \frac{-i\Omega}{2}\sum_m J_m e^{-i(\Delta + m\omega_m)t}H_{n,m}^{(L)} \quad (5.101)$$

$$\alpha_R(t) = \frac{-i\Omega}{2}\sum_m J_m e^{-i(\Delta + m\omega_m)t}H_{n,m}^{(R)} \quad (5.102)$$

where the shorthand $J_m = J_m(\overline{A}/\omega_m)$ is introduced and

$$H_{n,m}^{L(R)} = C_{n,m}^{(L(R))} + D_{n,m}^{(L(R))}e^{-in\omega_m t} + E_{n,m}^{(L(R))}e^{in\omega_m t}, \quad (5.103)$$

where the following are defined:

$$C_{n,m}^{(R,L)} = \langle L|+\rangle\langle +|R, L\rangle \left(\frac{A_n}{W_{n,m}^+} + \frac{B_n}{X_{n,m}^-} \right)$$

$$+ \langle L|-\rangle\langle -|R, L\rangle \left(\frac{B_n}{X_{n,m}^+} + \frac{A_n}{W_{n,m}^-} \right) \quad (5.104)$$

$$D_{n,m}^{(R,L)} = \langle L|-\rangle\langle +|R, L\rangle\frac{g_n}{\omega_R} \left(\frac{1}{W_{n,m}^-} - \frac{1}{X_{n,m}^+} \right) \quad (5.105)$$

$$E_{n,m}^{(R,L)} = \langle L|+\rangle\langle -|R, L\rangle\frac{g_n}{\omega_R} \left(\frac{1}{X_{n,m}^-} - \frac{1}{W_{n,m}^+} \right), \quad (5.106)$$

and

$$W_{n,m}^{\pm} = \frac{\kappa}{2} \mp i \left[\omega_R \pm \left(m - \frac{n}{2} \right) \omega_m \pm \Delta \right] \tag{5.107}$$

$$X_{n,m}^{\pm} = \frac{\kappa}{2} \mp i \left[\omega_R \pm \left(m + \frac{n}{2} \right) \omega_m \pm \Delta \right]. \tag{5.108}$$

When the average $\langle \left(|a_L|^2 - |a_R|^2 \right) \dot{q} \rangle$ is taken, only terms of frequency $\pm \omega_m$ give a non zero contribution to the sum over $|\alpha_L|^2 - |\alpha_R|^2$, the result is

$$\gamma_{BA}(A) = \frac{\lambda \Omega^2}{4Ai} \sum_m J_m \Bigg[\chi_1^{n,m,m+1} J_{m+1} - \chi_1^{n,m,m-1} J_{m-1}$$

$$+ \chi_2^{n,m,m-n+1} J_{m-n+1} - \chi_2^{n,m,m-n-1} J_{m-n-1}$$

$$+ \chi_3^{n,m,m+n+1} J_{m+n+1} - \chi_3^{n,m,m+n-1} J_{m+n-1}$$

$$+ \chi_4^{n,m,m+2n+1} J_{m+2n+1} - \chi_4^{n,m,m+2n-1} J_{m+2n-1}$$

$$+ \chi_5^{n,m,m-2n+1} J_{m-2n+1} - \chi_5^{n,m,m-2n-1} J_{m-2n-1} \Bigg] \tag{5.109}$$

where the following are defined:

$$\chi_1^{n,m,m'} = C_{n,m}^{(L)*} C_{n,m'}^{(L)} - C_{n,m}^{(R)*} C_{n,m'}^{(R)} + D_{n,m}^{(L)*} D_{n,m'}^{(L)}$$

$$- D_{n,m}^{(R)*} D_{n,m'}^{(R)} + E_{n,m}^{(L)*} E_{n,m'}^{(L)} - E_{n,m}^{(R)*} E_{n,m'}^{(R)} \tag{5.110}$$

$$\chi_2^{n,m,m'} = C_{n,m}^{(L)*} D_{n,m'}^{(L)} - C_{n,m}^{(R)*} D_{n,m'}^{(R)} + C_{n,m}^{(L)*} E_{n,m'}^{(L)}$$

$$- C_{n,m}^{(R)*} E_{n,m'}^{(R)} \tag{5.111}$$

$$\chi_3^{n,m,m'} = C_{n,m}^{(L)*} E_{n,m'}^{(L)} - C_{n,m}^{(R)*} E_{n,m'}^{(R)} + C_{n,m}^{(L)*} D_{n,m'}^{(L)}$$

$$- C_{n,m}^{(R)*} D_{n,m'}^{(R)} \tag{5.112}$$

$$\chi_4^{n,m,m'} = D_{n,m}^{(L)*} E_{n,m'}^{(L)} - D_{n,m}^{(R)*} E_{n,m'}^{(R)} \tag{5.113}$$

$$\chi_5^{n,m,m'} = D_{n,m'}^{(L)} E_{n,m}^{(L)*} - D_{n,m'}^{(R)} E_{n,m}^{(R)*}. \tag{5.114}$$

Note that there is now a single sum, over multiple Bessel functions, comprised of many complex terms. In practice, the sum is performed numerically, so that limits extend from $-M$ to M, where M is a real integer. As $M \to \infty$, the imaginary components cancel, producing a purely real value γ_{BA}, as is required. This value converges for large M, such that one can take $M = 30$. As m increases, the coefficients $\chi_i^{n,m,m'}$ in Equation 5.109 converge towards zero, as the denominators $W_{n,m}^{\pm}$ and $X_{n,m}^{\pm}$ increase. In fact, increasing value at which the sum is truncated does not appear to alter the value of $\Re[\gamma_{BA}]$ past $M = 5$,

however one requires $M = 30$ to ensure that $\Im[\gamma_{BA}] \ll \Re[\gamma_{BA}]$, whilst offering a quantity which can be computed fairly rapidly.

One can compare the results of the calculation to the linearized result of Chapter 4, in the regime where the fixed point state is stable. Taking the limit $A \to 0$ in Equation 5.109 leaves only the amplitude-independent zeroth order term. The resulting value of γ_{BA} closely matches the linearized result. The agreement between the two calculations is illustrated in Figure 5.7, which shows the relative error between the two:

$$\delta\gamma = \frac{\gamma_{BA}(A = 0) - \gamma_{LIN}}{\gamma_{BA}}, \tag{5.115}$$

where γ_{LIN} represents the linearized value of the damping due to back action, given in Equation 4.92 of Chapter 4. The curve increases rapidly with λ, but remains small for the range plotted. As λ increases, the linearization of Equations 4.16 to 4.19 in Chapter 4 becomes less accurate and so the two calculations begin to deviate.

The RWA requires $n\omega_m \approx \Delta_E$, in order that the optical modes are separated by an integer number of mechanical quanta. The minimum separation between the optical modes is $2\sqrt{g^2 + \lambda^2 q_0^2}$, where the cavity shift $\lambda q_0 = \Delta\omega + \lambda Q$. Contributions to the cavity shift come from the equilibrium displacement and the fixed point displacement of the resonator. The calculation of Equation 5.109 is simplified by ignoring the cavity shift from the displacement Q (shown in green in Figure 5.1a). For the regime where oscillations decay (Figure 5.4a) it is evident that this contribution is small. There is, however, a change in behaviour as λ_c is approached. As a starting point, it is assumed that $\lambda Q \ll \Delta\omega$, so that $\lambda q_0 \approx \Delta\omega$.

In addition, there is a small frequency shift in the mechanical oscillations. Over the vast range of limit cycles the shift is negligible - remaining within 1% of ω_m, but around $\lambda \approx 0.4$ the shift reaches 5% of ω_m and continues to grow. Ideally, one would need to account for the mechanical frequency shift, but since it is negligible over the majority of the range of parameters addressed here, it is neglected.

5.4.6 *Limit cycle dynamics*

For $\lambda > \lambda_c$, the system reaches stable limit cycles in the long time limit. The analysis from Chapter 2, Section 2.3.3 is applied to Equation 5.109 to determine the amplitude of stable limit
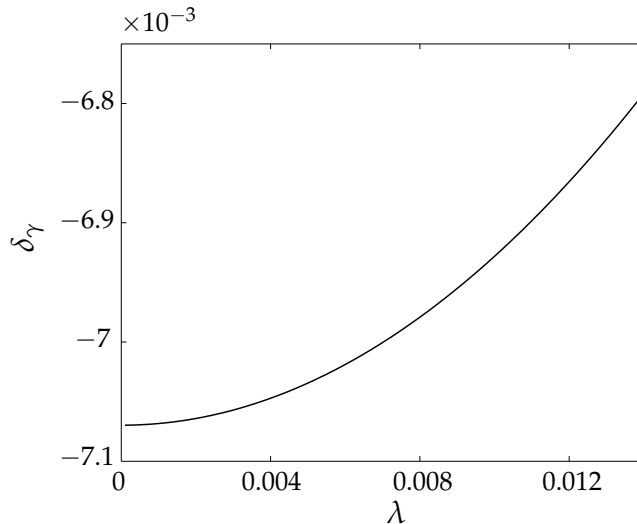
Figure 5.7: Relative error when comparing the damping due to back action, as given in Equation 5.109 (solid) and compared with the linearized calculation of Chapter 4. The error is very small over the range where the fixed point state is stable, and increases with λ, as expected.

cycles. Recall the stability condition (quoted in Equation 5.36), indicating the size of limit cycles, A_0. If the gradient of γ_{BA} is positive at A_0, the limit cycle is stable. In this manner, the limit cycle dynamics of the system are mapped out for a range of λ values. Figure 5.8 offers a comparison between the numerically and analytically generated amplitudes, for $\lambda \leq 0.41$.

The analytic calculation appears to capture the limit cycle dynamics remarkably well, particularly at smaller λ values, $\lambda_c \leq \lambda \leq 0.05$. Small discrepancies can be noted, both along each curve as λ increases, and between curves as limit cycles appear further out. The most notable discrepancy is the failure of analytics to detect limit cycles towards the end of certain branches. Considering the approximation $\lambda q_0 \approx \Delta\omega$, it is not surprising that the calculation would become less accurate at stronger coupling; Figure 5.4a indicates a rapid increase in λQ with λ as the limit cycle regime is reached.

Turning, now, to the approximations applied in the analytical calculation, Figure 5.9 addresses two of the assumptions made. The additional cavity shift, λQ, occurs due to the imbalance between occupations of the left and right cavities, such that $\lambda q_0 = \Delta\omega + \lambda Q$. In taking $\lambda q_0 = \Delta\omega$, errors are introduced in the calculation, affecting the values of Δ_E and ω_R as well as the accuracy of the RWA. Figure 5.9a shows the ratio between the assumed cavity shift, $\Delta\omega$, and the shift from the fixed point
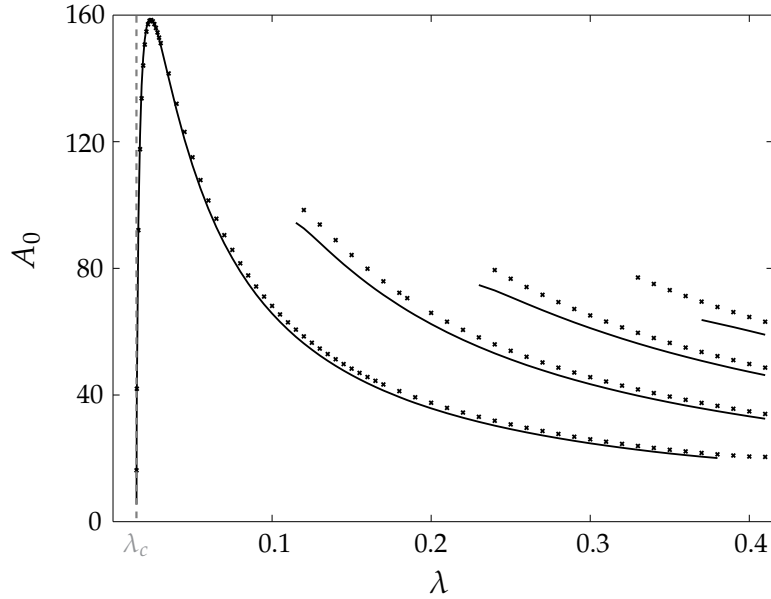
Figure 5.8: Analytic calculation of limit cycle sizes (solid lines), using Equation 5.109 and the analysis outlined in Chapter 2. This is compared to the numerical data generated in Section 5.3 (crosses). As seen in Figure 5.5, the stable cycles lie along smooth curves separated into different branches. The two sets of results prove to match closely, with the main discrepancies arising towards the end of each branch, where analytics fail to predict limit cycles seen in numerical calculations. The vertical dotted line at λ_c indicates where the instability arises and limit cycles emerge.

displacement, λQ (calculated numerically). Qualitatively, there is a clear increase with λ along each curve, as well as sharp increases between curves that is consistent with the decreases in accuracy noted along and between branches in Figure 5.8. However, quantitatively the λQ values plotted are very high, compared with $\Delta \omega$. In light of such large cavity shifts, the accuracy of the analytic calculation is perplexing.

Also shown, in Figure 5.9b, is the relative error between the frequency of oscillations in $q(t)$ and the mechanical frequency, $\delta \omega_m = (\omega_{eff} - \omega_m)/\omega_m$. For the range plotted, $\delta \omega_m < 0.1$, so that the shift remains small - however there is a noticeable increase in $\delta \omega_m$ for the first branch as $\lambda \to 0.4$, where the analytics begin to fail. These values appear consistent with the success of the analytic approach.
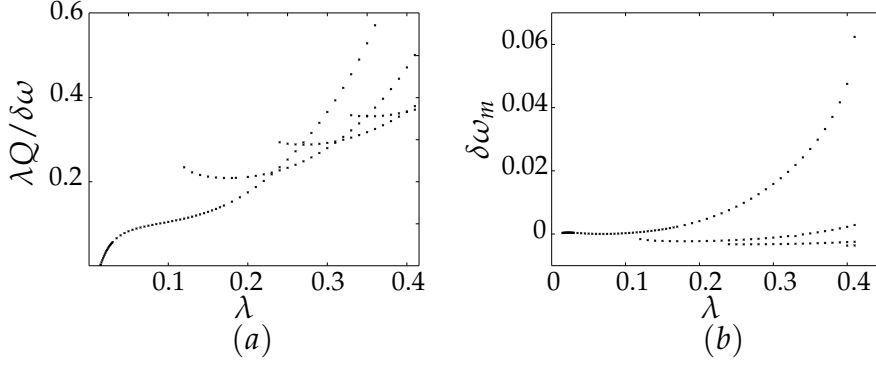
Figure 5.9: Analysis of quantities ignored in calculating γ_{BA}: (a) the ratio between the cavity shift from the fixed point displacement and the , $\lambda Q/\Delta\omega$, and (b) the relative error in the shifted mechanical frequency. In (a), the fixed point appears to cause a significant shift in the cavity frequency, in comparison to the equilibrium shift. Whilst in (b) the correction remains small, there is an increase as $\lambda \to 0.4$ and the discrepancies appear in the analytics.
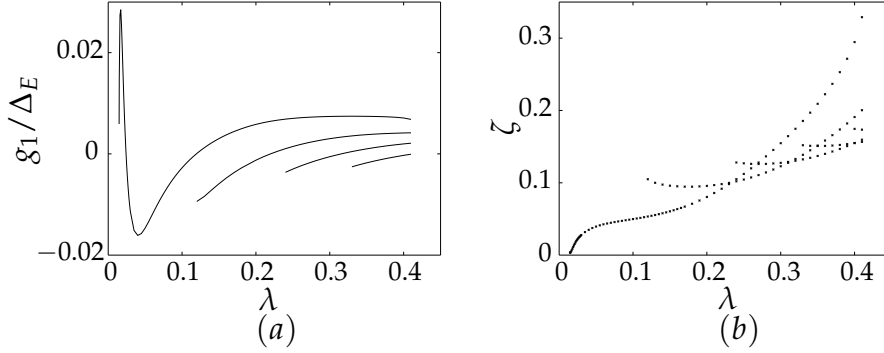
Figure 5.10: Conditions of the RWA: (a) the coupling term, g_1/Δ_E and (b) $\zeta = |\Delta_E - n\omega_m|/|\Delta_E + n\omega_m|$. In order to apply the RWA, these two quantities must be far below unity. It is evident that the coupling is small for the range considered. The quantity ζ grows significantly with λ; in particular, there is a rapid increase near $\lambda = 0.4$, where the analytics fail to capture limit cycles on the first branch of the curve.

The success of the RWA can be understood by re-addressing the assumptions with the cavity mode separation defined to include the additional shift:

$$\Delta_E = 2\sqrt{g_0^2 + (\Delta\omega + \lambda Q)^2}. \tag{5.116}$$

To that end, the ratio ζ is defined,

$$\zeta = \frac{|\Delta_E - n\omega_m|}{|\Delta_E + n\omega_m|}, \tag{5.117}$$

and examined alongside the coupling term g_1/ω_m in Figure 5.10. It is immediately apparent that $g_1/\omega_m \ll 1$ for the range of λ in question so that the weak coupling condition of the RWA is satisfied. It is also required that $\zeta \ll 1$, in order for the system to be close to resonance. For $\lambda < 0.3$, the ratio ζ remains below 0.2. This suggests that the system is indeed close to resonance, and the RWA is relatively accurate. For $\lambda > 0.3$ the ratio increases rapidly, and bigger discrepancies occur between the results in Figure 5.8 - this is where the analytics start to fail at predicting the presence of certain limit cycles.

5.5   CONCLUSION

In conclusion, this chapter has mapped out the dynamics of the driven regime for a multimode optomechanical system. A variety of behaviours have been investigated numerically, including the emergence of multiple limit cycles and chaos. Whilst the presence of multiple attractors prohibits a truly systematic analysis of the system, a fairly detailed picture of the limit cycle dynamics has been obtained for weaker coupling values. Furthermore, this aspect of the dynamics has been explored analytically. A rotating wave approximation allows an incredibly accurate prediction of the limit cycle amplitudes in the weak coupling regime. The success of the calculation seems surprising, considering the significant contribution to the cavity shift which is ignored, however closer inspection reveals that the assumptions of the rotating wave approximation are met sufficiently to allow for an accurate calculation.

Appendices

A

DETAILS OF WIGNER TRANSFORMATION

Given a master equation,

$$\dot{\rho} = -i\left[H_{eff}, \tilde{\rho}\right] + \hat{\mathcal{L}}_m \tilde{\rho} + \hat{\mathcal{L}}_c \tilde{\rho}, \qquad \text{(A.1)}$$

it is possible to perform a transformation which results in a c-number equation for the system - a semi-classical equation in terms of complex numbers[50]. The benefit of this is that, in certain cases, a Fokker-Planck type equation can obtained, from which Langevin equations of motion can be deduced. For this particular system, a further approximation will be required in order to obtain a Fokker-Planck equation[1, 31].

This type of transformation is possible using a number of different representations[1] including the P and Q-representations. In this instance, the Wigner representation is chosen, as it offers the most simple transformation for evaluating averages of symmetrically ordered products of creation and annihilation operators. The system is then described in terms of a set of semi-classical variables whose moments correspond to averages of symmetrically ordered operators (as demonstrated in Equations 2.25 and 2.26). The Wigner function is defined in Equation 2.23, and can be thought of as the quantum mechanical analogue of the classical probability distribution. The transformation is performed by first defining the Wigner transformations on individual operators, then deducing the action on multiple operators.

The Wigner transformations on operators a and a^* are defined [1]

$$W(a) = \alpha \qquad \text{(A.2)}$$
$$W(a^\dagger) = \alpha^*, \qquad \text{(A.3)}$$

where α and α^* are semi-classical variables which replace the quantum operators a and $a^\dagger$. The Wigner function of the density operator $W(\rho)$ is unknown, as ρ cannot be specified, so equations are written in terms of $W(\rho)$. The Wigner transformation proceeds by writing Wigner functions for each term in the master equation 2.21. Each term consists of products of operators a, $a^\dagger$, b, $b^\dagger$ and ρ. With Wigner functions for each of these operators defined, a transformation is applied, which allows Wigner

functions of products of operators, $W(AB)$, to be expressed as functions of the Wigner functions for the individual operators, $W(A)$ and $W(B)$:

$$W(AB) \;=\; W(A)e^{\frac{1}{2}\left(\overleftarrow{\partial}_\alpha \overrightarrow{\partial}_{\alpha^*} - \overleftarrow{\partial}_{\alpha^*} \overrightarrow{\partial}_\alpha\right)}W(B), \qquad (A.4)$$

where $\overleftarrow{\partial}_\alpha$ denotes a differential acting to the left, and $\overrightarrow{\partial}_\alpha$ denotes a differential acting to the right.

Equation A.4 can be applied to transform the expanded terms of Equation 2.21, the term $i\Delta a^\dagger a\rho$ transforms as

$$
\begin{aligned}
W(i\Delta a^\dagger a\rho) \;&=\; i\Delta W(a^\dagger a)e^{\frac{1}{2}\left(\overleftarrow{\partial}_\alpha \overrightarrow{\partial}_{\alpha}^* - \overleftarrow{\partial}_{\alpha}^* \overrightarrow{\partial}_\alpha\right)}W(\rho) \qquad &(A.5)\\[2mm]
&=\; i\Delta\left[W(a^\dagger)e^{\frac{1}{2}\left(\overleftarrow{\partial}_\alpha \overrightarrow{\partial}_{\alpha}^* - \overleftarrow{\partial}_{\alpha}^* \overrightarrow{\partial}_\alpha\right)}W(a)\right]\times\\[2mm]
&\quad\; e^{\frac{1}{2}\left(\overleftarrow{\partial}_\alpha \overrightarrow{\partial}_{\alpha}^* - \overleftarrow{\partial}_{\alpha}^* \overrightarrow{\partial}_\alpha\right)}W(\rho) \qquad &(A.6)\\[2mm]
&=\; i\Delta(\alpha^* - \tfrac{1}{2}\partial_\alpha)(\alpha + \tfrac{1}{2}\partial_{\alpha^*})W(\rho) \qquad &(A.7)\\[2mm]
&=\; i\Delta\left[\alpha^*\alpha - \frac{1}{2} + \frac{1}{2}(\alpha^*\partial_{\alpha^*} - \alpha\partial_\alpha) -\right.\\[2mm]
&\quad\; \left.\frac{1}{4}\partial_{\alpha^*}\partial_\alpha\right]W(\rho) \qquad &(A.8)
\end{aligned}
$$

Treating further terms in the same way as this leads to the final form of the c-number equation, given in Equation 2.27.

B

TWO POINT CORRELATOR FOR CAVITY FLUCTUATIONS

The solution to Equation 2.35 yields expressions for the fluctuations in α and α^*:

$$\delta\tilde{\alpha}(\omega) = \frac{\tilde{\eta}_\alpha(\omega)}{\frac{\kappa}{2} + i(\omega + \Delta')}, \tag{B.1}$$

$$\delta\tilde{\alpha}^*(\omega) = \frac{\tilde{\eta}_{\alpha^*}(\omega)}{\frac{\kappa}{2} + i(\omega - \Delta')}. \tag{B.2}$$

Given

$$\tilde{\eta}_\alpha(\omega) = \eta_\alpha(\omega)e^{iz\sin(\omega'_m t + \phi)} \tag{B.3}$$

$$\tilde{\eta}_{\alpha^*}(\omega) = \eta_{\alpha^*}(\omega)e^{-iz\sin(\omega'_m t + \phi)}, \tag{B.4}$$

when calculating the two point correlation function, exponents cancel and

$$\langle \tilde{\eta}_\alpha(\omega)\tilde{\eta}_{\alpha^*}(\omega')\rangle = \langle \eta_\alpha(\omega)\eta_{\alpha^*}(\omega')\rangle. \tag{B.5}$$

The two point correlation function is calculated by performing a Fourier transform, given that $\langle \eta_\alpha(\omega)\eta_{\alpha^*}(\omega')\rangle = \frac{\kappa}{2}\delta(\omega + \omega')$,

$$\langle \delta\alpha(t)\delta\alpha^*(t')\rangle = \frac{1}{2\pi}\int_{-\infty}^{\infty}d\omega \int_{-\infty}^{\infty}d\omega' \frac{\langle \tilde{\eta}_\alpha(\omega)\tilde{\eta}_{\alpha^*}(\omega')\rangle}{[\frac{\kappa}{2} + i(\omega + \Delta')][\frac{\kappa}{2} + i(\omega' - \Delta')]}$$

$$= \frac{1}{2\pi}\int_{-\infty}^{\infty}d\omega \frac{\frac{\kappa}{2}}{\left(\frac{\kappa}{2}\right)^2 + (\omega + \Delta')^2}. \tag{B.6}$$

The integral over ω is performed using the substitution

$$\omega + \Delta' = \frac{\kappa}{2}\tan(\theta) \tag{B.7}$$

$$d\omega = \frac{\kappa}{2}\sec^2(\theta)d\theta. \tag{B.8}$$

The integral to be evaluated is then

$$\langle \delta\alpha(t)\delta\alpha^*(t')\rangle = \frac{1}{2\pi}\int_{-\frac{\pi}{2}}^{\frac{\pi}{2}}d\theta \frac{\sec^2(\theta)}{1 + \tan^2(\theta)}, \tag{B.9}$$

$$= \frac{1}{2\pi}\int_{-\frac{\pi}{2}}^{\frac{\pi}{2}}d\theta, \tag{B.10}$$

$$= \frac{1}{2}. \tag{B.11}$$

With this in mind, the term $\alpha^*\alpha - \frac{1}{2}$ can be evaluated, by averaging the second order fluctuations:

$$
\begin{aligned}
\alpha^*\alpha - \frac{1}{2} &= \langle\alpha^*\rangle\langle\alpha\rangle + \langle\alpha^*\rangle\delta\alpha + \langle\alpha\rangle\delta\alpha^* + \langle\delta\alpha^*\delta\alpha\rangle \\
&\quad -\frac{1}{2} \\
&= \langle\alpha^*\rangle\langle\alpha\rangle + \langle\alpha^*\rangle\delta\alpha + \langle\alpha\rangle\delta\alpha^*,
\end{aligned}
$$

$$(B.12)$$

$$(B.13)$$

which gives the expression in Equation 2.46.

C

DETAILS OF NUMERICAL CALCULATION

In Chapters 2 and 3 a master equation is written for the system. The numerical approach involves analysing the dynamics of the resonator by solving the master equation directly, giving ρ. The equation takes the form

$$\dot{\rho}(t) = \hat{\mathcal{L}}\rho(t), \tag{C.1}$$

where $\rho(t)$ is the density matrix and $\hat{\mathcal{L}}$ the Liouvillian, a super-operator. In order to solve this as an eigenvalue equation, it is written in Liouville space representation [60, 77]; matrices are transformed to vectors by writing out columns consecutively as a single column, then $\hat{\mathcal{L}}$ can be written as a matrix, which acts on the vector ρ in the same way as the super operator on the matrix ρ. This is denoted in the following way:

$$|\dot{\rho}\rangle\rangle = \mathcal{L}|\rho\rangle\rangle \tag{C.2}$$

The matrix $\mathcal{L}$ is non-Hermitian, and has a separate set of right and left eigenvectors:

$$\mathcal{L}|R_n\rangle\rangle = \Lambda_n|R_n\rangle\rangle \tag{C.3}$$
$$\langle\langle L_n|\mathcal{L} = \Lambda_n\langle\langle L_n|, \tag{C.4}$$

where in the absence of degeneracy, the eigenvectors can be assumed to form a complete orthonormal set[60]. A solution to Equation C.2 can be found, then expanded in terms of the eigenvalues, Λ_n:

$$|\rho(t)\rangle\rangle = e^{\mathcal{L}t}|\rho(0)\rangle\rangle \tag{C.5}$$
$$= |\rho_{SS}\rangle\rangle + \sum_{n=0}^{N-1}\langle\langle L_n|\rho(0)e^{\Lambda_n t}|R_n\rangle\rangle, \tag{C.6}$$

where $\rho(0)$ is an initial density matrix and the matrix $\mathcal{L}$ has N eigenvalues Λ_n. The eigenvector with zero eigenvalue $\lambda = 0$ and right eigenvector, $|R_0\rangle\rangle$, is the steady state density operator, $|\rho_{SS}\rangle\rangle$ and normalised to give $\langle\langle L_0| = \langle\langle\hat{I}|$. All further eigenvalues satisfy $\Re[\Lambda_n] < 0$[78] and describe different timescales in the evolution of the system. Solutions for $\rho(t)$ can then be expressed using an eigendecomposition of the matrix $\mathcal{L}$. The

result is a sum of the steady state density matrix together with a series of transient terms.

The eigenvector $|\rho_{SS}\rangle\rangle$ is found by solving Equation C.2 numerically. In general, in infinite number of states are available to the cavity and resonator. In order to perform numerical analysis, however, the spaces of cavity and resonator state must be truncated to a finite number of states. This produces accurate results, provided parameters are chosen such that there is a negligible probability of the cavity(resonator) occupying states with energies higher than $N_a(N_b)$. The matrix $\mathcal{L}$ therefore contains $\left(N_a^2 \times N_b^2\right)^2$ elements. In this thesis, parameters of interest generally require an order of $N_b \sim 100$ resonator states, which generates matrices too large to deal with. This is tackled by observing that most of the off diagonal elements are negligible in size, and can be discarded. The calculation proceeds by considering only a finite number of off-diagonal elements. Checks are included in the calculation so that when the matrix is reduced, the elements discarded are below a certain value, or the number included will be increased.

D

TRANSFORMATION OF HAMILTONIAN FROM UNCOUPLED TO COUPLED CAVITY MODES

Here the transformation from equation 3.3 to 3.12 is detailed. This describes the transformation between operators a_L, a_R with frequencies ω_L and ω_R, and operators a_1 and a_2 with frequencies ω_1 and ω_2. A Bogoliubov transformation is applied to the vector $\begin{pmatrix} a_L & a_R \end{pmatrix}^T$, this takes the form

$$\begin{pmatrix} a_1 \\ a_2 \end{pmatrix} = \begin{pmatrix} u & v \\ x & y \end{pmatrix} \begin{pmatrix} a_L \\ a_R \end{pmatrix}. \tag{D.1}$$

Operators a_L and a_R represent the left and right modes, with frequencies ω_L and ω_R, while the upper and lower branches of the dispersion curve (Figure 3.1b) are described by operators a_1 and a_2 with frequencies ω_1 and ω_2 respectively. Coefficients u, v, x and y are found by imposing commutation relations to a_1 and a_2:

$$[a_{1(2)}, a_{1(2)}^\dagger] = 1 \tag{D.2}$$

$$[a_{1(2)}, a_{1(2)}] = 0 \tag{D.3}$$

$$[a_{1(2)}^\dagger, a_{1(2)}^\dagger] = 0 \tag{D.4}$$

$$[a_{1(2)}, a_{2(1)}^\dagger] = 0 \tag{D.5}$$

Relations between u, v, x, y follow:

$$u^2 + v^2 = x^2 + y^2 = 1 \tag{D.6}$$

$$ux + vy = 0 \tag{D.7}$$

The cavity modes are governed by the Hamiltonian

$$H_{cav} = \omega_L a_L^\dagger a_L + \omega_R a_R^\dagger a_R + g \left(a_L^\dagger a_R + a_R^\dagger a_L \right), \tag{D.8}$$

so that equations of motion are given by

$$\begin{pmatrix} \dot{a}_L \\ \dot{a}_R \end{pmatrix} = \begin{pmatrix} -i\omega_L - ig \\ -ig - i\omega_R \end{pmatrix} \begin{pmatrix} a_L \\ a_R \end{pmatrix} \tag{D.9}$$

Differentiating equations D.1 and substituting in equation D.9 gives

$$\begin{pmatrix} \dot{a}_1 \\ \dot{a}_2 \end{pmatrix} = -i \begin{pmatrix} u\omega_L + vg & ug + v\omega_R \\ x\omega_L + yg & xg + y\omega_R \end{pmatrix} \begin{pmatrix} a_l \\ a_R \end{pmatrix}. \tag{D.10}$$

Upper and lower branch modes are expected to evolve as

$$
\begin{pmatrix} \dot{a}_1 \\ \dot{a}_2 \end{pmatrix} = -i \begin{pmatrix} \omega_1 & \\ & \omega_2 \end{pmatrix} \begin{pmatrix} a_1 \\ a_2 \end{pmatrix}.
\tag{D.11}
$$

Coefficients are solved for by applying condition D.6:

$$
v = \frac{\omega_1 - \omega_L}{\sqrt{g^2 + (\omega_1 - \omega_L)^2}}
\tag{D.12}
$$

$$
u = \frac{g}{\sqrt{g^2 + (\omega_1 - \omega_L)^2}}
\tag{D.13}
$$

$$
x = \frac{\omega_2 - \omega_R}{\sqrt{g^2 + (\omega_2 - \omega_R)^2}}
\tag{D.14}
$$

$$
y = \frac{g}{\sqrt{g^2 + (\omega_2 - \omega_R)^2}}
\tag{D.15}
$$

Frequencies $\omega_{1,2}$ are the eigenvectors, ω, of the matrix in D.9

$$
-i \begin{vmatrix} \omega_L - \omega & g \\ g & \omega_R - \omega \end{vmatrix} = 0
\tag{D.16}
$$

$$
(\omega_L - \omega)(\omega_R - \omega) - g^2 = 0
\tag{D.17}
$$

$$
\omega = \frac{\omega_L + \omega_R}{2} \pm \sqrt{\frac{(\omega_L - \omega_R)^2}{4} + g^2}
\tag{D.18}
$$

$$
\omega = \omega_0 \pm \sqrt{(\lambda q)^2 + g^2},
\tag{D.19}
$$

where the frequencies $\omega_{1,2}$ are then identified as the positive and negative roots in Equation D.19:

$$
\omega_1 = \omega_0 + \sqrt{(\lambda q)^2 + g^2},
\tag{D.20}
$$

$$
\omega_2 = \omega_0 - \sqrt{(\lambda q)^2 + g^2}.
\tag{D.21}
$$

The Hamiltonian is then written in terms of the upper and lower branches:

$$
\begin{aligned}
H &= \omega_1 a_1^\dagger a_1 + \omega_2 a_2^\dagger a_2 + \frac{1}{2}\omega_m(q^2 + q^2) \\
&\quad + \Omega(a_L e^{i\omega_d t} + a_L^\dagger e^{i\omega_d t}).
\end{aligned}
\tag{D.22}
$$

The drive term can be written in terms of $a_{1,2}$,

$$
\begin{aligned}
H_d &= \Omega(a_L e^{i\omega_d t} + a_L^\dagger e^{-i\omega_d t})
\tag{D.23} \\
&= \Omega(X a_1^\dagger e^{-i\omega_d t} - Y a_2^\dagger e^{-i\omega_d t} + X a_1 e^{i\omega_d t} \\
&\quad - Y a_2 e^{i\omega_d t}),
\tag{D.24}
\end{aligned}
$$

where X and Y are given by

$$X = \frac{y}{uy - vx} \tag{D.25}$$

$$Y = \frac{v}{uy - vx} \tag{D.26}$$

A unitary transformation eliminates time dependence,

$$H_0 = \omega_d(a_1^\dagger a_1 + a_2^\dagger a_2) \tag{D.27}$$

$$U = e^{iH_0 t/\hbar}, \tag{D.28}$$

giving a drive term

$$H_d = \Omega_d\left[X(a_1 + a_1^\dagger) - Y(a_2 + a_2^\dagger)\right], \tag{D.29}$$

and an effective Hamiltonian of

$$H_{eff} = H_{int} - H_0, \tag{D.30}$$

$$\tag{D.31}$$

where $H_{int} = UHU^\dagger$.

E

ROUTH HURWITZ STABILITY CRITERION

Consider a system with n degrees of freedom. In a linearized problem, coupled differential equations can be written for the fluctuations, in matrix form as follows:

$$\begin{pmatrix} \dot{x}_n \\ \dot{x}_{n-1} \\ \vdots \\ \dot{x}_0 \end{pmatrix} = M \begin{pmatrix} x_n \\ x_{n-1} \\ \vdots \\ x_0 \end{pmatrix}, \qquad \text{(E.1)}$$

where M describes the time evolution of the vector $\vec{x}$. If oscillatory solutions are sought in the form $\vec{x}(t) = \vec{x}_0 e^{\Lambda t}$, the problem becomes an eigenvalue equation:

$$\begin{vmatrix} M_{1,1} - \Lambda & M_{1,2} & \cdots & M_{1,n} \\ M_{2,1} & M_{2,2} - \Lambda & \cdots & M_{2,n} \\ \vdots & & \ddots & \\ M_{n,1} & & & M_{n,n} - \Lambda \end{vmatrix} \begin{pmatrix} x_n \\ x_{n-1} \\ \vdots \\ x_0 \end{pmatrix} = 0, \quad \text{(E.2)}$$

where non trivial solutions are sought by setting $\det\{M - \Lambda\} = 0$. The variable Λ is then the solution to a polynomial of root n:

$$a_n \Lambda^n + a_{n-1} \Lambda^{n-1} + \ldots + a_1 \Lambda + a_0 = 0 \qquad \text{(E.3)}$$

There are n roots to the polynomial, which, in general are complex. In order for $\vec{x}(t)$ to be a stable fluctuation, the real part of each solution, Λ must be negative. Without explicitly solving for Λ, the stability of solutions can be determined by the Routh Hurwitz Criterion, which analyses the coefficients a_0 through a_n. There are two criteria to be met:

1. All coefficients must be real, non zero and have the same sign.

2. The elements in the first column of the Routh Array must all have the same sign.

The last condition is based on an object called a Routh array, which is constructed from combinations of the coefficients as described in table E.1. The elements in the first two rows are

given by alternating coefficients from the polynomial in question. Further elements in each row are given by determinants of two by two matrices formed from adjacent elements in the array, with the bottom left corner lying directly above the element in question. For a polynomial of order n, the Routh array has $n + 1$ rows. To clarify, an example is given below:

a_n	a_{n-2}	$\dots$	
a_{n-1}	a_{n-3}	$\dots$	
b_1	b_2	b_3	$\dots$
c_1	c_2	c_3	$\dots$
$\vdots$		$\dots$	

Table E.1: The Routh array, with elements defined in terms of the coefficients of the polynomial in question. Elements of the left column must be positive in order to satisfy the second condition.

$$b_1 = \begin{vmatrix} a_n & a_{n-2} \\ a_{n-1} & a_{n-3} \end{vmatrix}, \tag{E.4}$$

$$= \frac{a_n a_{n-3} - a_{n-2} a_{n-1}}{a_{n-1}}. \tag{E.5}$$

E.1   ROUTH ARRAY FOR THE STATIC BISTABILITY

The Routh array for Equation 4.47 is shown in Table E.2, and consists of seven rows. With the proviso that elements a_6 to a_0 are positive (see Section 4.3.1), one requires elements b_1 to f_1 to be positive. For element b_1 this is possible to show:

$$b_1 = \frac{a_5 a_4 - a_6 a_3}{a_5} \tag{E.6}$$

$$= \frac{\kappa \left(4g^2 + 5\kappa^2 + 4\kappa\gamma + \gamma^2 + 2(\Delta_L^2 + \Delta_R^2) + \gamma\omega_m^2 \right)}{4\kappa + \gamma}, \tag{E.7}$$

which is always positive, since κ and γ are positive. The element f_1 is given by a_0, which is positive in the case $\eta_d > 0$.

For further elements in the array, however, expressions are long and cumbersome. It is not possible to deduce their positivity analytically - however, plots of the elements for the range of parameters considered are shown in Figure E.1, and are indeed positive. Whilst this doesn't prove definitively that the second condition is always met, it is at least met for this example, in the range where $\Delta_L, \Delta_R > 0$.

a_6	a_4	a_2	a_0
a_5	a_3	a_1	0
$b_1 = \frac{a_5 a_4 - a_6 a_3}{a_5}$	$b_2 = \frac{a_5 a_2 - a_6 a_1}{a_5}$	$b_3 = a_0$	0
$c_1 = \frac{b_1 a_3 - a_5 b_2}{b_1}$	$c_2 = \frac{b_1 a_1 - a_5 b_3}{b_1}$	$c_3 = 0$	0
$d_1 = \frac{c_1 b_2 - b_5 c_2}{c_1}$	$d_2 = a_0$	$d_1 = 0$	0
$e_1 = \frac{d_1 c_2 - c_5 d_2}{d_1}$	$e_2 = 0$	0	0
$f_1 = a_0$	$f_2 = 0$	$f_1 = 0$	o

Table E.2: A table detailing elements of the Routh Array, in terms of coefficients as described in equation E.3.
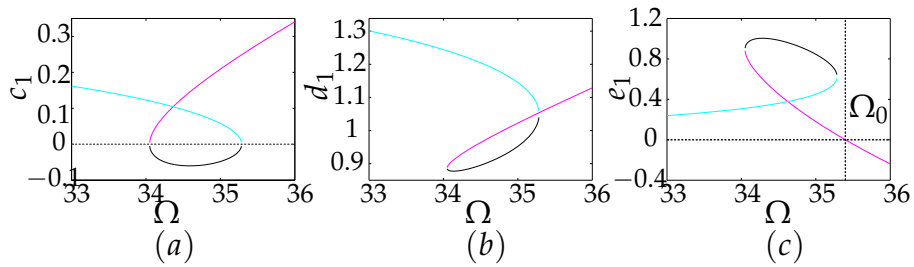

Figure E.1: Plots of c_1, d_1 and e_1 for the parameters explored in Section 4.3.1 of Chapter 4. Each is positive over the range where $0 < \eta_d < 1$. In (c), Ω_0 indicates where the fixed point solution becomes unstable and oscillations occur.

F

ROTATING WAVE APPROXIMATION FOR EVEN N

In Chapter 5 the RWA is applied to give expression for the coefficients $c_{\pm}$, which can be solved analytically. The analysis is presented for the case of odd n (with results presented for $n = 1$), but can be generalised for all n. Below the calculation is explicitly shown for the case where n is even, to show how a similar result is reached.

Equations 5.75 to 5.78 give the matrix elements for V, for even n these are

$$V_{++} = 2\sum_{\nu} g_{\nu} f_{\nu} ux \tag{F.1}$$

$$V_{--} = 2\sum_{\nu} g_{\nu} f_{\nu} vy \tag{F.2}$$

$$V_{+-} = \sum_{\nu} g_{\nu} f_{\nu} (uy + vx) \tag{F.3}$$

$$V_{-+} = V_{+-}. \tag{F.4}$$

Substituting equations 5.70 to 5.73 gives

$$V_{++} = \frac{2g_0}{\Delta_E} \tag{F.5}$$

$$V_{--} = -V_{++} \tag{F.6}$$

$$V_{+-} = \frac{-2\lambda q_0}{\Delta_E}. \tag{F.7}$$

$$\tag{F.8}$$

Note that the matrix elements V_{++} and V_{--} do not vanish in this case.

The coefficients then obey the following equations of motion:

$$i\dot{c}_+ = \sum_{\nu} \left[\frac{2g_0}{\Delta_E} g_{\nu} \left[e^{i\nu\omega_m t} + e^{-i\nu\omega_m t} \right] c_+ \right.$$

$$\left. - \frac{2\lambda q_0}{\Delta_E} g_{\nu} \left[e^{i\nu\omega_m t} + e^{-i\nu\omega_m t} \right] e^{i\Delta_E(t-t')} c_- \right] \tag{F.9}$$

$$i\dot{c}_- = \sum_{\nu} \left[-\frac{2\lambda q_0}{\Delta_E} g_{\nu} \left[e^{i\nu\omega_m t} + e^{-i\nu\omega_m t} \right] e^{-i\Delta_E(t-t')} c_+ \right.$$

$$\left. - \frac{2g_0}{\Delta_E} g_{\nu} \left[e^{i\nu\omega_m t} + e^{-i\nu\omega_m t} \right] c_- \right]. \tag{F.10}$$

Applying the RWA, only terms with exponents $\pm|\Delta_E - n\omega_m|$ are retained, giving

$$\dot{c}_+ = i\sum_\nu \frac{2\lambda q_0}{\Delta_E} g_n e^{i(\Delta_E - \nu\omega_m)(t-t')} e^{-i\nu\omega_m t'} c_- \qquad \text{(F.11)}$$

$$\dot{c}_- = i\sum_\nu \frac{2\lambda q_0}{\Delta_E} g_n e^{-i(\Delta_E - \nu\omega_m)(t-t')} e^{i\nu\omega_m t'} c_+, \qquad \text{(F.12)}$$

which are almost identical to Equations 5.94 and 5.95, for the odd n case, save for a factor of $2\lambda q_0/\Delta_E$. The remaining analysis then proceeds by redefining g_n as g'_n:

$$g'_n = \frac{2\lambda q_0 g}{\Delta_E} J_n\left(\frac{2\lambda A}{\omega_m}\right). \qquad \text{(F.13)}$$

BIBLIOGRAPHY

[1] D. F. Walls and G. J. Milburn. *Quantum Optics*. Springer-Link: Springer e-Books. Springer, (2008).

[2] M. Planck. Ueber das Gesetz der Energieverteilung im Normalspectrum. *Annalen der Physik*, **309**:553–563, (1901).

[3] A. Einstein. ber einen die Erzeugung und Verwandlung des Lichtes betreffenden heuristischen Gesichtspunkt. *Annalen der Physik*, **322**:132–148, (1905).

[4] R. Villard. *Changes Within Physical Systems And/or Conservation of Energy and Momentum: An Anthology of Current Thought*. Contemporary discourse in the field of physics. Rosen Publishing Group, (2005).

[5] Japanese Aerospace Exploration Agency. Small Solar Power Sail Demonstrator 'IKAROS' Successful Solar Sail Deployment, June (2010).

[6] P. Lebedew. Untersuchungen ber die Druckkrfte des Lichtes. *Annalen der Physik*, **311**:433–458, (1901).

[7] V. B. Braginsky, Y. I. Vorontsov, and K. S. Thorne. Quantum Nondemolition Measurements. *Science*, **209**:547–557, (1980).

[8] P. Meystre, M.O. Scully, and North Atlantic Treaty Organization. Scientific Affairs Division. *Quantum optics, experimental gravity, and measurement theory*. NATO advanced science institutes series: Physics. Plenum Press, (1983).

[9] F. Marquardt and S. M. Girvin. Optomechanics. *Physics*, **2**:40, (2009).

[10] J. Qian, A. A. Clerk, K. Hammerer, and F. Marquardt. Quantum Signatures of the Optomechanical Instability. *Phys. Rev. Lett.*, **109**:253601, (2012).

[11] W. Marshall, C. Simon, R. Penrose, and D. Bouwmeester. Towards Quantum Superpositions of a Mirror. *Phys. Rev. Lett.*, **91**:130401, (2003).

[12] P. D. Nation. Nonclassical mechanical states in an optomechanical micromaser analog. *Phys. Rev. A*, **88**:053828, (2013).

[13] F. Marquardt, J. P. Chen, A. A. Clerk, and S. M. Girvin. Quantum Theory of Cavity-Assisted Sideband Cooling of Mechanical Motion. *Phys. Rev. Lett.*, **99**:093902, (2007).

[14] J. D. Teufel, T. Donner, Dale Li, J. W. Harlow, M. S. Allman, K. Cicak, A. J. Sirois, J. D. Whittaker, K. W. Lehnert, and R. W. Simmonds. Sideband cooling of micromechanical motion to the quantum ground state. *Nature*, **475**:359–363, (2011).

[15] D. A. Rodrigues, J. Imbers, and A. D. Armour. Quantum Dynamics of a Resonator Driven by a Superconducting Single-Electron Transistor: A Solid-State Analogue of the Micromaser. *Phys. Rev. Lett.*, **98**:067204, (2007).

[16] A. M. Jayich, J. C. Sankey, B. M. Zwickl, C. Yang, J. D. Thompson, S. M. Girvin, A. A. Clerk, F. Marquardt, and J. G. E. Harris. Dispersive optomechanics: a membrane inside a cavity. *New Journal of Physics*, **10**:095008, (2008).

[17] M. R. Vanner. Selective Linear or Quadratic Optomechanical Coupling via Measurement. *Phys. Rev. X*, **1**:021011, (2011).

[18] C. Biancofiore, M. Karuza, M. Galassi, R. Natali, P. Tombesi, G. Di Giuseppe, and D. Vitali. Quantum dynamics of an optical cavity coupled to a thin semitransparent membrane: Effect of membrane absorption. *Phys. Rev. A*, **84**:033814, (2011).

[19] B. M. Zwickl, W. E. Shanks, A. M. Jayich, C. Yang, A. C. Bleszynski Jayich, J. D. Thompson, and J. G. E. Harris. High quality mechanical and optical properties of commercial silicon nitride membranes. *Applied Physics Letters*, **92**:103125, (2008).

[20] D. J. Wilson, C. A. Regal, S. B. Papp, and H. J. Kimble. Cavity Optomechanics with Stoichiometric SiN Films. *Phys. Rev. Lett.*, **103**:207204, (2009).

[21] G. D. Cole, I. Wilson-Rae, K. Werbach, M. R. Vanner, and M. Aspelmeyer. Phonon-tunnelling dissipation in mechanical resonators. *Nat Commun*, **2**:231, (2011).

[22] J. D. Thompson, B. M. Zwickl, A. M. Jayich, Florian Marquardt, S. M. Girvin, and J. G. E. Harris. Strong dispersive coupling of a high-finesse cavity to a micromechanical membrane. *Nature*, **452**:72–75, (2008).

[23] E. Buks. Decoherence suppression by cavity optomechanical cooling. *Comptes Rendus Physique*, **13**:454 – 469, (2012).

[24] D. Vitali, S. Gigan, A. Ferreira, H. R. Böhm, P. Tombesi, A. Guerreiro, V. Vedral, A. Zeilinger, and M. Aspelmeyer. Optomechanical Entanglement between a Movable Mirror and a Cavity Field. *Phys. Rev. Lett.*, **98**:030405, (2007).

[25] J. C. Sankey, C. Yang, B. M. Zwickl, A. M. Jayich, and J. G. E. Harris. Strong and tunable nonlinear optomechanical coupling in a low-loss system. *Nat Phys*, **6**:707–712, (2010).

[26] A. B. Matsko, A. A. Savchenkov, V. S. Ilchenko, D. Seidel, and L. Maleki. Optomechanics with Surface-Acoustic-Wave Whispering-Gallery Modes. *Phys. Rev. Lett.*, **103**:257403, (2009).

[27] K. Srinivasan, H. Miao, M. T. Rakher, M. Davanco, and V. Aksyuk. Optomechanical Transduction of an Integrated Silicon Cantilever Probe Using a Microdisk Resonator. *Nano Letters*, **11**:791–797, (2011).

[28] I. Favero and K. Karrai. Cavity cooling of a nanomechanical resonator by light scattering. *New Journal of Physics*, **10**:095006, (2008).

[29] J. et. al. Aasi. Enhanced sensitivity of the LIGO gravitational wave detector by using squeezed states of light. *Nature Photonics*, **7**:613–619, (2013).

[30] D. A. Rodrigues and A. D. Armour. Amplitude Noise Suppression in Cavity-Driven Oscillations of a Mechanical Resonator. *Phys. Rev. Lett.*, **104**:053601, (2010).

[31] A. Armour and D. Rodrigues. Quantum dynamics of a mechanical resonator driven by a cavity. *Comptes Rendus Physique*, **13**:440 – 453, (2012).

[32] A. Schliesser, O. Arcizet, R. Riviere, G. Anetsberger, and T. J. Kippenberg. Resolved-sideband cooling and position measurement of a micromechanical oscillator close to the Heisenberg uncertainty limit. *Nat Phys*, **5**:509–514, (2009).

[33] K. Børkje, A. Nunnenkamp, B. M. Zwickl, C. Yang, J. G. E. Harris, and S. M. Girvin. Observability of radiation-pressure shot noise in optomechanical systems. *Phys. Rev. A*, **82**:013818, (2010).

[34] I. Wilson-Rae, N. Nooshi, J. Dobrindt, T. J. Kippenberg, and W . Zwerger. Cavity-assisted backaction cooling of mechanical resonators. *New Journal of Physics*, **10**:095007, (2008).

[35] C. Genes, D. Vitali, P. Tombesi, S. Gigan, and M. Aspelmeyer. Ground-state cooling of a micromechanical oscillator: Comparing cold damping and cavity-assisted cooling schemes. *Phys. Rev. A*, **77**:033804, (2008).

[36] A. Schliesser, P. Del'Haye, N. Nooshi, K. J. Vahala, and T. J. Kippenberg. Radiation Pressure Cooling of a Micromechanical Oscillator Using Dynamical Backaction. *Phys. Rev. Lett.*, **97**:243905, (2006).

[37] C. Metzger, M. Ludwig, C. Neuenhahn, A. Ortlieb, I. Favero, K. Karrai, and F. Marquardt. Self-Induced Oscillations in an Optomechanical System Driven by Bolometric Backaction. *Phys. Rev. Lett.*, **101**:133903, (2008).

[38] G. Anetsberger, O. Arcizet, Q. P. Unterreithmeier, R. Riviere, A. Schliesser, E. M. Weig, J. P. Kotthaus, and T. J. Kippenberg. Near-field cavity optomechanics with nanomechanical oscillators. *Nat Phys*, **5**:909–914, (2009).

[39] G. Heinrich, J. G. E. Harris, and F. Marquardt. Photon shuttle: Landau-Zener-Stückelberg dynamics in an optomechanical system. *Phys. Rev. A*, **81**:011801, (2010).

[40] J. Larson and M. Horsdal. Photonic Josephson effect, phase transitions, and chaos in optomechanical systems. *Phys. Rev. A*, **84**:021804, (2011).

[41] F. Marquardt, J. G. E. Harris, and S. M. Girvin. Dynamical Multistability Induced by Radiation Pressure in High-Finesse Micromechanical Optical Cavities. *Phys. Rev. Lett.*, **96**:103901, (2006).

[42] T. Carmon, M. C. Cross, and K. J. Vahala. Chaotic Quivering of Micron-Scaled On-Chip Resonators Excited by Centrifugal Optical Pressure. *Phys. Rev. Lett.*, **98**:167203, (2007).

[43] P. Rabl. Photon Blockade Effect in Optomechanical Systems. *Phys. Rev. Lett.*, **107**:063601, (2011).

[44] J. D. Teufel, Dale Li, M. S. Allman, K. Cicak, A. J. Sirois, J. D. Whittaker, and R. W. Simmonds. Circuit cavity electromechanics in the strong-coupling regime. *Nature*, **471**:204–208, (2011).

[45] A. Nunnenkamp, K. Børkje, J. G. E. Harris, and S. M. Girvin. Cooling and squeezing via quadratic optomechanical coupling. *Phys. Rev. A*, **82**:021806, (2010).

[46] J. C. Maxwell. *A Treatise on Electricity and Magnetism*. A Treatise on Electricity and Magnetism 2 Volume Paperback Set. Cambridge University Press, (2010).

[47] I. Wilson-Rae. Intrinsic dissipation in nanomechanical resonators due to phonon tunneling. *Phys. Rev. B*, **77**:245418, (2008).

[48] A. Venkatesan, K. J. Lulla, M. J. Patton, A. D. Armour, C. J. Mellor, and J. R. Owers-Bradley. Dissipation due to tunneling two-level systems in gold nanomechanical resonators. *Phys. Rev. B*, **81**:073410, (2010).

[49] M. Aspelmeyer, T. J. Kippenberg, and F. Marquardt. Cavity Optomechanics. *ArXiv 1303.0733*, (2013).

[50] C. W. Gardiner. Handbook of stochastic methods. *Springer Series in Synergetics*, (1985).

[51] H.J. Groenewold. On the principles of elementary quantum mechanics. *Physica*, (1946).

[52] S Nasiri. Distribution functions in light of the uncertainty principle. *Iranian Journal of Science and Technology*, **29**:259, (2005).

[53] L. You, J. Cooper, and P. Zoller. Quantum-classical correspondences for atomic operators: a positive P representation approach. *J. Opt. Soc. Am. B*, **12**, (1994).

[54] P. Kinsler and P. D. Drummond. Quantum dynamics of the parametric oscillator. *Phys. Rev. A*, **43**:6194–6208, (1991).

[55] K.F. Riley, P. Hobson, and S.J. Bence. *Mathematical Methods for Physics and Engineering: A Comprehensive Guide*. Cambridge University Press, (2006).

[56] J. Larson. Dynamics of the JaynesCummings and Rabi models: old wine in new bottles. *Physica Scripta*, **76**:146, (2007).

[57] C. H. Metzger and K. Karrai. Cavity cooling of a microlever. *Nature*, **432**:1002–1005, (2004).

[58] H.J. Weber and G.B. Arfken. *Essential Mathematical Methods for Physicists*. Academic Press, (2004).

[59] A. Nunnenkamp, K. Børkje, and S. M. Girvin. Single-Photon Optomechanics. *Phys. Rev. Lett.*, **107**:063602, (2011).

[60] K. Blum. *Density Matrix Theory and Applications*. Springer Series on Atomic, Optical, and Plasma Physics. Springer, (2012).

[61] D.K. Bhushan. *Matrix And Linear Algebra 2Nd Ed.* Prentice-Hall Of India Pvt. Limited, (2009).

[62] A A Clerk, F Marquardt, and K Jacobs. Back-action evasion and squeezing of a mechanical resonator using a cavity detector. *New Journal of Physics*, **10**:095010, (2008).

[63] T. J. Kippenberg and K. J. Vahala. Cavity Optomechanics: Back-Action at the Mesoscale. *Science*, **321**:1172–1176, (2008).

[64] M. Karuza, M. Galassi, C. Biancofiore, C. Molinelli, R. Natali, P Tombesi, G Di Giuseppe, and D Vitali. Tunable linear and quadratic optomechanical coupling for a tilted membrane within an optical cavity: theory and experiment. *Journal of Optics*, **15**, (2013).

[65] K. Thyagarajan and A. Ghatak. *Lasers: Fundamentals and Applications*. Graduate Texts in Physics. Springer, (2010).

[66] S. Groblacher, K. Hammerer, M. R. Vanner, and M. Aspelmeyer. Observation of strong coupling between a micromechanical resonator and an optical cavity field. *Nature*, **460**:724–727, (2009).

[67] Georg Heinrich. *Nanomechanics interacting with light: Dynamics of coupled multimode optomechanical systems*. PhD thesis, Universitt Erlangen-Nrnberg, (2011).

[68] G. Heinrich, M. Ludwig, H. Wu, K. Hammerer, and Florian Marquardt. Dynamics of coupled multimode and hybrid optomechanical systems. *Comptes Rendus Physique*, **12**:837–847, (2011).

[69] R. Ghobadi, A. R. Bahrampour, and C. Simon. Quantum optomechanics in the bistable regime. *Phys. Rev. A*, **84**:033846, (2011).

[70] N.K. Sinha. *Control Systems*. New Age International (P) Limited, (2008).

[71] U. Weiss. *Quantum Dissipative Systems*. Series in modern condensed matter physics. World Scientific, (2012).

[72] E. Verhagen, S. Deleglise, S. Weis, A. Schliesser, and T. J. Kippenberg. Quantum-coherent coupling of a mechanical oscillator to an optical cavity mode. *Nature*, **482**:63–67, (2012).

[73] D. Zill and W. Wright. *Differential Equations with Boundary-Value Problems*. Textbooks Available with Cengage Youbook. Cengage Learning, (2012).

[74] H. Wu, G. Heinrich, and F. Marquardt. The effect of LandauZener dynamics on phonon lasing. *New Journal of Physics*, **15**:123022, (2013).

[75] D.J. Griffiths. *Introduction to quantum mechanics*. Pearson Prentice Hall, (2005).

[76] A. Aspect, W. Barletta, and R. Bonifacio. *Coherent and Collective Interactions of Particles and Radiation Beams*. IOS Press, (1997).

[77] T. Harvey. *Noise in a dynamical open quantum system: coupling a resonator to an artificial atom.* PhD thesis, University of Nottingham, (2009).

[78] M. Jakob and S. Stenholm. Variational functions in degenerate open quantum systems. *Phys. Rev. A*, **69**:042105, (2004).